

DUDLEY KNOX LIBRARY
NAVAL POSTGRADUATE SCHOOL
MONTEREY CA 93943-5101

REPORT DOCUMENTATION PAGE

1a. REPORT SECURITY CLASSIFICATION UNCLASSIFIED			1b. RESTRICTIVE MARKINGS		
2a. SECURITY CLASSIFICATION AUTHORITY			3. DISTRIBUTION/AVAILABILITY OF REPORT Approved for public release; distribution is unlimited.		
2b. DECLASSIFICATION/DOWNGRADING SCHEDULE					
4. PERFORMING ORGANIZATION REPORT NUMBER(S)			5. MONITORING ORGANIZATION REPORT NUMBER(S)		
6a. NAME OF PERFORMING ORGANIZATION Naval Postgraduate School		6b. OFFICE SYMBOL (If applicable) EW		7a. NAME OF MONITORING ORGANIZATION Naval Postgraduate School	
6c. ADDRESS (City, State, and ZIP Code) Monterey, CA 93943-5000				7b. ADDRESS (City, State, and ZIP Code) Monterey, CA 93943-5000	
8a. NAME OF FUNDING/SPONSORING ORGANIZATION		8b. OFFICE SYMBOL (If applicable)		9. PROCUREMENT INSTRUMENT IDENTIFICATION NUMBER	
8c. ADDRESS (City, State, and ZIP Code)		10. SOURCE OF FUNDING NUMBERS			
		Program Element No.		Project No.	Task No. Work Unit Accession Number
11. TITLE (Include Security Classification) DEFINITION OF THE SEA SURFACE INFRARED SUN GLITTER CORRIDOR					
12. PERSONAL AUTHOR(S) Moss, Eric Brian					
13a. TYPE OF REPORT Master's Thesis		13b. TIME COVERED From To		14. DATE OF REPORT (year, month, day) September 1992	
				15. PAGE COUNT 155	
16. SUPPLEMENTARY NOTATION The views expressed in this thesis are those of the author and do not reflect the official policy or position of the Department of Defense or the U.S. Government.					
17. COSATI CODES			18. SUBJECT TERMS (continue on reverse if necessary and identify by block number)		
FIELD	GROUP	SUBGROUP	Thermal Radiation, Infrared, Sun Glitter, Sun Glints, AGA, Thermovision 780 System, LOWTRAN 6, Background IR Radiance		
19. ABSTRACT (continue on reverse if necessary and identify by block number) Measurements of sea surface radiance were made in the 2-5.6 and 8-14 micrometer wavebands within patterns of intense specular highlights formed near the azimuth of the sun at low solar observation angles. From these measurements, an analysis of the statistical and physical nature of a sun glitter channel as presented to a low altitude observer (i.e., shipboard) was conducted. Findings showed strong correlations between wind speed and corridor width, and between wind speed and the strength of source radiance, dominated primarily by the direct solar reflected contribution to sea radiance. 8-14 micrometer radiances showed far less susceptibility to the detrimental effects of sun glitter on IR sensing systems. All patterns were gaussian in shape across the azimuthal extent of each glitter corridor. The magnitude of glinting radiances decreased with increasing depression angles, presenting an approximate half-gaussian radiance distribution in elevation. A method to convert apparent radiance (as received at the sensor) to equivalent zero-range blackbody radiance was formulated but showed weaknesses in computing the path radiance of the atmosphere intervening between the sea and the AGA 780 sensor, and in accounting for the emissivity of the sea as it affected the self-emitted component of sea surface source radiance.					
20. DISTRIBUTION/AVAILABILITY OF ABSTRACT <input checked="" type="checkbox"/> UNCLASSIFIED/UNLIMITED <input type="checkbox"/> SAME AS REPORT <input type="checkbox"/> DTIC USERS				21. ABSTRACT SECURITY CLASSIFICATION Unclassified	
22a. NAME OF RESPONSIBLE INDIVIDUAL A.W. Cooper				22b. TELEPHONE (Include Area code) (408) 646-2452	
				22c. OFFICE SYMBOL PH Cr	

Approved for public release; distribution is unlimited.

DEFINITION OF THE SEA SURFACE
INFRARED
SUN GLITTER CORRIDOR

by

Eric B. Moss
Lieutenant, United States Navy
B.S., United States Naval Academy, 1983

Submitted in partial fulfillment
of the requirements for the degree of

MASTER OF SCIENCE IN SYSTEMS ENGINEERING

from the

NAVAL POSTGRADUATE SCHOOL
September 1992

ABSTRACT

Measurements of sea surface radiance were made in the 2-5.6 and 8-14 μm wavebands within patterns of intense specular highlights formed near the azimuth of the sun at low solar observation angles. From these measurements, an analysis of the statistical and physical nature of a sun glitter channel as presented to a low altitude observer (i.e. shipboard) was conducted. Findings showed strong correlations between wind speed and corridor width, and between wind speed and the strength of source radiance, dominated primarily by the direct solar reflected contribution to sea radiance. 8-14 μm radiances showed far less susceptibility to the detrimental effects of sun glitter on IR sensing systems. All patterns were gaussian in shape across the azimuthal extent of each glitter corridor. The magnitude of glinting radiances decreased with increasing depression angles, presenting an approximate half gaussian radiance distribution in elevation. A method to convert apparent radiance (as received at the sensor) to equivalent zero-range blackbody source radiance was formulated but showed weaknesses in computing the path radiance of the atmosphere intervening between the sea and the AGA 780 sensor, and in accounting for the emissivity of the sea surface as it affected the self-emitted component of sea surface source radiance.

TABLE OF CONTENTS

I.	INTRODUCTION	1
II.	INFRARED FUNDAMENTALS	7
A.	THERMAL RADIATION THEORY	7
1.	Planck's Law	7
2.	Kirchhoff's Law	10
3.	Stefan-Boltzmann Law	11
4.	Wien's Displacement Law	12
5.	Lambert's Law	12
B.	INFRARED ATMOSPHERIC INTERACTIONS	13
III.	NATURAL INFRARED BACKGROUND SOURCES	18
A.	SKY SPECTRAL RADIANCE	19
1.	Atmospheric Path Radiance	20
2.	Solar Scattering	25
a.	Clear Sky Radiance	29
b.	Overcast and Cloudy Sky Radiance	31
B.	SEA SURFACE RADIANCE	32
1.	Ocean Thermal Emission	34
2.	Reflectivity and Absorptivity of Smooth Sea Water	35
3.	Solar Glitter	37

IV.	A MODEL OF THE WIND ROUGHENED SEA SURFACE	42
A.	ROUGH SEA EMISSIVITY AND REFLECTIVITY	45
	1. The Schwartz-Hon Model of Rough Sea Emissivity	48
B.	THE COX AND MUNK WAVE SLOPE DISTRIBUTION	53
C.	WAVE SLOPE SHADOWING	60
D.	MEAN SQUARE WAVE SLOPE	62
E.	SOME OBSERVATIONAL ASPECTS OF SUN GLITTER	63
	1. Temporal Nature of Sun Glints	64
	2. Sun Glitter Contribution to Ocean Contrast	65
	a. Wavelength Contrasts	65
	b. Wind-Induced Contrasts	66
F.	GLITTER PATTERN WIDTH	68
V.	DATA COLLECTION AND ANALYSIS	70
A.	EXPERIMENT SETUP AND LOCATION	70
B.	DATA COLLECTION EQUIPMENT	71
	1. The AGA 780 Thermovision Thermal Imaging System	71
	2. Thermal Imaging Techniques	72
C.	SUN GLITTER DATA COLLECTION	77
D.	METEOROLOGICAL DATA COLLECTION	78
E.	DATA ANALYSIS	81
	1. LOWTRAN Atmospheric Prediction Code	88
	2. Correlating the Physical Horizon with the Computer Display	93

F.	SYSTEMATIC SUMMARY OF SUN GLITTER DATA ANALYSIS	94
VI.	RESULTS	100
A.	GLITTER PATTERN WIDTH	100
B.	PLOTS OF GLITTER SOURCE RADIANCE VS. AZIMUTH .	102
C.	HISTOGRAMS OF SUN GLITTER RADIANCE DATA	116
D.	COMPARISON OF RADIANCE VALUES TO PREVIOUS RESEARCH	124
VII.	CONCLUSIONS	131
	APPENDIX A-SUN GLITTER CORRIDOR WIDTH PREDICTION CODE .	135
	APPENDIX B-MATLAB FUNCTIONS AGACOMP.M AND IRTEMP.M . .	139
	LIST OF REFERENCES	141
	INITIAL DISTRIBUTION LIST	145

ACKNOWLEDGEMENTS

This research was supported by the Naval Academic Center for Infrared Technology (NACIT) under Naval Postgraduate School direct funding. Special thanks goes to Mr. Jerry Lenz and Mr. Bob Sanders for their assistance during the Point Sur experiments, and to Professor Gene Crittenden for his help and guidance during the thermal imager calibrations leading up to this thesis' experiments. The author also wishes to express his gratitude to Professor Ed Milne for his contributions and suggestions during data extraction and analysis. Thanks also goes to the Meteorology Department of the Naval Postgraduate School, specifically Keith Jones and Professor Ken Davidson, for their assistance in allowing me to collect on site weather data using their equipment. The efforts of Hayden Sohn and Beverly Ewolding of the California Parks Department are additionally appreciated for their assistance in allowing this experiment to occur at the Pt. Sur Lighthouse. I would especially like to express my gratitude to Prof. A.W. Cooper for providing numerous hours to counsel and direct my efforts throughout the creation of this work.

I. INTRODUCTION

Shipboard infrared (IR) sensors have become an increasingly important part of integrated combat direction systems for naval forces worldwide. They detect airborne and surface threats by sensing the thermal contrast between targets and the ocean background. Such IR backgrounds can be cluttered by clouds or sky/sun reflections from a wind ruffled sea surface. Sensor design and testing procedures, therefore, require accurate descriptions of these ocean backgrounds in order to improve their detection performance.

The processes that control the extent to which IR clutter corrupts a scene (i.e. wind interactions on a water surface) are considerably complex. Statistical models of these phenomena are often obtained empirically, serving to depict macroscopically the elements affecting IR clutter. Several studies have been undertaken to research, develop, and validate such models in an attempt to improve the detection capabilities of shipboard IR systems. Perhaps the most widely accepted of these works is the geometric optics approach of Cox and Munk [Ref. 1].

The ability to detect valid threats with low false alarm rates has become an essential design criterion for IR sensors, where the number of false alarms can be controlled by using *a priori* knowledge of the nature of a given scene's clutter. In

describing the apparent IR radiance of an ocean background within a sensor's field of view (FOV), it becomes necessary to account for several distinct clutter producing mechanisms in spatial, temporal and spectral quantities, since detection algorithms using all of these types of processing are currently employed. Both IR imaging and surveillance systems are affected by clutter. Imaging IR sensors with automatic target recognition schemes especially need accurate clutter and background definitions, since these systems rely on parametric statistical algorithms to identify an object's silhouette against its background [Ref. 2:p. 232].

For a sensor viewing an ocean scene within some specific spectral region of the infrared, the energy received from the sea background originates from four sources. The first of these is the self-emission of the sea itself by virtue of the fact that the water temperature is above absolute zero (-273°C). A second source arises from the inherent radiance of the atmosphere intervening between the sea surface and the sensor. The third source is sky radiance reflecting off the sea surface which is closely related to the fourth source, the intense solar specular reflections off the sea, more commonly known as sun glitter. Figure 1.1 [Ref. 3:p. 1] shows how all of the factors involved in IR sea radiance combine within a scene.

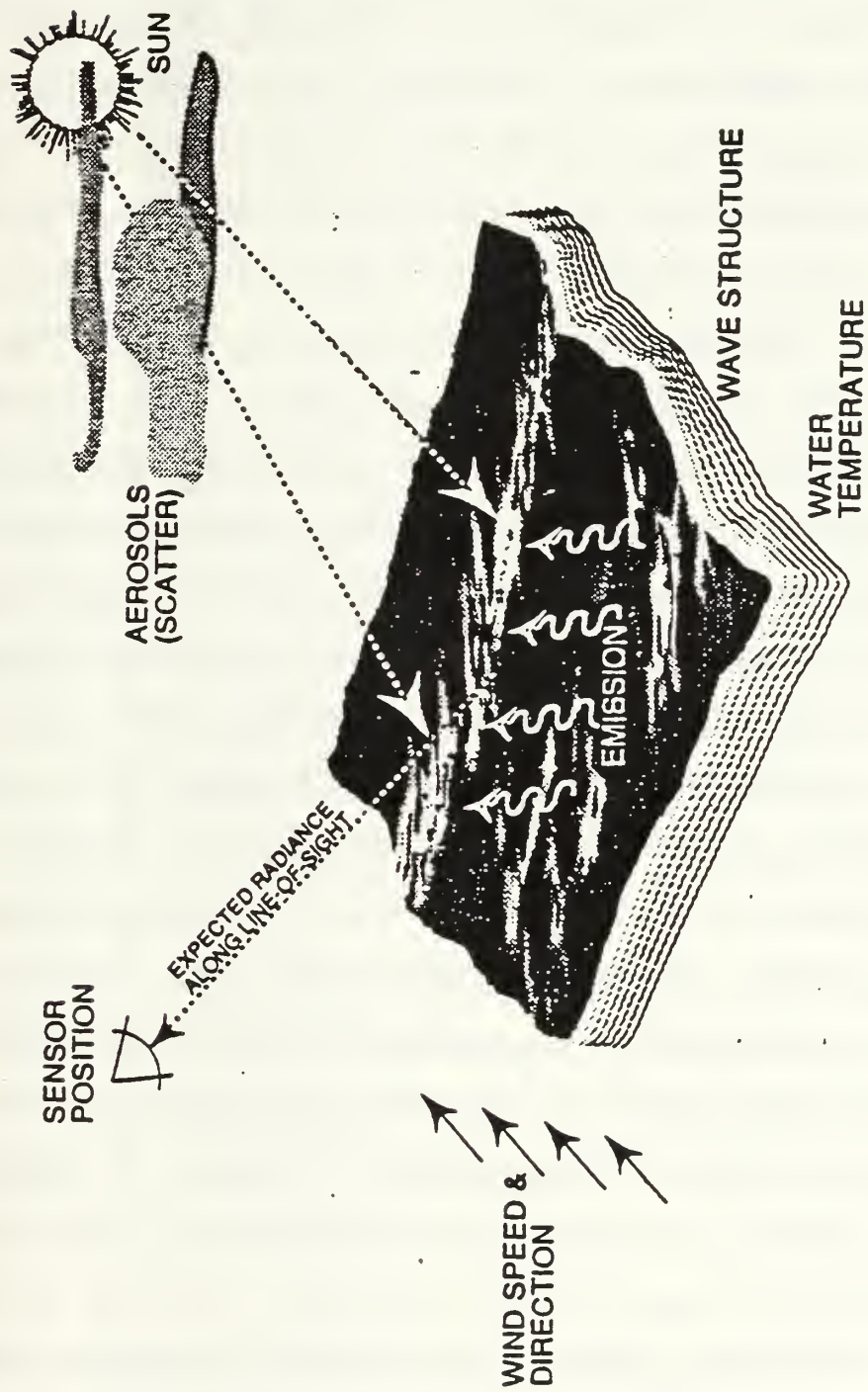


Figure 1.1 Factors involved in IR sea radiance (Ref. 3)

The complexity of any efforts to compute the extent to which these effects interfere with IR sensing is enhanced by the ever changing roughness of the sea surface acting to modulate the sea's source radiance as well as any reflections from skyward radiances. Further, the reflectance and emissivity of sea water also depend upon the roughness of the sea acting to change the orientation of the surface relative to the direction in which a ray is reflected. [Ref. 3:p. 1] If a system designer is able to predict the impact of roughness, then new sensors will be better able to match perceived thermal signals with actual target temperatures.

Sunlight reflecting from a rough water surface consists of a corridor of intense highlights on the surface of the water. This pattern is brightest when looking along an azimuth toward the sun and diminishes symmetrically on both sides of this direction. At any instant in time, there appear to be many separate facets of light which are momentarily oriented to reflect the image of the sun in the direction of the observer. The instantaneous number of these specularly reflecting highlights in a fixed FOV is a random function of the surface wind velocity and direction. The observed brightness within a scene, then, results from a spatial average of radiance values over many unresolved facets. [Ref. 4:p. 41]

Solar reflections (glints) from a smooth surface of water produce a high intensity signal which can compete with or mask

the signal of actual targets. Shipboard defense systems employing IR sensors have experienced saturation of their detectors and detection processing circuitry due to glints from the ocean surface, necessitating that threat sectors below the horizon be blanked up to $\pm 23^\circ$ on either side of the sun's azimuth [Ref. 5:p. 5]. This scheme rejects any true targets which might be otherwise be detectable within the pattern.

The problem of countering the effects of sunglitter radiance, then, is motivated by the need to reduce false alarms which result from viewing the sea surface near the solar azimuth. This problem necessitates development of a clutter model to aid in measuring and testing the performance of shipboard IR sensors. A technique is required, therefore, to predict the spatial and magnitudinal extent of solar glitter and to employ such a prediction in software used to discriminate against the high number of false alarms that would otherwise occur.

In this thesis, an investigation into the nature of sun glitter is described. Measurements of sun glitter were taken in the 2-5.6 μm and 8-14 μm bands, and were subsequently analyzed to produce a definition of the statistical and physical nature of sun glitter corridors under varying weather and sea states. Extensive use was made of existing sun glitter models in an attempt to interpret data such that follow-on comparisons to newer models (such as the SEABEAM

computer code [Ref. 3]) would be possible. A simple algorithm to account for atmospheric attenuation and path radiance effects is introduced so that all resultant output data will be expressed in terms of equivalent blackbody source radiance.

Chapter II contains a description of the necessary theory and equations pertaining to infrared radiation and the effects the atmosphere has upon that radiation. A discussion of naturally occurring radiation sources follows in Chapter III detailing the individual IR signals that comprise clutter. Chapter IV provides a description of a sea surface radiance model, comprised of elements from several existing models. Chapter V details the methodology followed in the measurement and analysis of data for this work, including a description of the AGA 780 Thermovision system used to collect the data. Results of data analysis are presented in Chapter VI followed by conclusions and recommendations in Chapter VII.

II. INFRARED FUNDAMENTALS

A. THERMAL RADIATION THEORY

Infrared radiation is defined as the photon energy emitted by an object resulting from changes in its internal energy. Along the electromagnetic spectrum, infrared energy exists in a band bounded on one side by the visible region at $0.7 \mu\text{m}$ and extending to the millimeter waveband at $1000 \mu\text{m}$. The infrared spectrum is further subdivided for military use into the short-wave infrared (SWIR) $0.7\text{-}3 \mu\text{m}$, the mid-wave infrared (MWIR) $3\text{-}5 \mu\text{m}$ and the long-wave infrared (LWIR) $5\text{-}15 \mu\text{m}$. The following are definitions of certain fundamental concepts and equations which are pertinent to the study of IR radiation.

1. Planck's Law

Thermal or infrared radiation consists of photons that are emitted by molecules undergoing vibrational and rotational quantum transitions. In general, an object whose temperature is greater than absolute zero will emit infrared radiation. Planck postulated that molecular harmonic oscillations occur only at multiples of some basic energy level, proportional to the frequency ν with proportionality constant h , Planck's constant. The energy of such a harmonic oscillator must be $E = nh\nu$, where n is an integer. Working from this relationship, Planck detailed the spectral distribution for a body's

electromagnetic radiant emittance W_λ as a function of its temperature by [Ref. 6:p. 21]

$$W_\lambda(\lambda, T) = \frac{(2\pi hc^2)}{\lambda^5 (\exp(hc/\lambda kT) - 1)}, \quad (\text{Watts/cm}^2 \cdot \mu\text{m}) \quad (2.1)$$

where

λ = wavelength (μm)
 k = Boltzmann's constant (1.38054×10^{-23} Watt·sec·K⁻¹)
 c = speed of light (2.9979×10^{10} cm/s)
 h = Planck's constant (6.6256×10^{-34} Watt·s²)
 T = temperature (K).

Planck's Law details the relationship between temperature and energy emission for a body which has a 100% radiation efficiency. Such theoretical objects are known as blackbodies, defined to be both perfect absorbers and perfect emitters of thermal radiation for a given temperature. The factor which defines the energy a body emits relative to a perfect emitter (a blackbody) is its emissivity ϵ . It is a value between zero (for a nonradiating source) and unity (for a blackbody) which measures how closely a real source approximates a blackbody. The spectral radiant emittance of a blackbody at three representative terrestrial temperatures is shown in Figure 2.1 [Ref. 6:p. 18-23].

To obtain the waveband specific (in-band) radiant emittance W for a particular target or its background, Planck's law must be integrated over the wavelengths of interest to obtain

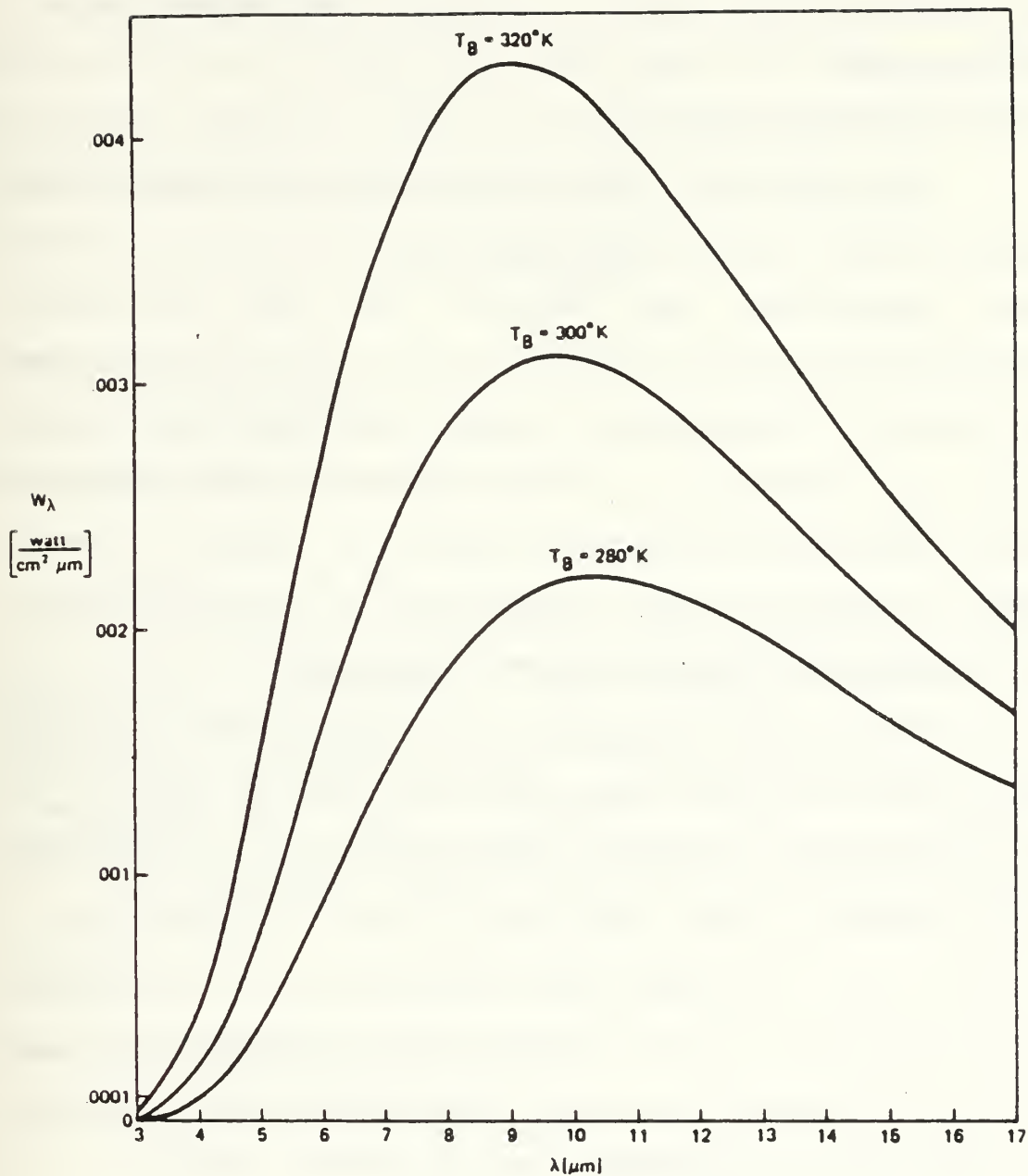


Figure 2.1 Planck's Law for spectral radiant emittance at three background temperatures T_b (Ref. 6)

$$W_{\Delta\lambda}(T) = \int_{\lambda_1}^{\lambda_2} W_{\lambda}(\lambda, T) d\lambda, \quad (\text{Watts/cm}^2). \quad (2.2)$$

This relation yields the total energy a body emits within a given waveband.

2. Kirchhoff's Law

Most naturally occurring IR radiation occurs in the middle infrared region, extending from 3.0 to 14.0 μm . Bodies whose temperatures are between 273 and 300 Kelvin (corresponding to normal terrestrial sea and air temperatures) emit photons at approximately 10 μm . Such bodies may also be reradiating (reflecting) photons emitted by other sources. From a macroscopic perspective, then, an object's overall thermal signature will be a combination of its self-emission and any reflected emissions from other bodies.

The law of conservation of energy states that the radiant energy incident upon a body (U_i) must be equal to the sum of that body's reflected radiant energy (U_ρ), transmitted radiant energy (U_τ) and absorbed radiant energy (U_α) or

$$U_i = U_\rho + U_\tau + U_\alpha, \quad (\text{Joules}). \quad (2.3)$$

Under equilibrium conditions, the energy absorbed by a body must be balanced by the energy it emits, or $U_e = U_\alpha$. Dividing both sides by U_i yields [Ref. 7:p. 40]

$$1 = \rho + \tau + \alpha \quad (2.4)$$

where

ρ = reflectivity
 τ = transmissivity
 α = absorptivity.

Equation (2.4) is valid even when specified over a given wavelength interval. With each term expressed as a spectral quantity, Equation (2.4) becomes [Ref. 8:p. 7]

$$1 = \rho_\lambda + \tau_\lambda + \alpha_\lambda, \quad \epsilon_\lambda = \alpha_\lambda \quad (2.5)$$

where

$\epsilon_\lambda = \alpha_\lambda$ is Kirchhoff's Law.

For opaque bodies, $\tau=0$ resulting in

$$\alpha_\lambda = 1 - \rho_\lambda. \quad (2.6)$$

Equation (2.6) shows that a good reflector is a poor absorber of IR radiation. For a perfect absorber, or blackbody, $\alpha=1$ implying that its emitted radiation will also be a maximum for a given temperature ($\alpha=\epsilon=1$). For some bodies, however, ϵ is smaller than unity but is constant for all wavelengths. Such bodies are known as graybodies. Additionally, a selective radiator would be a body whose ϵ varies as a function of wavelength.

3. Stefan-Boltzmann Law

Solving Planck's integral (Equation (2.2)) over all wavelengths (0 to ∞) yields the total power radiated from a blackbody into a hemispherical solid angle. The closed form solution, known as the Stefan-Boltzmann law, relates the total

radiant emittance of a blackbody $W(T)$ to its temperature and is stated as

$$W(T) = \sigma T^4, \quad (\text{watt/cm}^2) \quad (2.7)$$

where

$$\begin{aligned} \sigma &= \text{Stefan-Boltzmann constant, } 5.6697 \times 10^{-12} \text{ Watt/(cm}^2 \cdot \text{K}^4) \\ &= (2\pi^5 k^4) / (15c^2 h^3) \end{aligned}$$

T = temperature of the blackbody (K).

For graybodies, whose emissivity is constant over all wavelengths, the relation becomes [Ref. 8:p. 8]

$$W(T) = \epsilon \sigma T^4, \quad (\text{watt/cm}^2). \quad (2.8)$$

4. Wien's Displacement Law

Differentiating Planck's law and setting the result equal to zero yields a relation between the wavelength corresponding to a blackbody's maximum radiation power and the temperature of that body. After substituting the appropriate constants, it is found that [Ref. 7:p. 37]

$$\lambda_m = \frac{2893}{T}, \quad (\mu m) \quad (2.9)$$

where

λ_m = wavelength at which radiation power is maximum
 T = temperature of the blackbody (K).

5. Lambert's Law

Rough planar surfaces tend to emit and reflect thermal radiation more or less diffusely. Unlike a specular

reflector, the diffuse reflecting surface spreads its radiant flux over a wide solid angle. The flux from such a surface follows a relation which states that the radiant intensity J (Watts/sr) from a perfectly diffuse source is proportional to the cosine of the angle between the normal to the surface and the viewing angle. The radiance N (Watts/cm²·sr) from a Lambertian surface, however, is independent of viewing angle, since the projected area of the source also varies with the cosine of the same angle. Therefore, the radiance of a Lambertian surface radiating into a hemisphere is [Ref. 7:p. 29]

$$N(T) = \frac{W(T)}{\pi}, \quad \left(\frac{\text{watts}}{\text{cm}^2 \cdot \text{sr}} \right) \quad (2.10)$$

where $W(T)$ is the in-band radiant emittance of the surface.

B. INFRARED ATMOSPHERIC INTERACTIONS

One component common to all naval infrared sensing applications is the atmosphere. Before the radiation from a target reaches a sensor, its flux will be attenuated to some extent by the atmospheric components through which it must travel. Either or both of two mechanisms act to reduce the source radiance reaching a detector: non-forward scattering and absorption. The reason for concern over atmospheric extinction phenomena is that they make the problem of distinguishing a target from its background more difficult by reducing the signal available to infrared detecting systems.

Absorption of IR radiation is a quantum process whereby a molecule or aerosol particle undergoes an increase in its internal energy by absorbing incoming photons. Only those frequencies can be absorbed whose photon energies match the differences between a molecule's allowed energy levels.

Scattering is the process by which a fraction of the radiation emitted by a source towards a detector is deflected into other directions. It occurs because the energy in an electromagnetic wave is intercepted and reradiated into a 4π steradians solid angle. For particles that are very small compared to the wavelength with which they interact, scattering is approximately isotropic; as the ratio of a particle's size to wavelength increases, the scattering becomes concentrated more into the forward hemisphere. For very large objects, forward scattering dominates. [Ref. 9:p. 1.23]

At a specific wavelength for a given atmospheric state, the overall transmissivity τ_A is defined by the Lambert-Beer law as

$$\tau_A = \exp(-\mu(\lambda)R) \quad (2.11)$$

where

R = range or path length
 μ = total extinction coefficient
 λ = wavelength.

Over a band of wavelengths, the average transmittance from λ_1 to λ_2 is

$$\tau_A = \frac{1}{\lambda_2 - \lambda_1} \int_{\lambda_1}^{\lambda_2} \exp[-\mu(\lambda)R] d\lambda. \quad (2.12)$$

The total extinction coefficient μ is the sum of the individual in-band coefficients for total absorption and total non-forward scattering (only non-forward scattering is considered since forward scattering acts to increase the radiance reaching a detector) as detailed by

$$\mu = \mu_A + \mu_S \quad (2.13)$$

where

μ = total extinction coefficient
 μ_A = extinction coefficient for total absorption
 μ_S = extinction coefficient for non-forward scattering.

Scattering and absorption may be further broken down into components according to their sources [Ref. 6:p. 31]

$$\mu_A = k_m + k_A \quad (2.14)$$

$$\mu_S = \sigma_m + \sigma_A \quad (2.15)$$

where

k_m = molecular absorption coefficient
 k_A = aerosol absorption coefficient
 σ_m = molecular scattering coefficient
 σ_A = aerosol scattering coefficient.

The spectral transmittance for a 6000 ft horizontal path at sea level is shown in Figure 2.2, with areas of low transmittance indicated by the molecule responsible for that absorption band. [Ref. 6:p. 114]

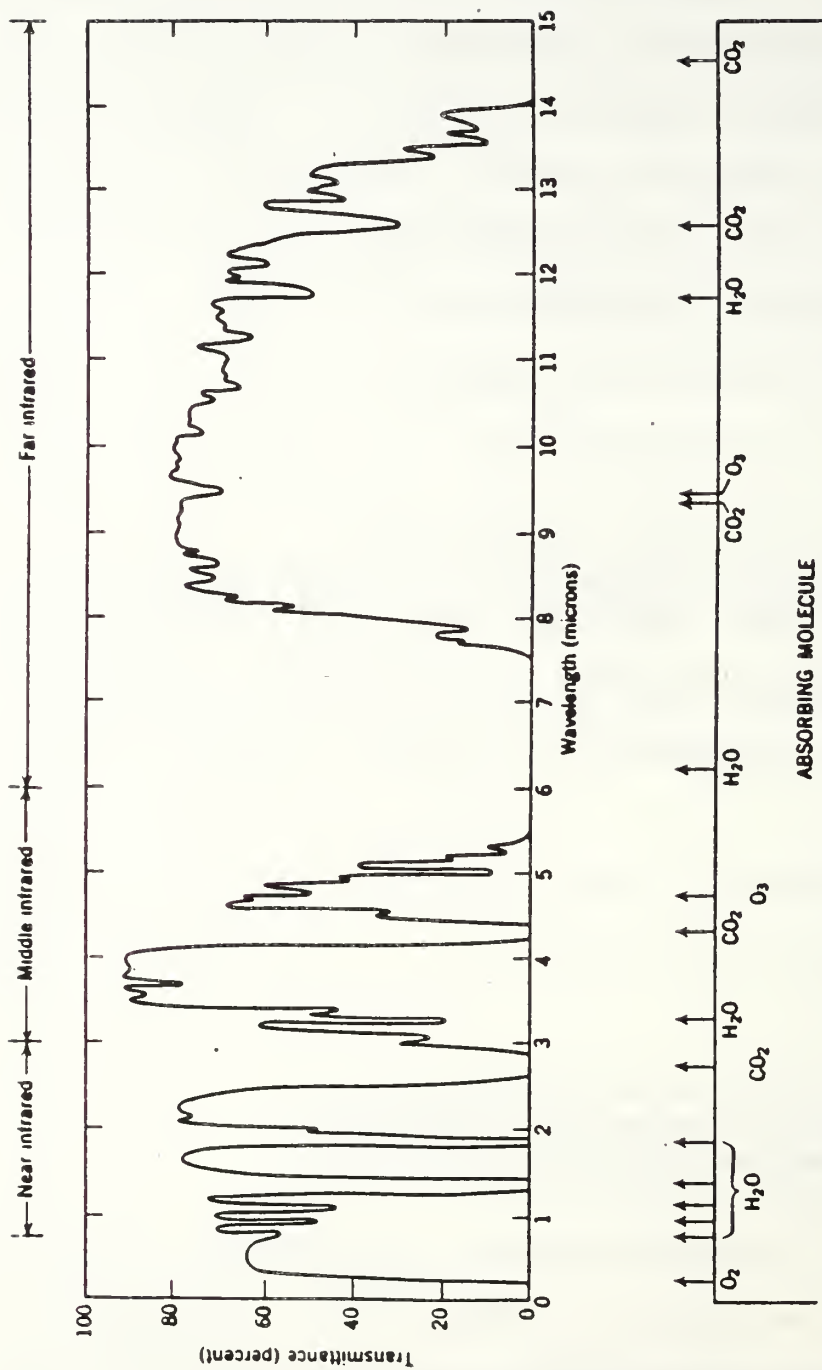


Figure 2.2 Transmittance of the atmosphere for a 6000 ft horizontal path at sea level containing 17 mm of precipitable water (Ref. 6)

Absorption and scattering impact the transmission of infrared energy by restricting it to specific atmospheric windows (wavebands) where these effects are least prominent. The windows most used in remote sensing applications are the 3-5 and 8-14 μm windows. Wavebands outside these windows are unusable due to strong attenuation from absorbing and scattering particles found in the atmosphere.

III. NATURAL INFRARED BACKGROUND SOURCES

Since infrared detection systems operate in an environment comprised of large amounts of thermal clutter, it becomes necessary to codify and understand the nature of all relevant sources of thermal interference a system will encounter. In a marine environment, there are two primary components of naturally occurring IR radiation. The first is energy emitted by the sea itself, due to the fact that it is at some non-zero temperature. The second is thermal radiance, emitted from above the horizon, which is reflected from the sea surface and into a detector's FOV. This sky radiance includes scattered energy from the sun as well as energy emitted by atmospheric molecules and aerosols. [Ref. 3:p. 1]

The total spectral radiance $N_t(\lambda, T)$ (Watts/cm²·sr·μm) which falls on a detecting system (not including solar glitter) at a specific sensor elevation angle with a sea background in its FOV is given by [Ref. 10:p. 3175]

$$N_t(\lambda, T) = \tau(\lambda) \epsilon(\lambda) N_{bb}(\lambda, T_{sea}) + \tau(\lambda) \rho(\lambda) N_{sky}(\lambda) + N_A(\lambda) \quad (3.1)$$

where

$\tau(\lambda)$	=	radiant transmittance at wavelength λ of the path between the sea and the sensor
$\epsilon(\lambda)$	=	radiant emissivity of the sea at wavelength λ
$N_{bb}(\lambda, T_{sea})$	=	spectral radiance of a blackbody at the temperature of the sea
$\rho(\lambda)$	=	radiant reflectance of the sea at wavelength λ

$N_{\text{sky}}(\lambda)$ = spectral radiance of the sky measured at sea level
 $N_A(\lambda)$ = spectral radiance of the atmospheric path between the sensor and the sea surface.

Any radiance within a scene added by sources other than the target makes the task of IR detection more difficult because it alters the contrast between that target and its background. Contrast determines the effectiveness of IR sensors. It is defined as a value between zero (no contrast) and unity (perfect resolution) by the form [Ref. 6:p. 22]

$$C_R = \frac{(W_T - W_B)}{(W_T + W_B)} \quad (3.2)$$

where

C_R = radiation contrast
 W_T = Target radiant emittance
 W_B = Background radiant emittance.

A. SKY SPECTRAL RADIANCE

Atmospheric background radiance is produced by two distinct mechanisms. One is the scattering of the sun's radiation and the other is the thermal emission of atmospheric constituents. Scattered solar radiation is present only during the day and is not significant beyond 3 μm in wavelength, whereas atmospheric emission dominates at wavelengths greater than 4 μm and is present both day and night [Ref. 11:p. 1313].

Figure 3.1 [Ref. 12:p. 3.71] illustrates the separation of atmospheric radiance into these two regions. Clear sky radiance resulting from solar scattering is represented by the solid curve approximately 3×10^{-6} times less intense than the 6000 K (blackbody) sun. The curve for atmospheric thermal emission is represented by a 300 K blackbody curve (corresponding to a mean, surface atmospheric temperature). Overall sky radiance, then, is the sum of these two solid curves for any given wavelength. Measurements of sky radiance should closely follow these model curves, but will be modified by absorption and scattering effects. On clear days, solar glints will further contribute to background clutter for IR sensors aligned near the azimuth of the sun.

1. Atmospheric Path Radiance

Atmospheric self-emission adds energy to a target's source radiance as it travels toward its intended detector by virtue of the fact that the atmosphere is at some temperature above absolute zero. These atmospheric emissions are the inverse of absorptions: when passing into a lower state of energy, molecules emit electromagnetic radiation at wavelengths equivalent to those in the corresponding absorption spectra. The emissivity of the atmosphere in the infrared is consequently dependent upon the concentrations of those gases, water vapor and molecules (O_3 , CO_2 , etc...) which undergo vibrational or rotational transitions corresponding to

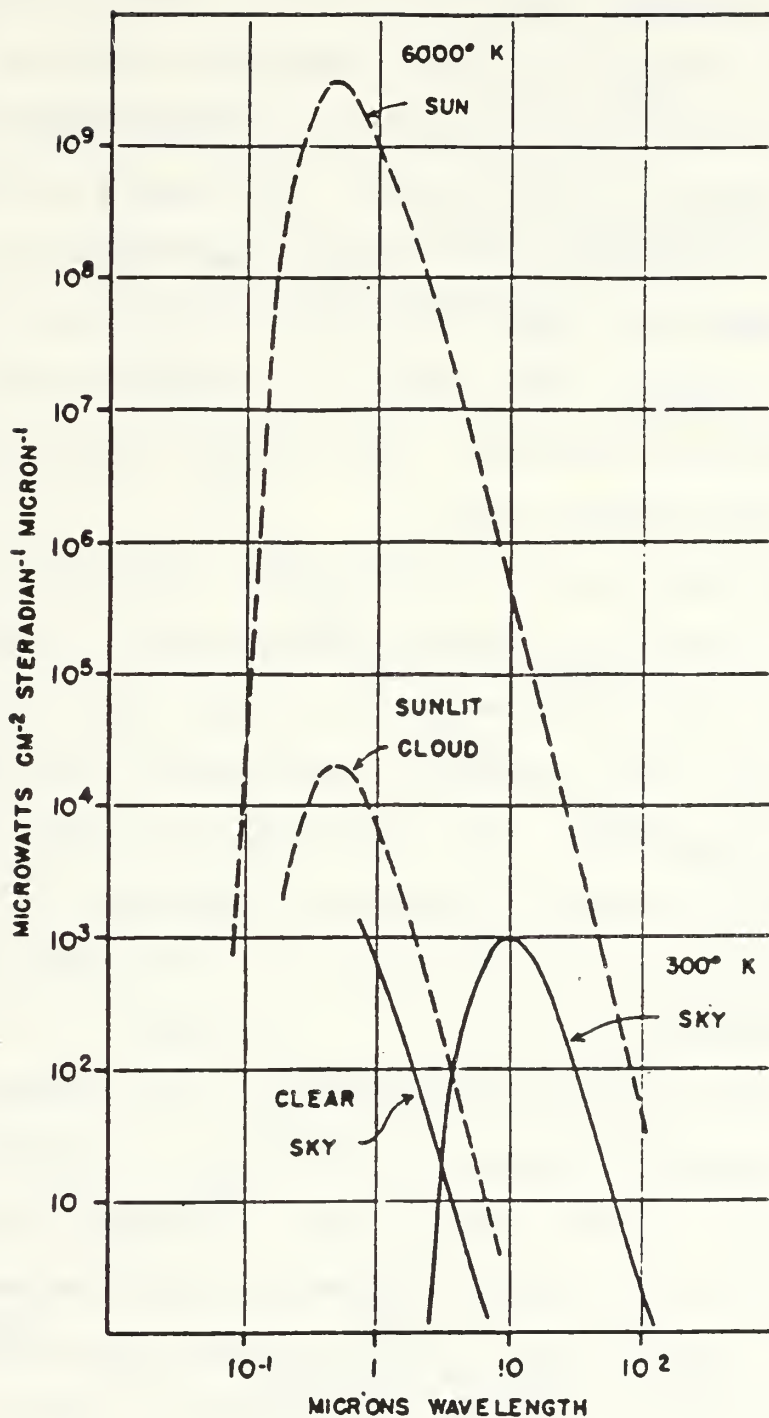


Figure 3.1 Contributions from scattering and atmospheric emission to background radiation (Ref. 12)

quantized thermal energy emissions. Of these, H_2O and CO_2 are the most important [Ref. 8:p. 41]. Thus, for a given atmospheric composition, the absorption spectra will be identical to the emission spectra since both processes follow the same quantum relation, $\Delta E = h\nu$. The impact path radiance exerts upon IR sensing over a long, near-horizontal path is shown in Figure 3.2 [Ref. 13:p. 23]. This figure indicates that path radiance $N(\theta)_p$ equals or exceeds either of the source radiance components: sea surface radiance $N(\theta)_{ss}$ and reflected sky radiance $N(\theta)_{rsk}$.

One factor which influences the impact path radiance has upon a scene is ambient temperature. For a given atmosphere, this establishes (via Wien's law) the general nature of the sky's spectral distribution resulting from thermal self-emission. As illustrated in Figure 3.3 [Ref. 12:p. 3-74], an ambient temperature difference of 25 K can result in a factor of two variation in the radiance produced by an atmosphere.

A second variable contributing to the radiance emitted by the atmosphere between a sensor and a target is path length. For a fixed sensor height, the angle between the horizontal and a target determines the length of the atmospheric path to that target and thus the emissivity of that atmosphere. Longer path lengths result in more atmospheric radiance being emitted into a sensor since near-horizon path lengths become so long as to make the atmosphere

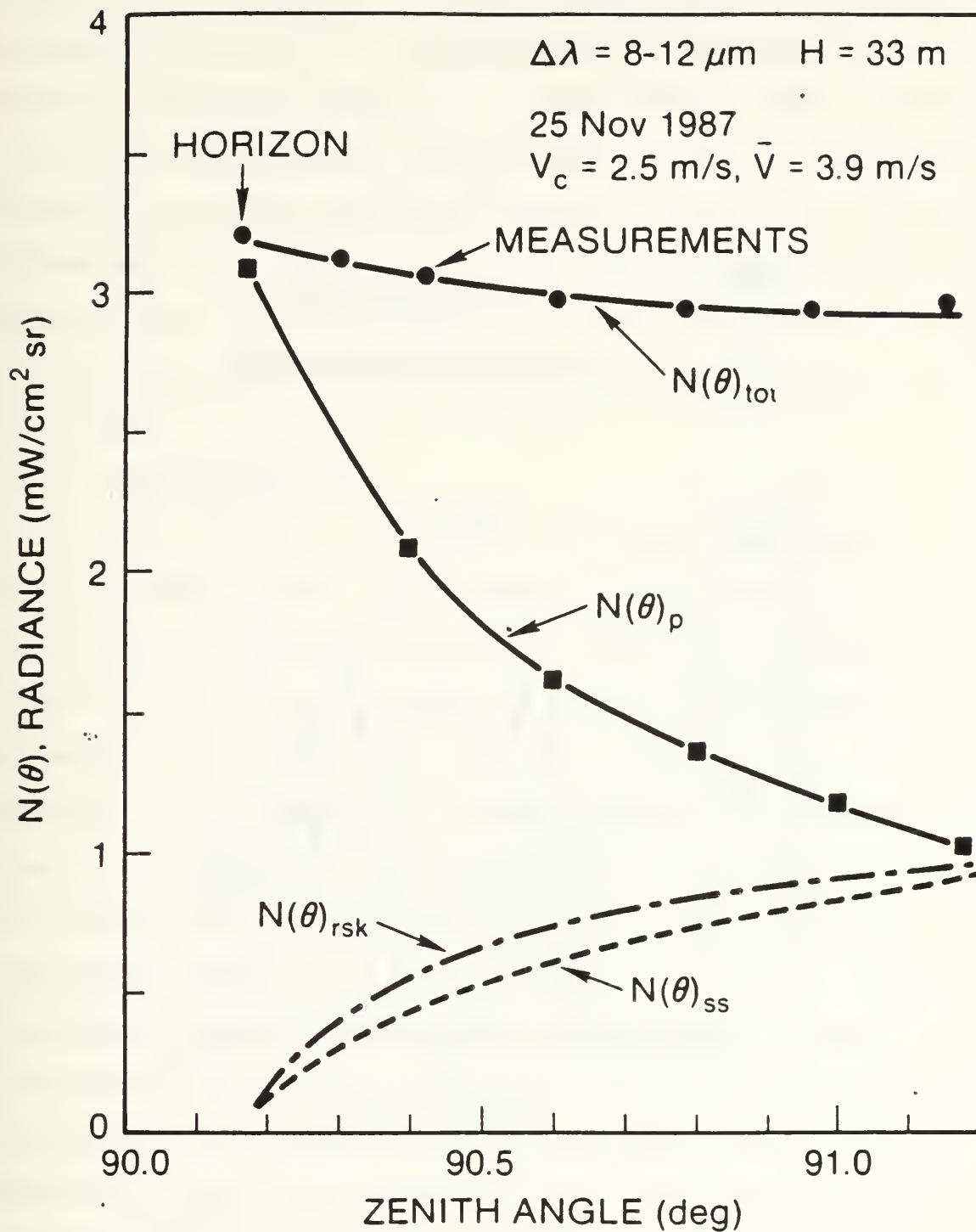


Figure 3.2

Various radiance contributions to a horizon scene imaged in the 8-12 μm waveband (Ref. 13)

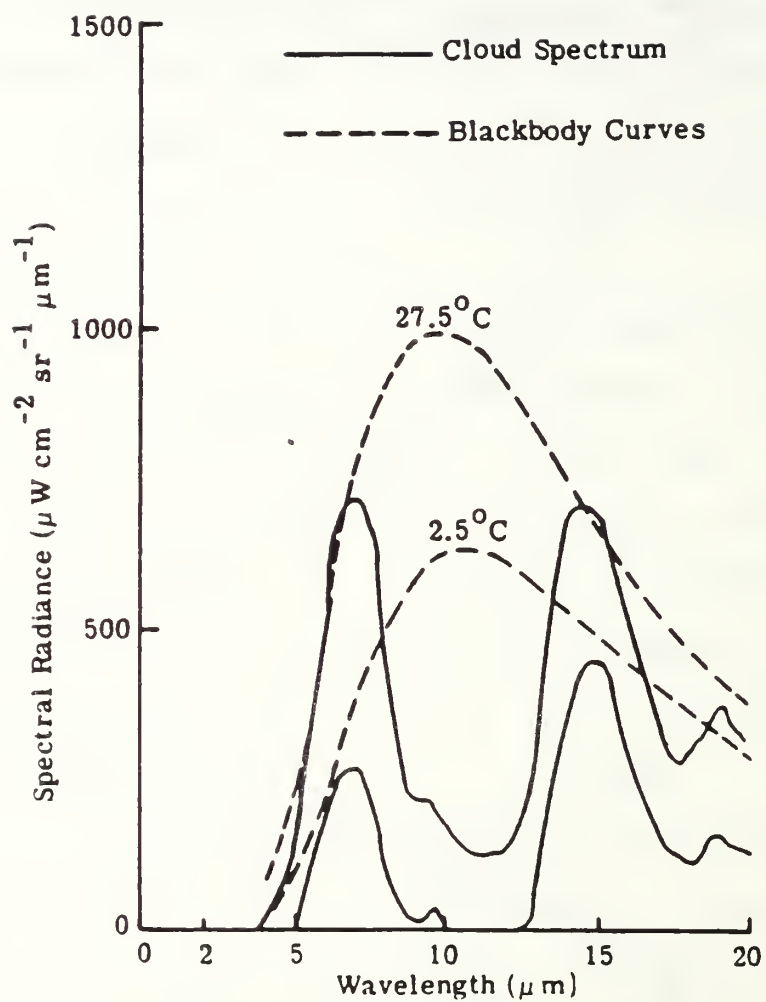


Figure 3.3

Two zenith skies' spectral radiances showing the large variation with ambient air temperature (Ref. 12)

behave as a blackbody. A plot of the night sky radiance measured by a sensor at a fixed height over varying elevation angles is shown as Figure 3.4. This confirms that for the 0° (horizon) measurement, the sky most closely resembles a blackbody, and that for path lengths through less air mass (higher elevation angles), regions of lower strength emissions tend to fade. Note the strong water vapor and carbon dioxide emission bands centered at 6.3 and $15\text{ }\mu\text{m}$, respectively. [Ref. 11:p. 1315].

2. Solar Scattering

The sun is a class G star which can be modeled as a 5900 K blackbody source. Its spectral irradiance both outside of the earth's atmosphere and at sea level is illustrated in Figure 3.5, showing maximums in the visible region with little subsequent energy beyond $3\text{ }\mu\text{m}$ [Ref. 12:p. 3-34]. In the infrared, solar radiation scattered through the atmosphere forms an extended source spanning the entire hemisphere above the sea surface. Its radiance ($N_{\text{sky}}(\lambda)$) is also a function of temperature insofar as atmospheric temperature affects atmospheric density (the scattering medium). Figure 3.1 illustrated the extent to which the earth's atmosphere attenuates the exoatmospheric sun's radiance. Sensor angular dependence upon the scattered solar radiation a system receives, however, is shown in Figure 3.6 [Ref. 11:p. 1320]. This figure illustrates that for a sun zenith angle of

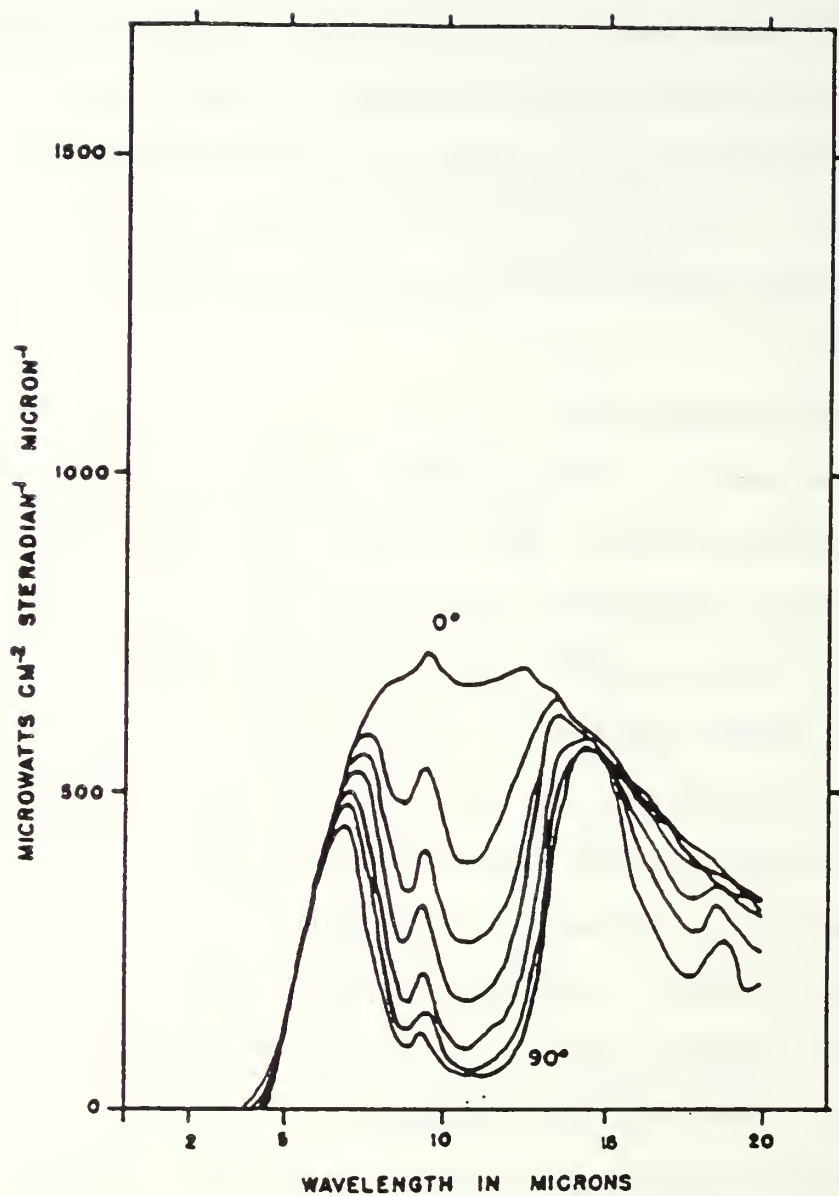


Figure 3.4

The spectral radiance of a clear night sky for several angles of elevation above the horizon, $T_{\text{ambient}} = 8^{\circ}\text{C}$ (Ref. 11)

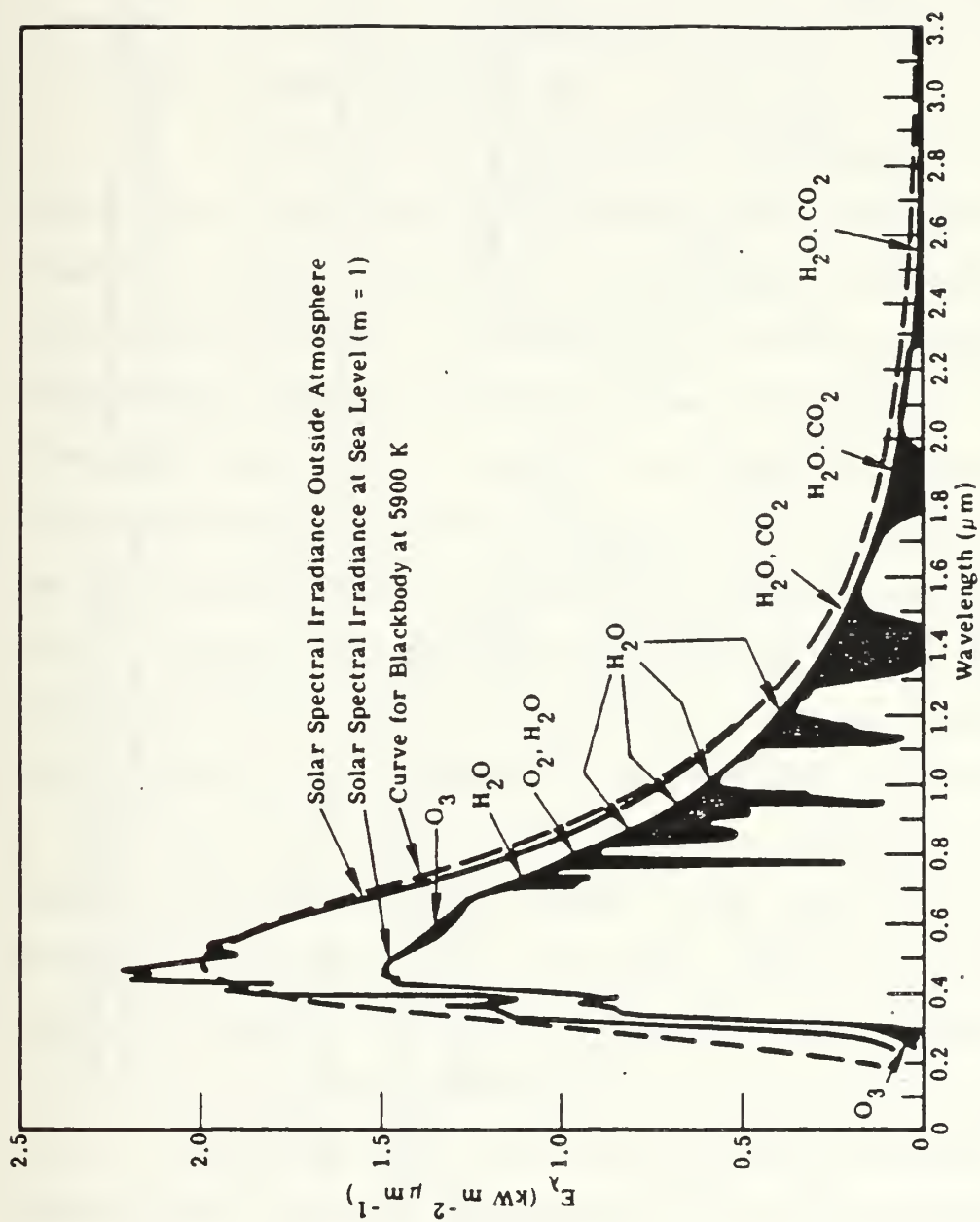


Figure 3.5

Spectral distribution curves related to the sun. Shaded areas indicate absorption at sea level due to atmospheric constituents (Ref. 12)

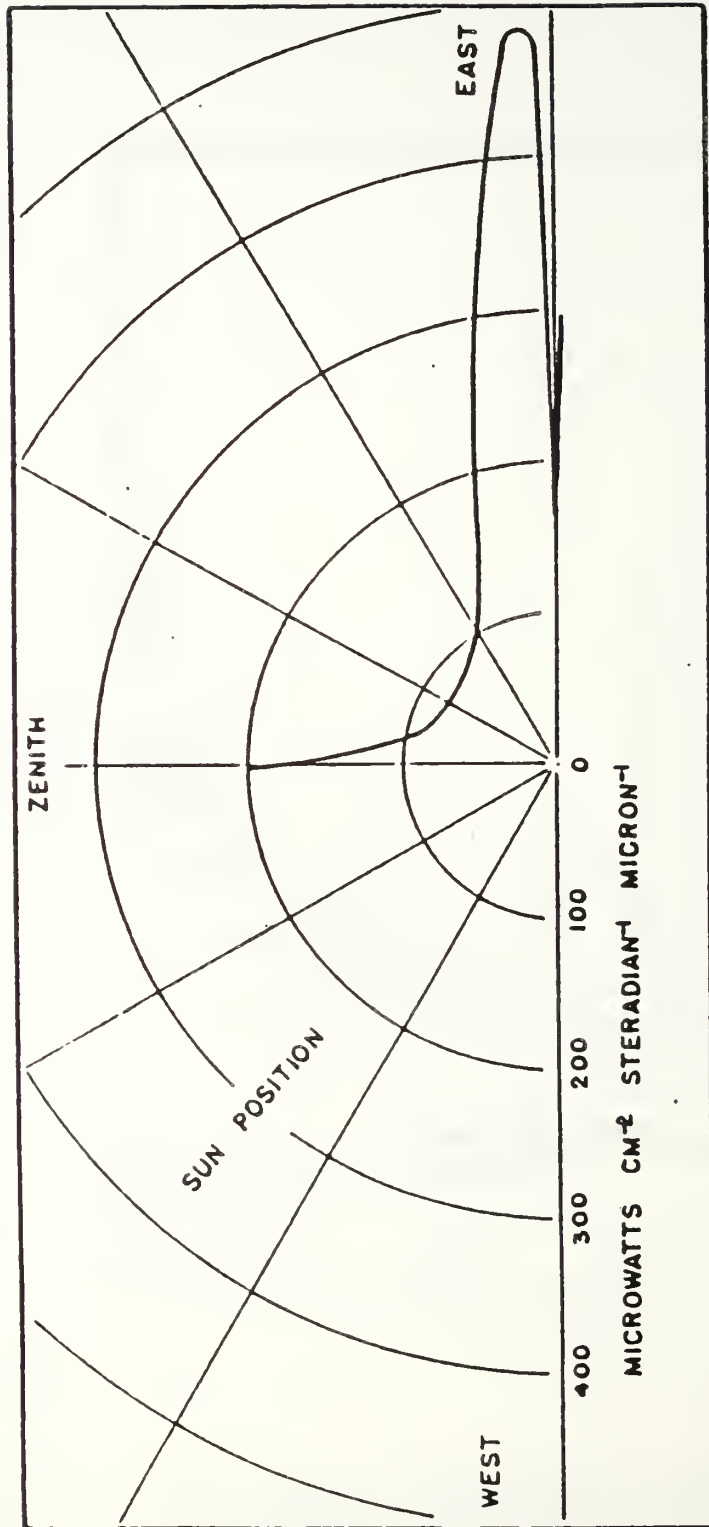


Figure 3.6 The spectral radiance of a clear sky at 1.13 μm wavelength showing the sensor elevation dependence of solar scattered radiation (Ref. 11)

approximately 42° , scattered solar radiance increases as the sensor elevation angle looks more toward the horizon. Such an increase is the result of the longer path through the atmosphere over which scattering can occur.

a. Clear Sky Radiance

Part of the mean radiance received from the sea comes from solar energy scattered by the atmosphere. This energy is emitted from the sky as though from an extended hemispherical source. It reflects off the sea surface at the appropriate viewing geometry to be received by a sensor. Clear sky radiances are generally low compared to overcast sky radiances because the window regions which are defined by low absorption bands are also regions of low emission [Ref. 16:p. 646]. Greater path lengths enhance the radiance emitted by scattered solar radiation due to the increase in scattering media, making near-horizon atmospheres appear almost black. A clear sky, then, has maximum radiance near the horizon and minimum radiance at the zenith. The total sky radiance entering a detector is, therefore, dependent upon that sensor's elevation angle with respect to the horizon.

Accurate predictions of mean ocean radiance must include computations of the magnitude of scattered solar energy which reflects from the sea surface under both clear and overcast conditions. Effective models have already been developed which give these radiance values. For maritime use,

two models are especially suitable: the SKYRAD code developed by the Naval Surface Weapons Center (NSWC) and the LOWTRAN code developed at the Air Force Geophysics Lab (AFGL) [Ref. 3:p. 9].

Additionally, several empirically based single equation models of clear sky radiance from solar scattering have been developed. One model presented by Levesque [Ref. 14:p. 357] describes a clear sky's radiance at sea level as a function of zenith angle, in which the effective blackbody temperature of the sky at a zenith angle of θ is given by

$$T(\theta) = T_{zenith} + (T_{ambient} - T_{zenith}) (\theta/2\pi)^{5/2}, \quad (K) \quad (3.3)$$

where T_{zenith} is usually 50-60 K colder than ambient temperature. Using the temperature $T(\theta)$ from Equation (3.3), the sky radiance would then be

$$N_{sky}(\lambda_1, \lambda_2, \theta) = W(\lambda_1, \lambda_2, T(\theta)) / \pi, \quad \left(\frac{\text{watt}}{\text{cm}^2 \cdot \text{sr}} \right). \quad (3.4)$$

Lacking some means to obtain T_{zenith} empirically, the total thermal irradiance for a clear sky at ground level H_{sky} can be estimated from the empirical relation of Idso-Jackson [Ref. 12:p. 3-76], based on a surface meteorological air temp T_A (K) by

$$H_{sky} = \sigma T^4 (1 - 0.261 \exp[-7.77 \times 10^{-4} (273 - T_A)^2]), \quad (\text{watt/cm}^2) \quad (3.5)$$

In the absence of either of the two computer codes LOWTRAN or SKYRAD, these methods are convenient to compute clear sky radiances N_{sky} but are not as accurate.

b. Overcast and Cloudy Sky Radiance

In the presence of clouds the thermal characteristics of the sky are apt to change dramatically. As previously stated, sky radiances are higher under overcast conditions than under clear conditions for the same exoatmospheric solar irradiance. For a mostly overcast sky, the overall radiance as viewed from the ground can be represented by a cardioidal distribution according to the following relation found in Jerlov's *Marine Optics* [Ref. 15:p.69]

$$N(\theta_{zenith}) = N\left(\frac{\pi}{2}\right) (1 + A \cos \theta_{zenith}), \quad \left(\frac{\text{watt}}{\text{cm}^2 \cdot \text{sr}}\right) \quad (3.6)$$

where $A=1$ for arctic skies and skies over snow; otherwise $A=2$. Given accurate meteorological inputs, though, LOWTRAN and SKYRAD will compute the sky radiance for any weather conditions including cloudy and overcast.

Clouds consist of locally high concentrations of water vapor and atmospheric gases. They may not be visible within regions of high absorption, such as at $6.3 \mu\text{m}$ (H_2O) and $15.0 \mu\text{m}$ (CO_2). Outside of these bands and especially in the

8-13 μm window, however, clouds are strong thermal emitters by virtue of their enhanced density. Yet due to their strong absorptive characteristics, clouds are considered essentially opaque to infrared radiation. Couple this with their low reflectivity, and the emissivity for clouds approaches unity. Figure 3.7 illustrates the radiance characteristics of clouds, showing that they generally follow Planck's Law for their temperature (-10°C) except in the 6.3 and 15.0 μm absorbing regions, where atmospheric emissions dominate. [Ref. 11:p. 1318]

Clouds and their infrared signatures are important to remote IR sensing in the marine environment in two ways. First, they increase the above horizon radiance which ultimately reflects off the surface of the ocean; this in turn increases the radiance reaching an IR detector aimed toward the sea surface. Second, under a broken cloudy sky, individual clouds passing over a scene act as localized sources of IR energy which produce non-uniform reflections off the sea surface. From a modeling standpoint, then, overcast and broken cloudiness conditions are the most difficult to account for due to the unpredictability of the size, shape and movement of clouds.

B. SEA SURFACE RADIANCE

This section will discuss the essential nature of sea water relevant to the computation of the infrared radiation

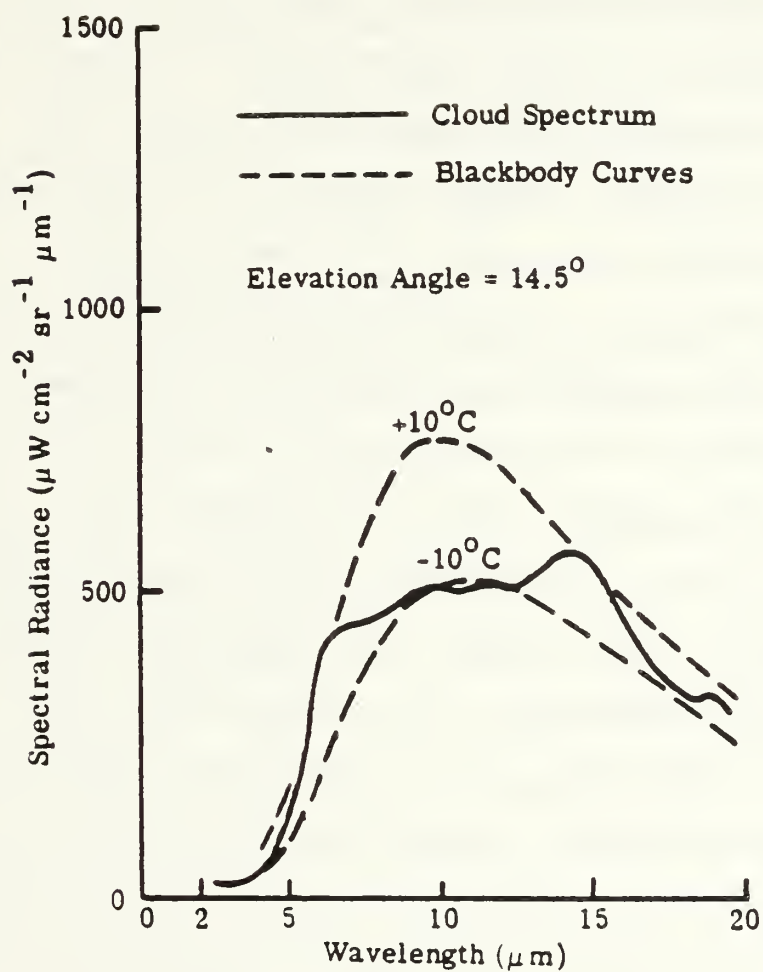


Figure 3.7

The spectral radiance of a cumulus cloud. The dashed curves represent blackbodies at air temperature ($+10^\circ\text{C}$) and cloud temperature (-10°C) (Ref. 11)

received from its surface. These fundamentals will be used in the model described in Chapter IV of this thesis, which will further incorporate equations pertaining to sea surface roughness to describe fully the IR radiance of the ocean.

1. Ocean Thermal Emission

As mentioned previously, part of the sea's overall radiance results from the self-emission of ocean water by virtue of it being at some temperature greater than absolute zero. Water, however, strongly absorbs infrared radiation at wavelengths longer than $3\text{ }\mu\text{m}$. The sea surface may thus be considered opaque to infrared radiation greater than $3\text{ }\mu\text{m}$ in wavelength. Any upwelling IR radiance from layers of water below the surface is attenuated before reaching the air-water boundary. As a result, only the uppermost few millimeters contribute to the self-emission of the sea surface. [Ref. 12:p. 3-105] Care should be exercised during field experiments when measuring the self-emission from a given ocean scene in that bulk water temperature measurements may not accurately represent temperatures in the emitting region nearest the surface. A good representation of sea's self-emission, then, would be the product of the blackbody radiant exitance corresponding to the temperature of the sea surface and the emissivity for the specific wavelength and view angle being used.

2. Reflectivity and Absorptivity of Smooth Sea Water

For an opaque body such as the sea surface, Kirchhoff's Law (Equations (2.5) and (2.6)) showed that emissivity and reflectivity vary inversely. Ignoring the effects of surface roughness and polarization, sea surface reflectivity and emissivity are known to be strong functions of viewing angle. Values for calm sea reflectance and emissivity averaged over the 2.0-15.0 μm waveband are plotted in Figure 3.8 [Ref. 12:p. 3-106]. This figure shows that when viewing an unroughened sea surface from the normal, reflectance will be minimum and emission maximum, whereas the opposite is true for viewing the same scene within 10° of the horizon.

The total radiance emanating from the sea surface (excluding sun glints) combines the separate radiances of sea self-emissions and reflected sky emissions (or reflected solar scattered radiance). This value of sea surface radiance is, therefore, a function of sensor viewing angle because the reflectance and emissivity of sea water are strong functions of elevation angle. Thus, the expression for sea surface radiance N (watts/cm²·sr) is

$$N_{ss}(\theta, \lambda) = [\epsilon(\theta, \lambda) N_{bb}] + [\rho(\theta, \lambda) N_{sky}(\theta)] \quad (3.7)$$

where

- θ = sensor view angle below zenith
- ϵ = sea surface emissivity as a function of view angle and wavelength

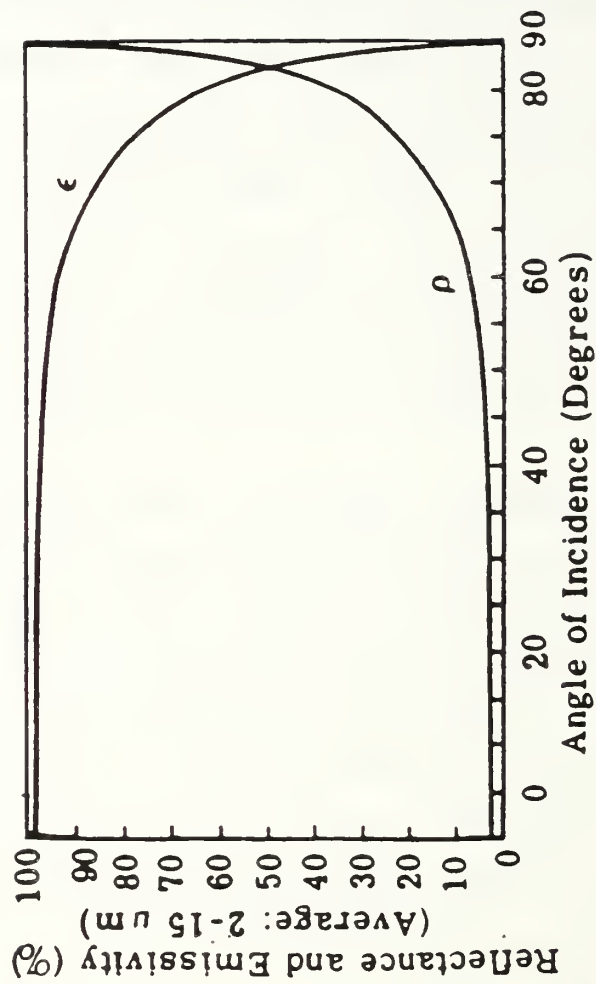


Figure 3.8 Reflectance and emissivity of a smooth water surface versus angle of incidence, averaged over 2-15 μm (Ref. 12).

N_{bb} = in-band blackbody radiance corresponding to sea surface temperature
 ρ = sea surface reflectivity as a function of view angle and wavelength (unpolarized)
 N_{sky} = in-band scattered solar radiance as a function of view angle.

The trends of emissivity and reflectivity with respect to angle as they affect sky radiance and sea self-emission are illustrated in Figure 3.9, where N' is the radiance of the sky, B is the radiance of a blackbody at the sea temperature of 15° C, and N is the total radiance from the sea surface, related by the expression $N = \epsilon B + N' \rho$ [Ref. 16:p. 646]. At the horizon where ϵ approaches zero and ρ approaches unity, the radiances of the sea and sky appear to merge into one another. This explains why for a calm sea the horizon is difficult to detect, whereas for a wind ruffled sea the distinction between the sea and sky is easier to view as the roughness causes the sea to apparently reflect less and emit more. Note the impact a single cloud would have as a strong IR source reflecting off the sea.

3. Solar Glitter

Solar glitter or glint results from specular reflections of sunlight from appropriately oriented wave facets. These direct solar reflections are usually the most intense of all thermal radiation components from the sea. On average they will be 1000 times more intense than either self-emissions or sky reflections along azimuths near the sun [Ref.

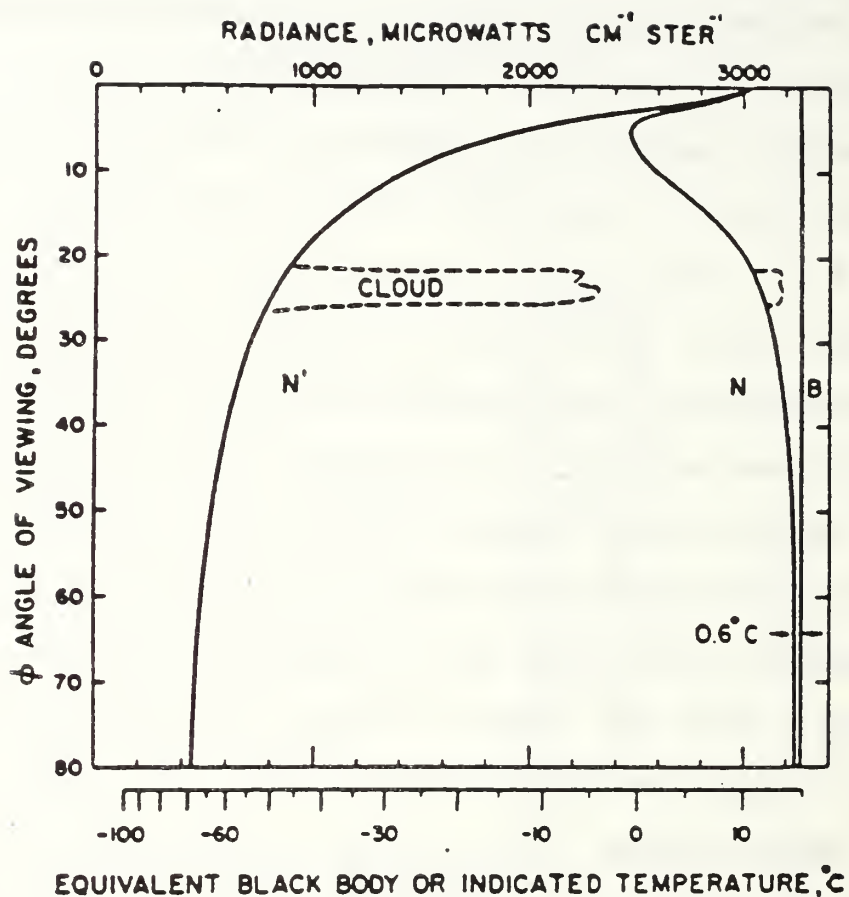


Figure 3.9

Typical distribution of the radiance of a calm sea N and sky N' in the 8.35-12.5 μm waveband (Ref. 16)

4:p.44], [Ref. 17:p. 207]. The spectral radiance of the sun reflected specularly by a smooth water surface is

$$N(\omega, \lambda) = \rho(\omega, \lambda) \tau(\lambda) N_0(\lambda), \quad \left(\frac{\text{watt}}{\text{cm}^2 \cdot \text{sr} \cdot \mu\text{m}} \right) \quad (3.8)$$

where

$\rho(\omega, \lambda)$ = surface reflectivity for incidence angle ω
 $N_0(\lambda)$ = exoatmospheric spectral radiance of the sun
 $\tau(\lambda)$ = spectral transmittance of the atmosphere between the sun and the water surface.

Additionally, for a calm sea the radiance from sun glitter would be greater at lower solar angles (with resultant grazing viewing geometry) where reflectance reaches its maximum values. Assuming equal sea surface reflecting areas, the intensity of glints for the sun at 20° above the horizon is an order of magnitude greater than those for the sun at 80° above the horizon [Ref. 5:p. 19].

Levesque [Ref. 14:p. 356] presents a model of glitter radiance as a function of the sun's irradiance modified by energy losses due to range and transmissivity. Scattering losses are detailed by the Henyey-Greenstein phase function $\phi(\psi)$ where $\psi=0$ is the direction of sunlight propagation without scattering. For the waveband from λ_1 to λ_2 at a solar zenith angle of θ_{sun} , the radiance at sea level is

$$N_{\text{sun}}(\lambda_1, \lambda_2, \psi) = H_{\text{sun}}(\lambda_1, \lambda_2, T_{\text{sun}}) \tau(\lambda_1, \lambda_2, \theta_{\text{sun}}) \phi(\psi), \quad \left(\frac{\text{watt}}{\text{cm}^2 \cdot \text{sr}} \right) \quad (3.9)$$

given the sun's irradiance of

$$H_{sun}(\lambda_1, \lambda_2, T_{sun}) = \left[\frac{R_{sun}}{D_{sun}} \right]^2 W(\lambda_1, \lambda_2, T_{sun}), \quad (\text{watt/cm}^2) \quad (3.10)$$

where

$$\begin{aligned} W(\lambda_1, \lambda_2, T_{sun}) &= \text{in band radiant exitance for a 5900 K blackbody} \\ \tau(\lambda_1, \lambda_2, \theta_{sun}) &= \text{atmospheric transmission for the } \lambda_1 \text{ to } \lambda_2 \text{ waveband} \\ D_{sun} &= \text{sun's distance from Earth } 149.68 \times 10^6 \text{ km} \\ R_{sun} &= \text{sun's radius } 695000 \text{ km} \\ \varphi(\psi) & \end{aligned}$$

$$= \frac{1}{4\pi} \frac{(1-G^2)}{(1+G^2-2G \cos \psi)^{3/2}} \quad (3.11)$$

$G = 0.8$ for Rayleigh Scattering.

The impact of solar glitter upon IR sensing is best illustrated by computing the amount of reflecting sea surface area required to produce a significant glint signal. First, the in-band solar irradiance reaching sea level must be computed. For the solar constant of 1360 W/m^2 and a $0.2 \text{ } \mu\text{m}$ waveband centered at $4 \text{ } \mu\text{m}$ (equivalent to 0.14050% of the solar spectrum [Ref. 12:p. 3-36]), the in-band radiant emittance of the sun will be 1.91080 W/m^2 at mean earth-sun distance. This power density is radiated within a solid angle equal to that of the solar disk in the sky, $1.9\pi \times 10^{-5} \text{ sr}$, yielding an in-band solar irradiance of $3.2 \text{ W/cm}^2 \cdot \text{sr}$. This energy then specularly reflects off a wave facet over an area assumed to be within the FOV of the receiving sensor (valid for the AGA 780 pixel

size of $2.42\pi \times 10^{-5}$ sr). Assuming a view angle of 45° for which reflectivity is 0.03, the area necessary to produce a radiant intensity of $1 \text{ watt} \cdot \text{sr}^{-1}$ can be found from

$$1 \text{ Watt/sr} = \rho(\omega, \lambda) \cdot \text{Area} \cdot \cos(\theta_{\text{view}}) \cdot H_{\text{sun}}(4\mu\text{m}) \quad (3.12)$$

where

H_{sun} = spectral solar radiance
 Area = the surface area of the glint
 θ_{view} = the angle of incidence (45°)
 $\rho(\omega, \lambda)$ = the reflection coefficient

therefore

$$\text{Area} = \frac{1}{(.707)(.03)(3.2)} \approx 15 \text{ cm}^2. \quad (3.13)$$

Thus an area nearly 3.87 cm^2 will act as a source of direct solar reflected radiance equal to $333 \text{ mW} \cdot \text{cm}^{-2} \cdot \text{sr}^{-1} \cdot \mu\text{m}^{-1}$. By comparison, $4 \mu\text{m}$ sky radiances as read from Figures 3.1 and 3.4 are approximately $1 \text{ mW} \cdot \text{cm}^{-2} \cdot \text{sr}^{-1} \cdot \mu\text{m}^{-1}$ which when multiplied by .03 reflectance yields a non-glinting sea radiance of $30 \mu\text{W} \cdot \text{cm}^{-2} \cdot \text{sr}^{-1} \cdot \mu\text{m}^{-1}$. This represents a 50 dB difference between glinting and non-glinting sea surfaces radiances. [Ref.5:p.19]

It is apparent, then, that sun glints can be very difficult to counteract when they comprise part of an ocean's IR background. Not only are they locally intense, tending to saturate detectors and processing circuitry, but during periods when solar angles are low, they are spatially broad enough to block entire angular sectors from an IR sensor's FOV.

IV. A MODEL OF THE WIND ROUGHENED SEA SURFACE

The problem of calculating the mean radiance from a sea surface background involves considering many individual sources of IR energy. Further complicating maritime IR radiance measurements is the seemingly endless motion of the sea resulting from wind interactions with the ocean surface. If the sea were perfectly calm, the sun would specularly reflect off the sea at the *horizontal specular point*. When the sea is roughened by an external force such as wind, the image of the sun is observed as a collection of individual highlights. Each wave facet will reflect toward an observer when the local slope of the surface at that point is momentarily oriented in such a way that the sun is specularly reflected in the direction of the observer. The farther the individual facet is from the horizontal specular point, the larger the inclination must be to produce a reflection off the rough sea. For example, when viewing the sea at one degree below the horizon, a glint region would be 40° wide in azimuth for surface slopes of 30° [Ref. 5:p. 17]. The term *sun glitter*, then, refers to the appearance of many such highlights as viewed over an extended region near the azimuth of the sun.

For the case of a clutter pattern where the area corresponding to the projection of a sensor's FOV onto the

ocean surface is greater than the length scale of the facets, the apparent intensity would be the spatial average of many such unresolved highlights weighted by the probability density function for facet orientation. The distribution of sun glitter is therefore closely related to the distribution of surface slopes [Ref. 1].

For a shipboard IR sensor, there are two distinct aspects of sunglitter which affect operations. Near sunrise or sunset when the sun is low in the sky, the glitter pattern appears confined to a bright, narrow corridor of closely spaced individual highlights. This pattern is brightest along the azimuth of the sun and diminishes symmetrically on either side of this angle. As the sun rises higher in the sky during the day, the pattern appears to spread out and individual reflecting facets become more distinct from one another. When the sun is near zenith, the pattern appears to lose its distinct corridor shape and is characterized instead by widely dispersed "glints" that occur randomly both in position and time over large areas.

The reason for the difference in appearance of the glitter pattern for varying solar angles lies in the manner in which wave slopes are distributed as a result of wind and sea interactions. For any given wind condition, shallow wave slopes occur with much greater frequency than steep slopes. Shallow slopes tend to produce appropriate reflection geometries for an observer viewing the sea when the sun is

close to the horizon. The density of highlights in this situation is so great as to produce a seemingly continuous and stationary pattern that masks most individual fluctuations. An increase in wind speed will periodically generate waves of greater slopes, but will not change the fact that shallow wave slopes still predominate. For the case where the sun is high in the sky, only steep slopes produce the correct reflection geometry for a near grazing observation angle. Since steep slopes occur less frequently than shallow slopes, the occurrence of individual glints would be a rare event by comparison. An IR sensor could easily employ temporal processing to prevent such infrequent glinting from appearing as false targets.

Preventing glints from acting as false targets in the case of low solar angles, however, is not as easily achieved since detectors and processing circuitry are likely to become saturated by the higher concentration of specular highlights in a given area. The remedy to this situation involves an understanding of the nature of wind/sea interactions, and how these impact the appearance of a glitter corridor for given sun and observation angles. [Ref. 18:p. 236]

This chapter will detail those aspects of the rough sea surface that affect the radiance received from it. Central to this discussion will be the development of a probability distribution which describes naturally occurring wind generated waves. From such a distribution, the fraction of

the sea's surface causing reflections can be found, which in turn relates the amount of solar radiance reflected from the sea to that which reaches sea level from the sun. The intent of this work, then, is to find a statistical description of sun glitter such that its effects can be countered within shipboard IR sensing systems.

A. ROUGH SEA EMISSIVITY AND REFLECTIVITY

Sea roughness can experience great swings in both spatial and temporal variability as a direct result of the forces that generate waves. Sea waves range from small wind-driven capillary waves to long waves caused by storms and earthquakes. Most of the energy within the wave spectra is contained in an intermediate band consisting of wind driven waves [Ref. 10:p. 3174]. As a consequence, these waves will predominate in causing solar reflections and will be the only type of surface disturbances included in the derivation of this wave slope model.

In order to simplify sea radiance calculations, variations in sea surface temperatures resulting from currents or local turbulence are assumed to be negligible within the FOV of a sensor. Additionally, local variations in sky radiance are assumed to be negligible over short periods and within the narrow FOV of shipboard IR sensors. This leaves only variations in the sea's emissivity and reflectivity resulting

from the tilt angle of waves as the cause of all variations in sea radiance over short length and time scales.

As the wind acts upon a sea surface to tilt waves away from the horizontal, the sea surface becomes a collection of individual facets. Each of these waves is capable of reflecting radiance originating above the horizon from the direction corresponding to its tilt. When an ocean surface roughened by winds is viewed near grazing, most of the facets seen by the sensor are tipped away from the horizontal toward the sensor. This phenomenon affects both the amount of radiation emitted from the sea and the amount of radiation reflected from the sky. The radiance from a sea surface, then, depends upon the slope distribution and orientation of the surface which in turn is dependent on wind speed.

If the radius of curvature of each wave's surface is large compared to the wavelength of incoming light, then it is possible to consider the surface to be locally flat. The surface roughness, then, is reduced to a distribution of plane facets with varying orientations. Additionally, if the size of these facets is large compared to the wavelength of the light, a geometric optics approximation may be made which allows each facet to emit and reflect energy specularly. The large wavelength of ocean waves readily allows this assumption in the IR. [Ref. 19:p. 5]

In the case of a perfectly smooth sea, the unpolarized reflectance at the horizon is unity and the radiance along a

grazing angle is comprised only of reflected skylight from immediately above the horizon. For this situation, emissivity is zero. Therefore, there would be no contrast at the horizon and the sea would be indistinguishable from the sky immediately above it except near the azimuth of the sun. As the sea becomes rough, wave slopes act to reduce the reflectivity and increase the emissivity of the sea as though the view angle had been changed. Since sky radiation decreases sharply with increasing elevation angle, the effect of sea roughness will be a decrease in the radiation reflected from the sky. The overall radiance of a rough sea as viewed at grazing incidence, then, is a combination of the thermal emission from wave facets as well as the reflected sky and sun light from those facets. The impact of wave slopes upon IR sensing is twofold: that radiation from elevation angles higher in the sky is reflected than would be the case if the sea were not rough and that the sea's thermal emission increases over that of a flat surface for low observation angles.

Solar glitter only becomes significant when a large fraction of the sea surface is capable of reflecting light from the sun's direction. When the appropriate wave slopes and viewing geometry exist, solar glitter will dominate all other radiance contributions and the sea will appear much brighter than the sky, which is a reversal of what normally

occurs outside of a sun glitter corridor [Ref. 20:p. 2].

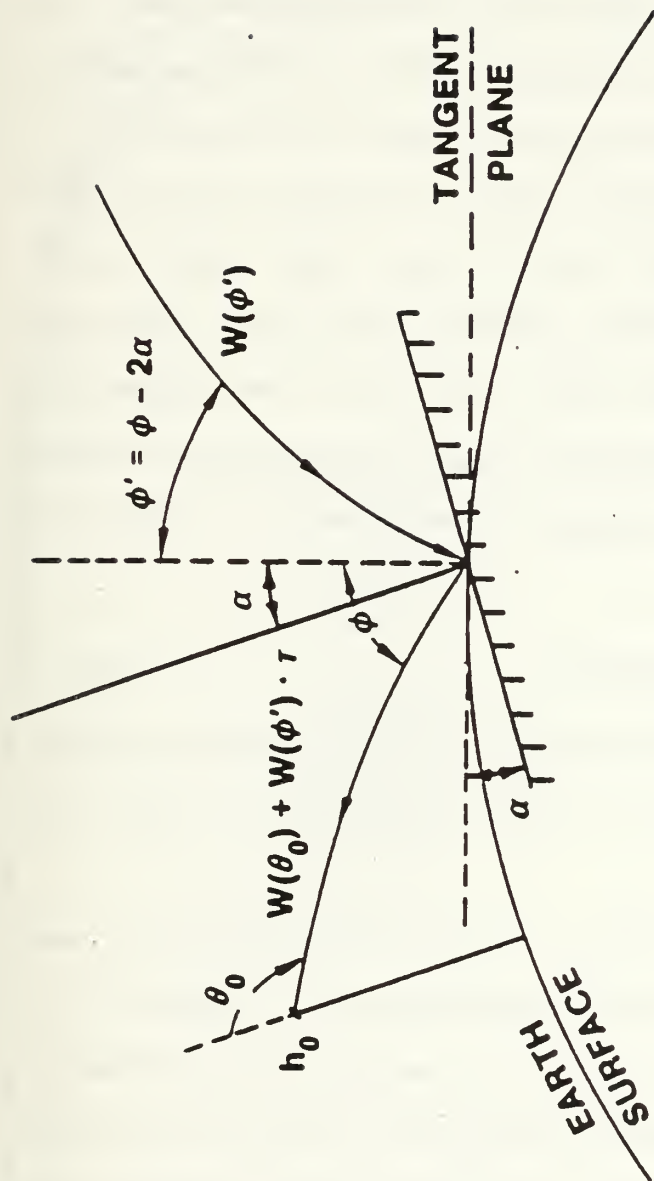
1. The Schwartz-Hon Model of Rough Sea Emissivity

As described in Section III.B.2, emissivity and unpolarized reflectivity are functions of wavelength and local angle of incidence. The expression $\epsilon_\lambda = 1 - \rho_\lambda$ (Equation (2.6)) relates these two quantities for opaque bodies such as water at wavelengths above 3.0 μm . Wind roughened sea water emissivities differ from flat sea emissivities by virtue of the variations in local incidence angles caused by tilted wave slopes.

The Schwartz-Hon algorithm was developed at the Naval Research Laboratory as a computer model to calculate the reflectances (and thereby, emissivities) of the wave-roughened sea surface as a function of view angle. [Ref. 21] Assumptions inherent in their model are:

- the surface emits at a constant temperature
- emissivity is a function of the surface roughness only
- the surface is composed of many contiguous flat surfaces
- for a flat section of the sea surface, water has reflectivity which is a function of view angle with respect to the surface normal (computed from the Fresnel equations). From this, a facet's emissivity can be calculated by $\epsilon = 1 - \rho$.

The sea surface viewing geometry germane to the Schwartz-Hon model is presented in Figure 4.1 [Ref. 21], showing the



- θ_0 = Zenith angle at observer height, h_0
 ϕ = Zenith angle at reflection point (tangent surface)
 ϕ' = Zenith angle at reflection point (tilted surface)
 α = Wave tilt
 W = Radiance
 τ = Atmospheric transmittance between observer and reflection point

Figure 4.1 Geometry of the sea surface for the Schwartz and Hon algorithm (Ref. 21)

relationships between viewing, incident and reflection angles for calm and rough seas. The model requires inputs of wind speed and view angle. It finds the spatially averaged slopes of many individual wave facets around a viewing point as defined by the user. Light rays are then projected back to the sensor from those facets which have the correct geometry for viewing. The overall emissivity is then calculated as a spatial average of emissivities over all facets within the 'footprint' for a wavelength of 10 μm . The model also calculates an effective incidence (zenith) angle for incoming sky radiance (θ_R) associated with the mean wave slope by assuming that the average emissivity over the footprint is due to a single, large sloping surface of smooth water, using the relationship

$$\theta_R = \theta_i - 2\alpha \quad (4.1)$$

where α is the local elevation angle of the sloping surface and θ_i is the zenith angle of the reflected ray from the surface.

This model's improvements to the calculation of sea surface emissivity are illustrated graphically in Figure 4.2. This figure shows that for a calm sea, emissivity decreases from a value of unity at normal viewing to a value of zero at grazing view angles, but that for rough seas emissivity decreases to some positive, minimum value at grazing [Ref. 21].

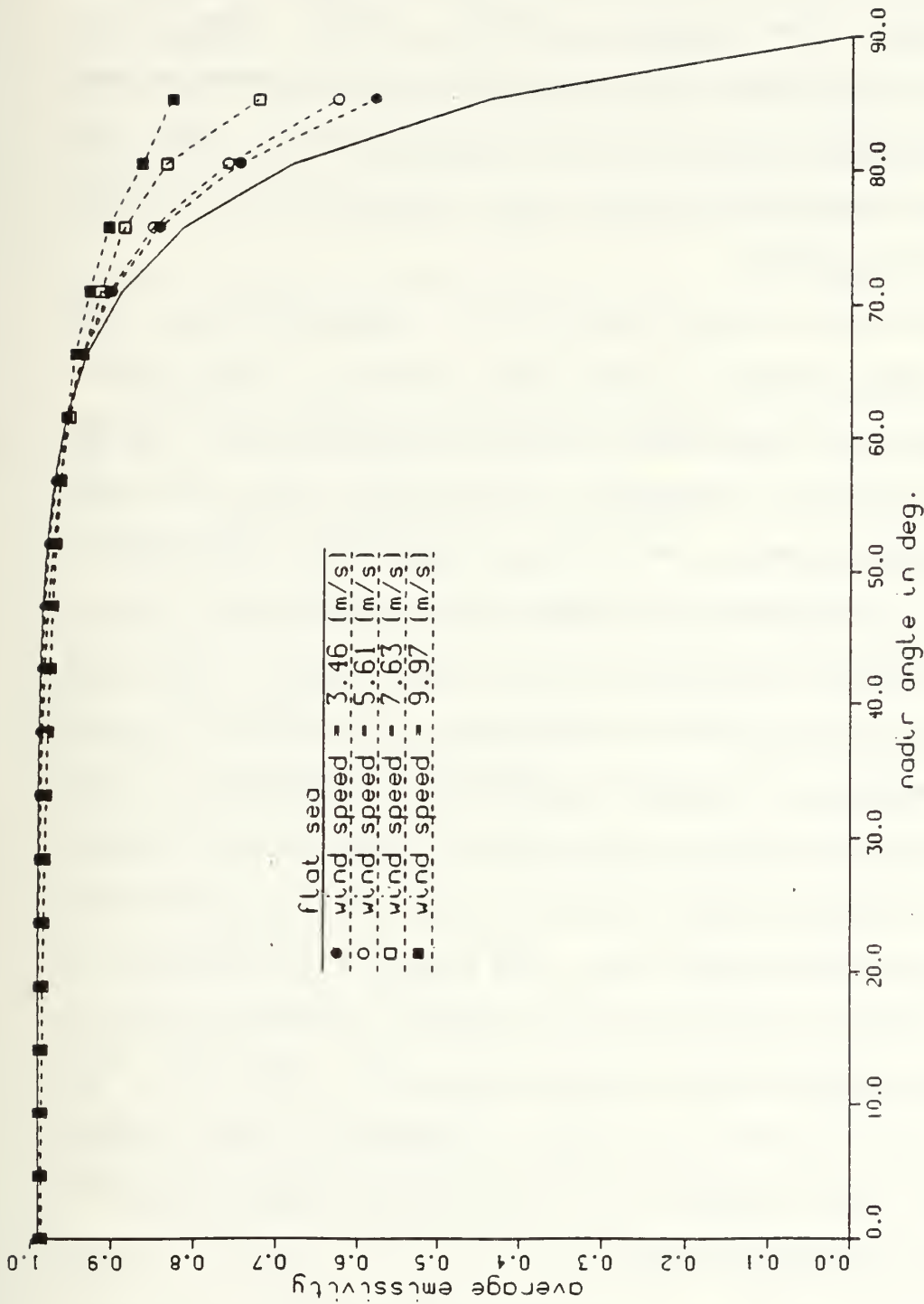


Figure 4.2 Sea surface emissivity vs. nadir angle from the Schwartz and Hon model (Ref. 21)

The Schwartz-Hon derived value of emissivity (ϵ_{SH}) has been validated for use at low grazing angles by LT Gregory Lawler, Naval Postgraduate School (1990) [Ref. 22]. His work involved comparisons of theoretical and measured sea and sky radiances which led to the conclusion that the Schwartz-Hon algorithm is sufficiently accurate for future use at near horizon angles.

The Schwartz-Hon algorithm as implemented in the computer code EMISS by Mr. John Cook of the Naval Oceanographic and Atmospheric Research Laboratory (now Naval Research Laboratory, Monterey, California) will be used throughout this paper. The value of emissivity computed by this code $\epsilon_{S\&H}$ represents the rough sea emissivity at 10 μm . This is sufficient for use in the 8-14 μm waveband, but since this thesis examines marine backgrounds in both the 2-5.6 and 8-14 μm wavebands, it becomes necessary to determine if this same value for emissivity can be used in the shorter waveband as well. Using the equations and indices of refraction presented by Friedman [Ref. 23], the difference between 10 μm and 4 μm emissivities for viewing angles between 80 and 90 degrees were computed to be less than 2.9%. Thus, for this work the Schwartz and Hon value of emissivity for viewing angles near the horizon will be used as the rough sea emissivity in both wavebands.

B. THE COX AND MUNK WAVE SLOPE DISTRIBUTION

Radiation emitted and reflected by the sea is affected by the presence of surface disturbances. It is necessary, therefore, to define statistically an ocean wave slope distribution for inclusion in sea radiance calculations. This function will serve to limit the percentage of wave slopes oriented toward a sensor which will in turn limit the radiance that sensor receives.

Through a series of observations of solar reflections from the sea, Cox and Munk derived a wave facet slope distribution to relate the probability of occurrence for a given wave slope to the local wind speed [Ref. 1]. From these observations they knew that at each individual glitter highlight there must have been a wave facet so inclined as to reflect the sun directly towards their detector. The slope of such a facet could be determined using Snell's Law by knowing the zenith angle of the sun and the elevation angle of the detector as well as the azimuth between them. Their efforts, then, made it possible to calculate the time-averaged radiance a sensor would receive from a rough sea by integrating the product of the calm sea's radiance and its wave slope distribution function over all possible wave slopes. [Ref. 8:p. 22]

The Cox and Munk empirically derived probability density function (PDF) for wave slopes has become accepted over several theoretically derived models, and remains the standard wave slope model used in most contemporary analyses. [Ref.

3:p. 13] Although their original analysis was performed in the visible region of the spectrum, their results can be easily extended into the IR. This is because IR wavelengths are short enough in comparison to ocean waves to sustain the geometric optics approach to measuring sun glitter in the IR. The results of Cox and Munk will be used hereafter in this thesis.

To define the Cox-Munk PDF a coordinate system is chosen as follows: let y designate the upwind axis, x the crosswind axis and z the vertical direction. Let β be the wave tilt as measured from horizontal and $m=\tan\beta$ be the slope of that wave, where α is its azimuth of ascent as measured from the positive y axis. With these definitions then

$$z_x=\delta z/\delta x=\tan\beta\sin\alpha, \quad z_y=\delta z/\delta y=\tan\beta\cos\alpha \quad (4.2)$$

are the crosswind and upwind components of a given wave's slope, respectively. Additionally, define ϕ to be the viewing elevation angle as measured from the horizontal. Let μ be the sun's zenith angle measured from vertical and offset from the y axis by angle ν . Figure 4.3 illustrates these angular relationships [Ref. 24:p. 7].

A wave facet's normal vector will not usually coincide with the vertical except in the case of perfectly calm seas. Since waves form and fall away rapidly, it is difficult to measure accurately their instantaneous slopes. If the viewing and sun angles are known, however, an intermediate local angle

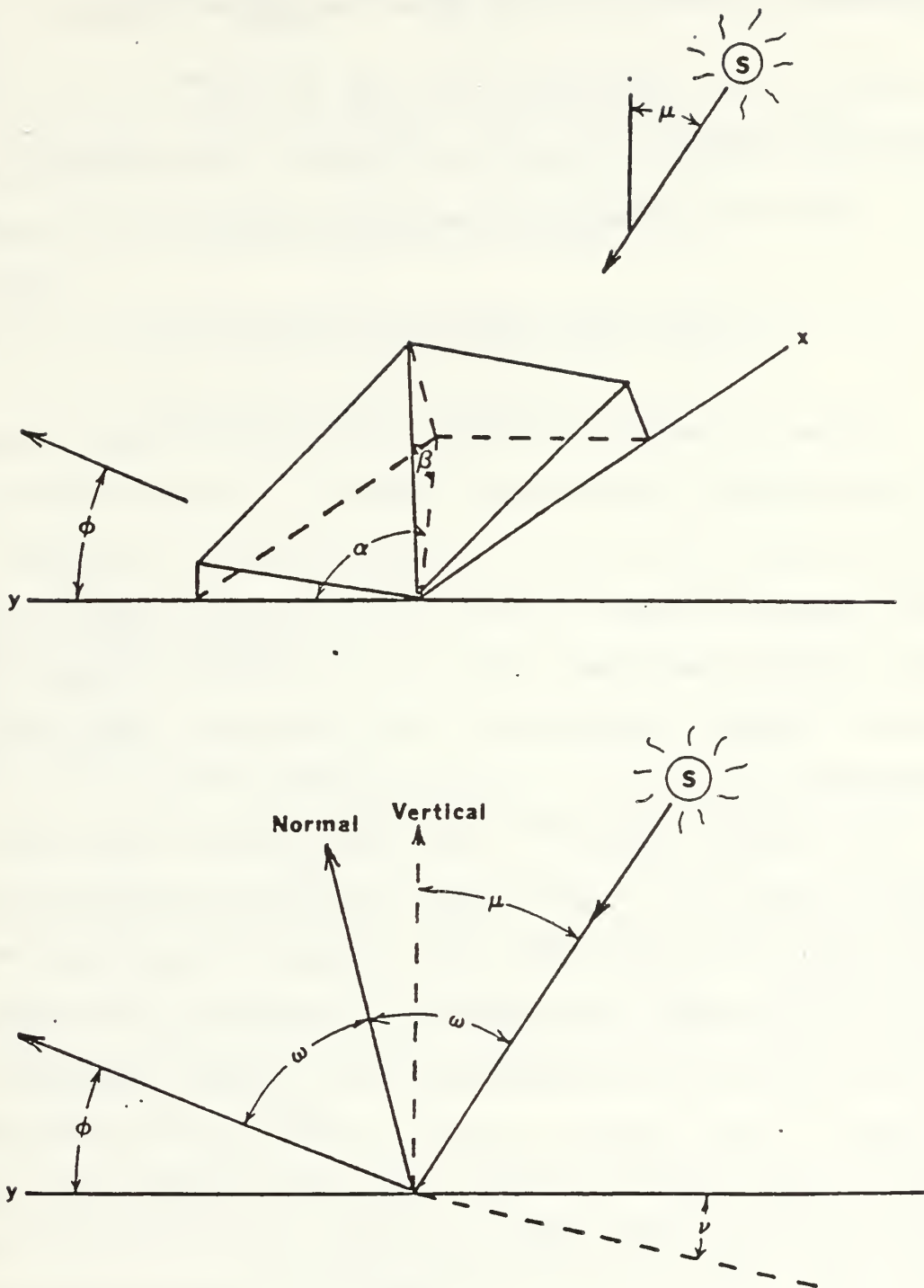


Figure 4.3 Solar Reflection Geometry (Ref. 24)

of incidence ω with respect to the wave's normal can be expressed in terms of the reflecting geometry by

$$\cos\omega = \sin\phi \cos\beta - \cos\phi \sin\beta \cos\alpha \quad (4.3)$$

where the angles α and β are defined by [Ref. 24:p. 2]

$$\cos\beta = (\cos\mu + \sin\phi) / (2\cos\omega) \quad (4.4)$$

$$\cos\alpha = (\cos\beta \sin\phi - \cos\omega) / (\sin\beta \cos\phi). \quad (4.5)$$

Since the overall horizontal sea surface slope is expected to be zero over large spatial areas, it follows that the mean values of z_x and z_y taken over many waves will be zero. The mean squared values, z_x^2 and z_y^2 , will not be zero, however. Cox and Munk designate these as σ_c^2 and σ_u^2 , (crosswind and upwind values, respectively) and interpret the rms slope components as σ_c and σ_u . [Ref. 25:p. 201]

The main result of Cox and Munk's work is the establishment of a wave slope distribution function $p(z_x, z_y)$ expressed as a Gram-Charlier PDF adapted to their data. It is defined such that the occurrence of slopes z_x, z_y is related to the probability of occurrence for a single highlight with slopes in the interval $z_x \pm \frac{1}{2}\delta z_x, z_y \pm \frac{1}{2}\delta z_y$ to occur within a small, horizontal unit area of sea surface $p(z_x, z_y)\delta z_x \delta z_y$. [Ref. 1:p. 841] The PDF is given by

$$p(z_x, z_y) = \frac{1}{2\pi\sigma_x\sigma_y} \exp\left[-\left(\frac{z_x^2}{\sigma_x^2} + \frac{z_y^2}{\sigma_y^2}\right)/2\right] [1 - C(W)] \quad (4.6)$$

where $C(W)$ is a series of Hermite polynomials which account for deviations from a standard two-dimensional Gaussian PDF resulting from naturally occurring, wind-induced skewness and peakedness:

$$C(W) = 1/2 C_{21} (\xi^2 - 1) \eta + 1/6 C_{03} (\eta^3 - 3\eta) - 1/24 C_{40} (\xi^4 - 6\xi^2 + 3) \quad (4.7)$$

$$- 1/4 C_{22} (\xi^2 - 1) (\eta^2 - 1) - 1/24 C_{04} (\eta^4 - 6\eta^2 + 3)$$

where

$$\begin{aligned} \xi &= z_x / \sigma_c \\ \eta &= z_y / \sigma_u \\ C_{21} &= 0.01 - 0.0086 \cdot W \\ C_{03} &= 0.04 - 0.033 \cdot W \\ C_{40} &= 0.40 \\ C_{22} &= 0.12 \\ C_{04} &= 0.23 \\ W &= \text{Wind speed (m/s)}. \end{aligned}$$

Equations 4.6 and 4.7 provide reasonable estimates of slopes within the limits defined by $|\xi| \leq 2.5$ and $|\eta| \leq 2.5$ (i.e., slope components up to two and one half times their rms value) and for wind speeds up to 14 m/s [Ref. 1:p. 849]. Figure 4.4 illustrates the distribution of wave tilts β for varying wind speeds [Ref. 26:p. 3180].

Cox and Munk's wave slope model permits an accurate computation of the time-averaged or mean spectral radiance for those sources which are affected by wave action: sea self-emission, sky reflections and direct solar glints. Its use is predicated on the following assertion: that the probability

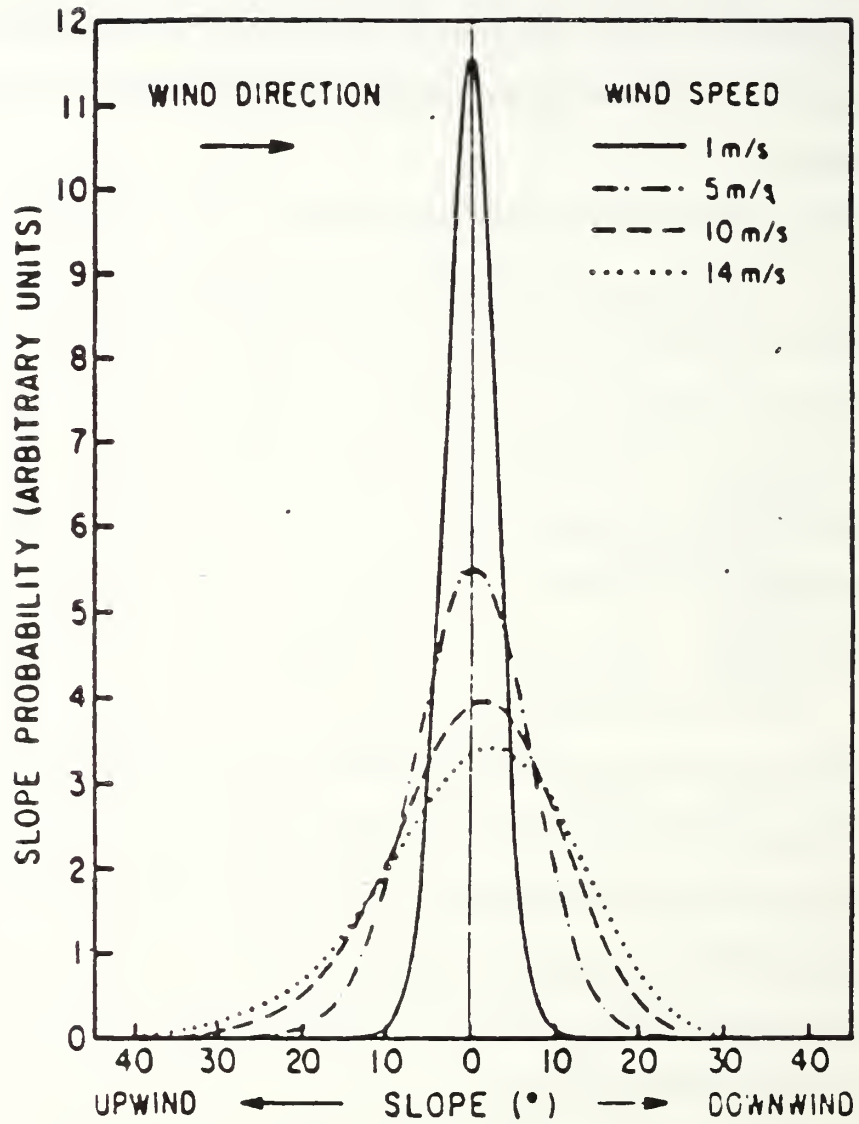


Figure 4.4

Facet tilt angle β distribution for a wind-roughened sea for various wind speeds from the Cox and Munk PDF (Ref. 26)

of radiance from a given direction hitting and reflecting off a facet is equal to the probability that the wave slope exists. Thus, in order to use the Cox and Munk PDF to improve the prediction of sea background radiance, a sensor must have either a large FOV or a long integration time in order to record many possible wave slope orientations. This is necessary since the radiance from an ensemble of facets is weighted by their probability of occurrence [Ref. 3:p. 2].

To compute mean radiance from direct solar reflections, Cox and Munk defined a reflectance probability P such that

$$P = p(z_x, z_y) \Delta_c \quad (4.9)$$

where Δ is the "tolerance ellipse" -- that area of a wave slope which reflects an object of small solid angular diameter and uniform radiance. Cox and Munk specified the area of this tolerance ellipse to be [Ref. 1:p. 842]

$$\Delta = \frac{1}{4} \pi \epsilon^2 \sec^3 \beta \sec \omega \quad (4.10)$$

where $\pi \epsilon^2$ is the solid angle of the sun disk in the sky such that $2\epsilon = 32'$. The reflecting unit area as projected into the line of sight is [Ref. 16:p. 647]

$$A = P \cos \omega \sec \beta \quad (4.11)$$

or, after rearranging

$$A = p(z_x, z_y) \pi \epsilon^2 \sec^4 \beta / 4. \quad (4.12)$$

Thus, if N_{sun} is the radiance of the sun at sea level, then the time-averaged radiance of the sea from direct solar reflections (glitter) according to Saunders [Ref. 16:p. 647] is

$$N_{\text{glitter}} = \frac{N_{\text{sun}} \pi \epsilon^2 p(z_x, z_y) \rho(\omega, \lambda)}{4 \cos^4 \beta \sin \phi}, \quad \left(\frac{\text{watt}}{\text{cm}^2 \cdot \text{sr}} \right) \quad (4.13)$$

where $1/\sin \phi$ accounts for the unit area normal to the direction of viewing when projected onto the horizontal.

C. WAVE SLOPE SHADOWING

For a given configuration of viewing angle and wave slope, a certain portion of waves will appear to be hidden behind other waves. Because Cox and Munk obtained their data from an aircraft at 2000 feet (corresponding to sun angles of $\mu < 55^\circ$), no accounting was made by them for the effects of radiance blocking from closely spaced waves. Hence, the results from the previous section are not immediately applicable to low altitude viewing without some form of correction for wave slope shadowing.

In Equation 4.13, as ϕ approaches zero (grazing view angle) the computed radiance approaches infinity. This clearly unrealistic case is understandable in light of Cox and Munk's experimental limitation of $\mu < 55^\circ$, which requires one to be airborne to produce the appropriate reflection geometry. For shipboard viewing positions, however, there is a need for

some form of correction term which extends Cox and Munk's work over all ranges of view and sun angles.

Slope shadowing accounts for the fact that at low observation angles, the slopes on the back sides of waves are hidden from view at low observation geometries. It is an important physical process to include in calculating the radiance from sea reflected sun glitter since it effectively reduces the surface area of the sea actually seen by an observer and, therefore, the radiance being reflected by it. Saunders [Ref. 16:p. 647] derived a shadowing correction factor $S^*(z_x, z_y) \leq 1$ which accounts for those facets which are hidden from the observer. S^* is defined as the fraction of the surface with slope components z_x and z_y that can be seen by an observer at a given angle ϕ . Thus for a shadowed wave where $z_y > \tan \phi$, $S^* = 0$. Otherwise $S^* = S^*(\phi)$, or

$$S^* = 2[1 + \text{erf}(v) + (v\sqrt{\pi})^{-1} \exp(-v^2)]^{-1} \quad (4.14)$$

where

$$v = \sigma^{-1} \tan \phi. \quad (4.15)$$

With the inclusion of Saunders' shadowing factor, Equation 4.13 becomes

$$N_{\text{glitter}} = \frac{N_{\text{sun}} \pi \epsilon^2 p(z_x, z_y) \rho(\omega, \lambda) S^*}{4 \cos^4 \beta \sin \phi}, \quad \left(\frac{\text{watt}}{\text{cm}^2 \cdot \text{sr}} \right) \quad (4.16)$$

thus ensuring that N_{glitter} remains finite for all values of ϕ while concurrently limiting the sun glitter radiance as a result of wave slope shadowing.

D. MEAN SQUARE WAVE SLOPE

Perhaps the most critical input to the Cox and Munk PDF is the sea surface mean square slope σ . This term relates the ambient wind speed to the average wave slope generated by that wind. Cox and Munk obtained values for their mean square slope components in the crosswind and up/downwind directions using linear regression methods and found that these two components as well as the overall mean square slope, $\sigma_c^2 + \sigma_u^2$ (independent of wind direction) varied linearly with wind speed W . Their expressions for mean square wave slope (valid for wind speeds up to 14 m/s) are defined as [Ref. 1:p. 847]

$$\sigma_c^2 = 0.003 + 1.92 \times 10^{-3} W, \quad r=0.956 \quad (4.17)$$

$$\sigma_u^2 = 0.000 + 3.16 \times 10^{-3} W, \quad r=0.945 \quad (4.18)$$

$$\sigma_c^2 + \sigma_u^2 = 0.003 + 5.12 \times 10^{-3}, \quad r=0.986. \quad (4.19)$$

In a reanalysis of Cox and Munk's mean square slope statistics, Wu [Ref. 27] found that σ^2 (equivalent to

$\sigma_c^2 + \sigma_u^2$) varied nonlinearly with wind speed. When Wu replotted Cox and Munk's measured wind speeds logarithmically against their mean square slope data, he found that an important trend had been overlooked: that mean square wave slopes appear to be segregated into separate regimes of low wind velocities ($<7\text{ m/s}$) and high wind velocities ($>7\text{ m/s}$). Wu's recomputed forms for mean square wave slopes (valid up to $W=15\text{ m/s}$) are

$$\sigma^2 = (1.2 + \ln W) \times 10^{-2}, \text{ for } W < 7 \text{ m/s} \quad (4.20)$$

$$\sigma^2 = (-1.45 + 0.85 \ln W) \times 10^{-1}, \text{ for } W > 7 \text{ m/s}. \quad (4.21)$$

Although Wu's results follow that of Cox and Munk by 18 years, his interpretations regarding the existence of two wind speed regimes have subsequently been endorsed by Cox [Ref. 28:p. 56]. Thus, the more precise expressions for σ^2 will be used in place of Cox and Munk's value of $\sigma_c^2 + \sigma_u^2$ in all equations used to compute glint radiance values within this thesis.

E. SOME OBSERVATIONAL ASPECTS OF SUN GLITTER

Over the course of several studies concentrating on various aspects of sun glitter, many valuable observations have been recorded. Those of importance to this thesis are detailed here to enhance the reader's understanding of sun glitter phenomena.

1. Temporal Nature of Sun Glints

As individual wave slopes form and fall away, the entire sea appears to be in seemingly continuous motion. As certain facets are formed whose geometries produce reflections toward an observer, that observer will record a momentary flash of light of some short duration. In attempting to overcome the problem faced by IR detectors from sun glitter, a *priori* knowledge of the duration of these individual glints would permit using some form of temporal discrimination processing. This would allow an IR sensing system to ignore short duration targets resulting from clutter (glints) while allowing that system to recognize and track long duration signals from real targets.

The available literature contains three reported measurements of the duration of individual glints, thus correlating the temporal persistence of sun glitter to the duration of individual wind generated wave peaks on the ocean. In a study of the 4.48 to 4.75 μm waveband, Fraedrich [Ref. 29:p. 395] reported a mean glint duration of 82 msec for wind speeds between 3.5 and 5.5 m/s. Schwering [Ref. 30:p. 34], looking at IR ocean clutter at wavelengths between 0.6 and 10 μm , found the mean glint duration to be in the range of 0.15 to 0.2 sec for wind speeds of 4.5 and 9.5 m/s. In a comprehensive IR background study performed by MIT Lincoln Laboratory [Ref. 31], a mean glint duration of 30 msec was reported from statistical

analyses of data in the 3-5 μm waveband (no wind speeds reported). Little correlation can be made between these studies without amplifying data such as solar positions and winds speeds except that IR sensors must be capable of framing at a rate on the order of 0.02 to 0.2 sec in order to distinguish between individual sun glints.

2. Sun Glitter Contribution to Ocean Contrast

Much can be learned about the nature of sun glitter by examining the response of ocean radiance to variations in parameters such as wind speed and wavelength. When distinct contrasts exist, the IR system designer can build spatial or spectral clutter discrimination algorithms into new systems which capitalize on these differences.

a. Wavelength Contrasts

In a theoretical investigation of sea and sky infrared spectral contrasts, Tropf [Ref. 20:p. 2] concluded that over the 3.5-5.0 μm waveband when the sea surface is capable of reflecting light from the sun's direction toward an observer, sun glitter will dominate all other nearby sources of radiance. Outside of a glinting region, the opposite is usually true because of the dominance of the sky's thermal emission at longer wavelengths.

Over a wider waveband (1-20 μm), Eisner, et. al [Ref. 17:p. 207] compared the radiances of a sun glint

corridor and a neighboring non-glinting region of the same near-ocean river. They reached the same conclusion as Tropf, namely that at short wavelengths ($<5\text{ }\mu\text{m}$) there was nearly 1000 times difference between glinting and non-glinting regions. At longer wavelengths, however, there was little difference by comparison because of the small amount of solar energy in wavelengths beyond $5\text{ }\mu\text{m}$.

b. Wind-Induced Contrasts

As wind speed increases, the mean wave slope also increases. Consequently, a larger fraction of the sea surface is seen at near-horizon viewing angles for high wind speed. A glitter pattern will then seem to widen with increasing wind speeds as the probability for the occurrence of waves having larger slopes also increases. Simultaneously, the probability of waves having small slopes is reduced, and the peak radiance within the now wider pattern is less than for a low wind (narrow pattern) condition (Gambling, [Ref. 32:p. 154]). Figure 4.5 illustrates the effects on glitter pattern width and maximum radiance the wind exerts. In an analysis of $8\text{-}12\text{ }\mu\text{m}$ infrared radiance contrasts near the horizon, Hughes [Ref. 13:p. 3] further supports Gambling's results by concluding that the mean radiances between the sea and sky tend to differ most during low wind-speed conditions.

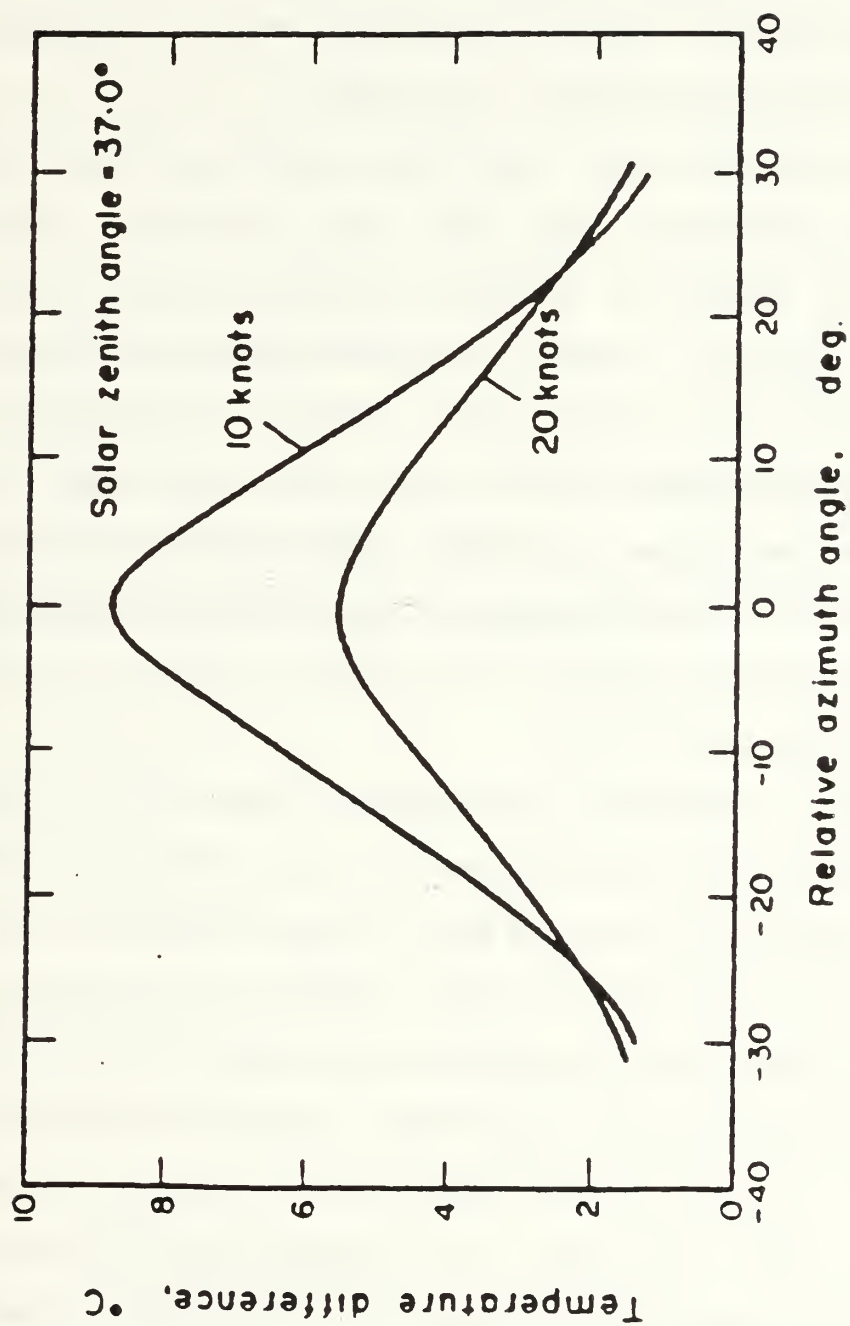


Figure 4.5 Computed glitter profiles for various wind speeds (Ref. 32)

F. GLITTER PATTERN WIDTH

One measure of the degree to which sun glitter interferes with an IR sensor is the fraction of azimuth it occupies within the sensor's FOV. As previously mentioned, both high solar elevations and higher wind speeds tend to increase the apparent width of sun glitter corridors.

In an analysis of infrared clutter within ocean backgrounds, Schwering [Ref. 30:p. 34] estimated the full width at half maximum of sunglint profiles in the 0.6-10 μm waveband to be $8.8 \pm 1^\circ$. Gambling's measurements of 2-5 μm sun glitter, [Ref. 32:p. 153] however, showed a half width of 35° for sun glitter at small solar zenith angles (sun high in the sky). These two values represent isolated cases and do not well illustrate the combinations of solar elevations and wind speeds which act to define the angular size of a glitter corridor on the sea surface.

To predict accurately the angular extent of a glitter corridor for a given wind speed and sun position, a model using the equations of Cox and Munk (or equivalent) is needed. One difficulty inherent in this process is defining the boundary between the glitter pattern and normal (non-glinting) sea surface emission/sky reflections. Since the Cox and Munk PDF is to a first order based on a standard Gaussian distribution [Ref. 1:p. 844], it is reasonable to define the width of a given sun glitter channel as that angular dimension occupied by $\pm 2\sigma$ of wave slopes. This is the statistical

equivalent of incorporating approximately 96% of a given sun glitter channel's wave slopes in the computation of its mean radiance.

In a recent memorandum, Tropf outlined a simplified computer code based on Cox and Munk to define the angular extent of glitter [Ref. 33]. Inputs to this code are surface wave slope (from Wu's wave slope statistics), seeker geolocation, date and time. This code adapts the geometrical equations set forth by Cox and Munk to compute the angle v , the seeker look angle relative to the sun, required to produce a glitter pattern over a range of possible sensor viewing angles. The angle v defines the half width of a sun glitter corridor for the conditions specified by the user. A printout of this code is contained in Appendix A.

V. DATA COLLECTION AND ANALYSIS

To begin the process of obtaining and analyzing sun glitter data, all the systems and support that would be required throughout this project had to be identified. Further, all necessary analytical tools had to be assembled in order to ensure that data collection requirements could be satisfied. This chapter describes the efforts involved in the collection of sun glitter data for this thesis, and the methodology adopted for analyzing it.

A. EXPERIMENT SETUP AND LOCATION

To obtain data, it was necessary to find a southwest facing location which would provide the best glitter channel presentation for Central California in the months of January and February during mid to late afternoon time frames. Any site chosen had to have ample space and electrical service in order to be effective for this purpose. The site chosen was the Point Sur Lighthouse in Big Sur, California.

Data was taken on three days, each of which provided a different meteorological condition. The first day, 30 January, 1992, was slightly overcast with broken, high clouds and a light breeze. The second day, 2 February, was clear and quite breezy with occasional wind gusts. 4 February, the final day, was warm and clear with only a light wind blowing.

These conditions satisfied the requirement that data be obtained under various weather states.

B. DATA COLLECTION EQUIPMENT

1. The AGA 780 Thermovision Thermal Imaging System

Sun glitter measurements were made using the Naval Postgraduate School Physics Department's AGA 780 Thermovision dual band thermal imaging system. Its normal short-wave channel bandpass is 3-5.6 μm , using a single indium antimonide (InSb) photovoltaic detector with a silicon optics, 7° by 7° lens. A broad band coating on the short-wave lens increases the relative response of the scanner such that its sensitivity is widened to 2-5.6 μm [Ref. 34:p. 3.4]. The long-wave system passes 8-14 μm energy using a single mercury cadmium telluride (HgCdTe) detector with a separate germanium optics, 7° by 7° lens. Both detectors are mounted against Dewar flasks containing liquid nitrogen which cool them to 77K. All sun glitter measurements were made at f/1.8 on both channels.

The AGA functions by using its lenses to direct thermal energy from a scene onto vertically mounted, 8 faceted prisms rotating at 180 rpm. Each of these prism's optical output is passed to a second, horizontally mounted 8 faceted prism rotating at 18000 rpm which passes the video signal through the aperture unit and finally onto the respective detector. The motors which drive these prisms are connected to the horizontal and vertical video triggering circuits in

such a way that the prisms "paint out" a frame consisting of four interlaced fields of 100 scanning lines each. The AGA scanner uses only 70 of these active display lines within each field. This produces a 280 line image, at a scan rate of 25 fields per second [Ref. 34:p. 3.1]. Raw images output from each channel are sent through an amplifier to a black and white video monitor and to the image processing software CATS, proprietary to the AGEMA corporation, on an INTEL 286-based desktop computer.

2. Thermal Imaging Techniques

The CATS software digitally displays and stores false color AGA 780 thermal images in either waveband and provides tools for either real time or stored video image analysis. It samples every second line sent to it by the AGA 780, producing an image which is 140 by 140 pixels at an image rate of 6.25 frames per second. This frame rate was deemed too slow to obtain any data on the temporal nature of sun glitter, but was sufficient to collect radiometric data which could be later manipulated into time-averaged sun glitter radiance values.

Each channel's black and white monitor contains controls for adjusting the system's thermal level and thermal range to be compatible with the scene under examination. These parameters are measured in arbitrary isothermal units which are linearly proportional to the intensity of radiation falling on the detector, but nonlinear with respect to

apparent temperature. The "Thermal Level" control adjusts the DC level of the AC video signal, while "Thermal Range" limits the dynamic range of the signal corresponding to a range of temperatures centered about a median temperature established by the thermal level adjustment.

Prior to use in the field, the AGA was calibrated against a laboratory blackbody source over a wide range of temperatures in order to obtain the proper relationship between isothermal units I and source temperature T. This calibration provided the constants A,B and C which fit the following expression (valid only for a 7° lens at f/1.8) [Ref. 34:p. 10.6]:

$$I = \frac{A}{C \exp(B/T) - 1} - \text{Offset}, \quad (\text{isothermal units}) \quad (5.1)$$

where

T = the apparent temperature of a given pixel in Kelvin assuming no intervening atmospheric effects

2-5.6 μm (shortwave) Calibration Constants are

A = 183453 B = 2814 C = 1 Offset = -12

8-14 μm (longwave) Calibration Constants are

A = 9835 B = 1565 C = 1 Offset = +1.5

Figure 5.1 illustrates the relationships between thermal level, thermal range and temperature for a sample measurement. [Ref. 34:p. 10.1]

Following a satisfactory calibration, the AGA was used directly to obtain thermal images without the need for separate temperature reference sources within its FOV. The system subsequently provided source temperature values by

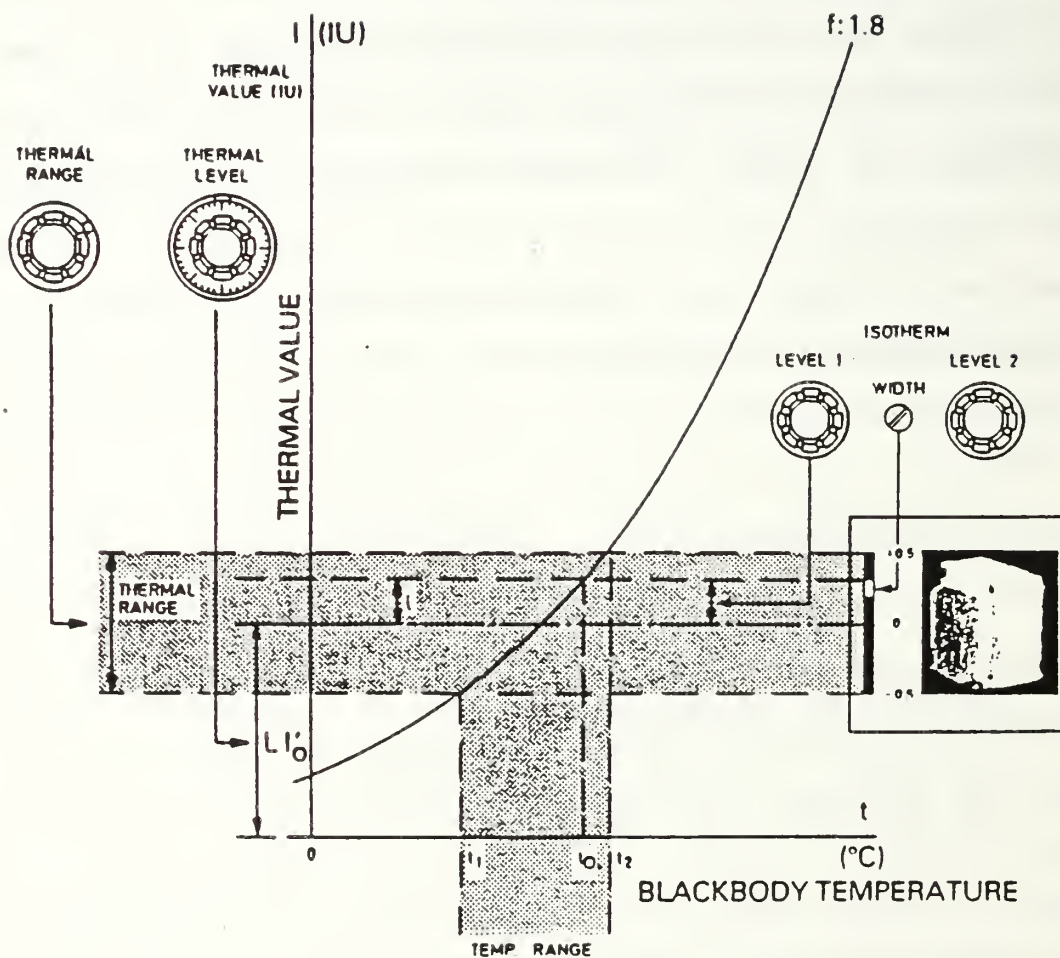


Figure 5.1

AGA 780 measurements using the thermal level and thermal range adjustments (Ref. 34)

assuming that any object in its FOV was a perfect blackbody radiator and that no external factors influenced the measurement (i.e., atmospheric). To then obtain true pixel temperatures, the CATS system mathematically compensated its thermal measurements for atmospheric transmissivity, path radiance and source emissivity effects by taking into account user input values of target emissivity, ambient atmospheric temperature and path length using the following relation

$$P_1 = \tau \epsilon_o P_o + \tau (1 - \epsilon_o) P_s + (1 - \tau) P_{atm} \quad (\text{Watts}) \quad (5.2)$$

where

- P_1 = total radiant power received by the system
- τ = atmospheric attenuation factor, dependent on range
- ϵ_o = object emissivity
- P_s = radiant power from a target's surroundings as a blackbody
- P_{atm} = radiant power from the atmosphere as a blackbody
- P_o = radiant power from a target as a blackbody
- $\epsilon_s = \epsilon_{atm} = 1.$

The first term on the right side of Equation 5.2 represents the received radiant power emitted from an object (target). The second term is the received radiant power from that object's surroundings as reflected by the object. The third term represents the received radiant power emitted by the atmosphere intervening between an object and the imager.

Because the AGA's thermal values are linearly related to the radiant power received by the system, Equation 5.2 can instead be expressed directly in isothermal units as [Ref. 34:p. 10.5]

(5.3)

$$I_1 = \tau \epsilon_0 I_0 + \tau (1 - \epsilon_0) I_s + (1 - \tau) I_{atm} \quad (\text{isothermal units})$$

where the subscripted I terms represent the thermal values of corresponding radiation sources as defined in Equation (5.2). I_0 (as computed by solving Equation (5.3)) and the calibration constants A, B and C can then be used in Equation 5.1 to compute the apparent temperature for each specified pixel.

The accuracy of any calculation used to compensate a specified pixel's temperature for emissivity and atmospheric effects is dependent upon how τ and ϵ are formulated. The CATS program simply computes a general value for τ and accepts a single value for ϵ over the entire 7° by 7° area covered by each image. For greater precision, it would be desirable to use the Schwartz and Hon value of ϵ and the LOWTRAN value of τ (which vary over changing elevation angles) to produce the most accurate results, but this is not permitted within the CATS software.

To improve on CATS' built-in compensations for target emissivity and atmospheric effects, an external pixel-by-pixel computation using the more accurate values of $\epsilon_{S\&H}$ and $\tau_{LOWTRAN}$ will be used in this thesis. This should provide more reliable results since an image of sun glitter is generally large enough that these parameters will vary over the vertical length scale of a single image.

C. SUN GLITTER DATA COLLECTION

Preliminary analysis of sun glitter characteristics preparatory to data collection revealed that a typical glitter corridor would be larger than the AGA's 7° by 7° lens size. This implied that multiple subimages of a pattern would be required to capture an entire glitter pattern's image in a patchwork fashion. The AGA, therefore, had to be accurately pointed in azimuth and elevation during data collection in order to prevent overlap between images while also ensuring that no part of any pattern was excluded from the measurements. Two protractors with pointers were mounted on the AGA tripod to enable accurate angular directivity during imaging. Subsequent calibration of this pointing system revealed accuracies of 0.25° in elevation and 0.31° in azimuth (which equate to 5 and 6 pixels, respectively with each pixel measuring $.05^\circ$ by $.05^\circ$).

The AGA frame rate, although too slow to obtain any data on the temporal nature of sun glitter, was not slow enough to allow any single image to represent the mean (time-averaged) sun glitter radiance as defined by Cox and Munk. In order to measure mean sun glitter radiances using the AGA 780, four separate images were recorded of each subscene in each waveband. Subsequent pixel-by-pixel radiance averaging would then yield the time-averaged radiances for each scene. Pursuing data analysis in this way allowed for follow-on comparison of this work's data to any output from theoretical

models based on the Cox and Munk PDF. A representative sun glitter thermal image from the 2/4/92 short-wave data is presented in Figure 5.2 with a photograph of the same pattern reproduced in Figure 5.3.

D. METEOROLOGICAL DATA COLLECTION

The requirements to collect meteorological data in support of this experiment were driven by the intent to employ LOWTRAN to compute values for atmospheric transmissivity τ for use in compensating sun glitter data for atmospheric effects. Three sources of real time weather information were recorded during each day's collection efforts.

First, each day's vertical atmospheric profile was recorded via radiosonde launches from the Point Sur lighthouse. These recordings were made approximately one half hour prior to any sun glitter data collection, and therefore represented excellent information as to the nature of the atmosphere as it existed during data collection.

Since the radiosonde launches occurred atop the 361' high grounds of the lighthouse, it was also necessary to record the meteorological conditions at the sea surface. This was accomplished by establishing communications with the Monterey Bay Aquarium weather buoy via computer modem. This buoy, although located 20 miles away, was the best source of sea surface weather information available. It provided data on open ocean surface winds and sea surface temperatures that

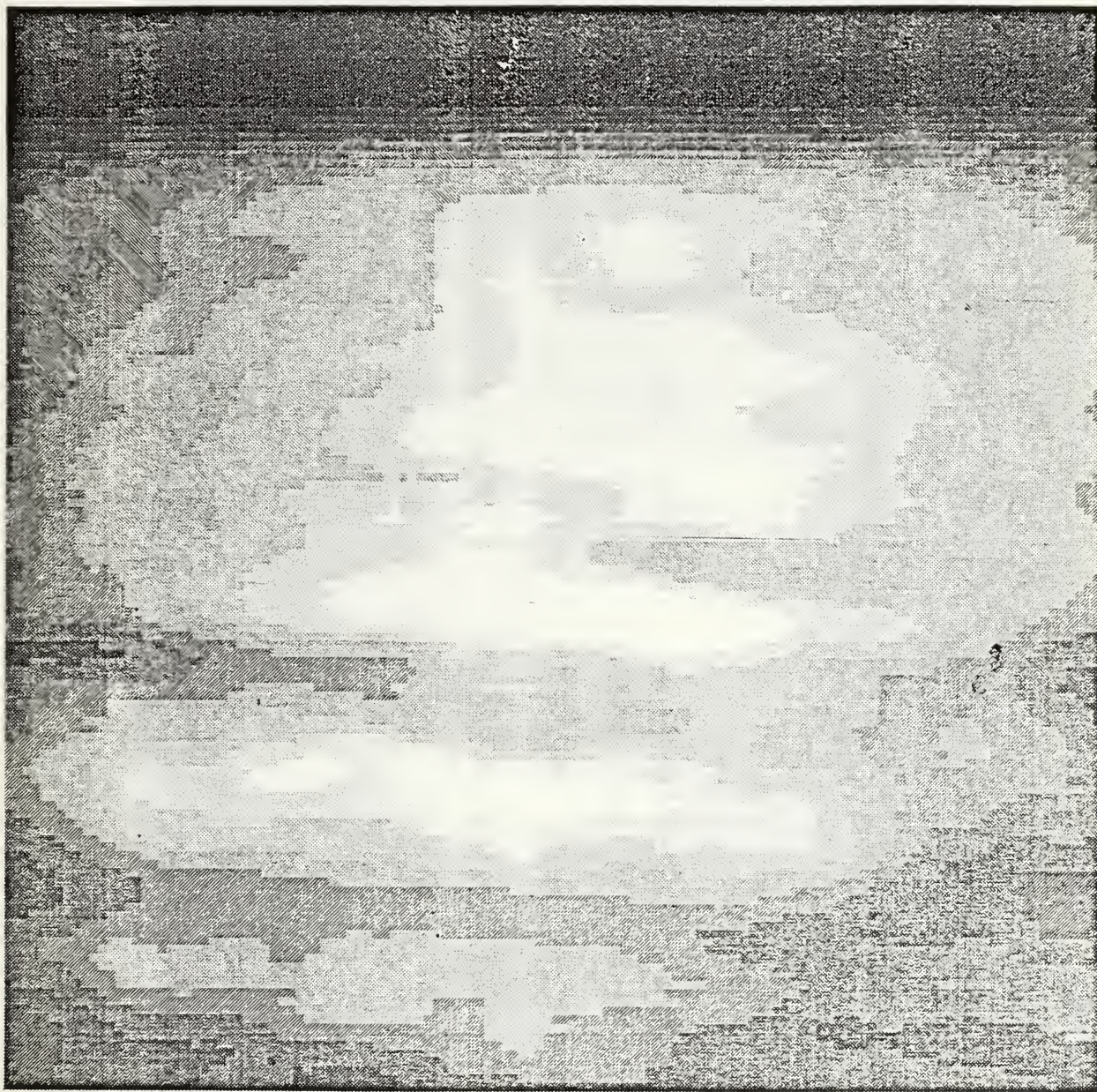


Figure 5.2 Sun glitter corridor imaged by the AGA 780 Thermovision thermal imager in the 2-5.6 μm waveband

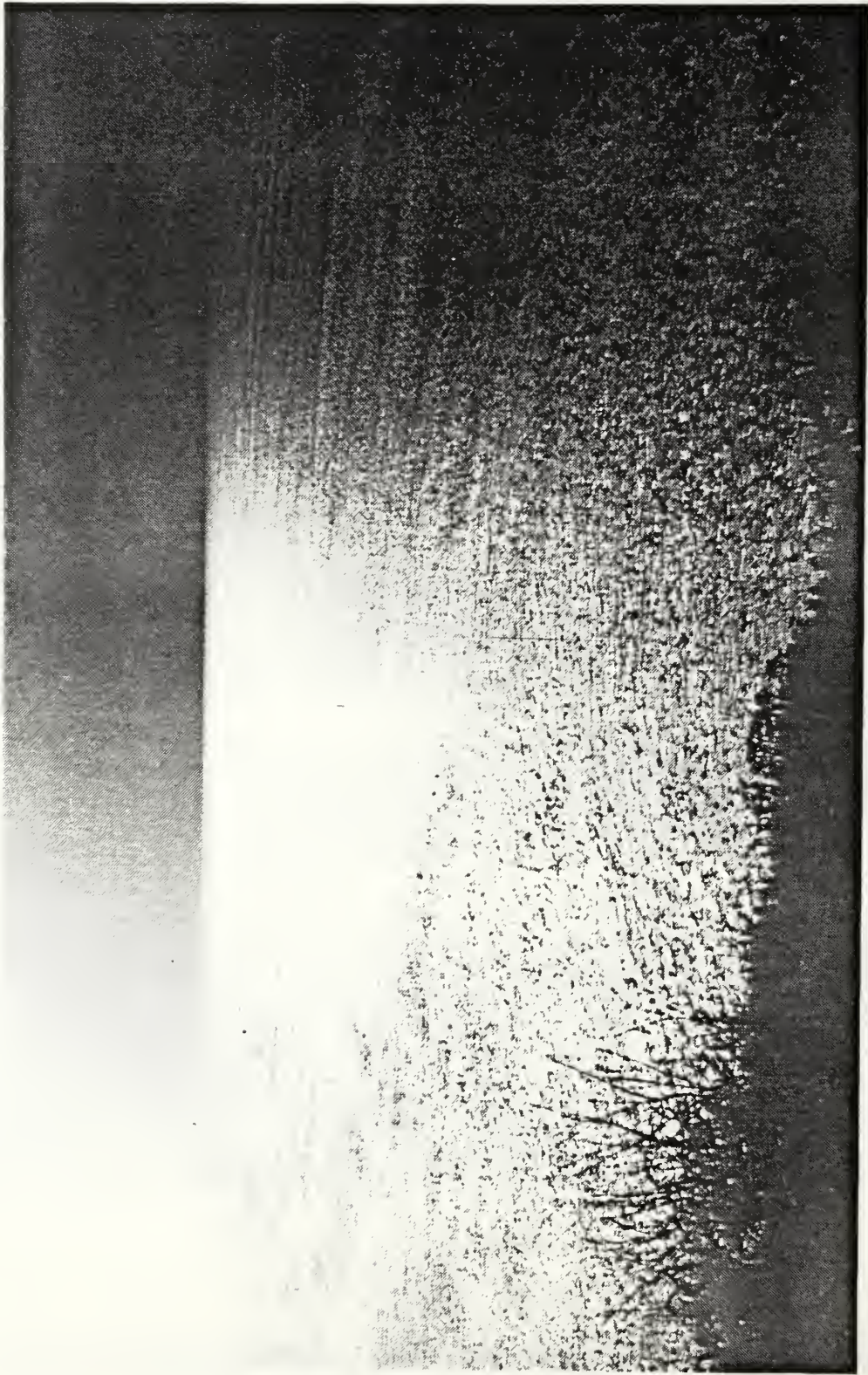


Figure 5.3 Photograph of sun glitter corridor corresponding to the thermal image of Figure 5.2

accurately represented the surface conditions at Point Sur. Buoy wind speed measurements were verified by comparison to a SOLOMAT portable weather station at the lighthouse, while a calibrated radiometric thermometer was used to confirm the buoy's sea surface temperature measurements. On each day the variations between sites were slight enough to permit using the buoy's data, despite its distance from the experiment's location. Overall vertical profiles, then, were constructed using sea surface values from the buoy (zero meters), plus ground measurements at the base of the lighthouse (110 meters), followed by layered data from the radiosonde (up to approximately 4 km). These composite vertical profiles are contained in Tables 5.1, 5.2 and 5.3 for each of the three day's measurements. 24-hour averaged wind speeds as required for input into LOWTRAN were obtained by retrieving buoy wind speed data for the 24 hour period that preceded each day's data collection as archived by the Monterey Bay Aquarium Research Institute (see Table 5.5).

E. DATA ANALYSIS

After all of the sun glitter images were collected, it was necessary to extract for analysis the raw, uncompensated, equivalent blackbody temperature data (in °C) stored in standard PC-DOS files (created using the CATS software). This was accomplished manually using the mouse-assisted computer program AGACAT, written by Dr. E. Milne of the Naval

TABLE 5.1
RADIOSONDE DATA--PT. SUR LIGHTHOUSE

30 January, 1992

Launch time 2339 GMT

<u>Altitude (km)</u>	<u>Pressure (mb)</u>	<u>Temp (C)</u>	<u>Relative Humidity</u>
.000	1014.6	16.8	72
.110	1004.0	17.9	44
.147	1000.5	16.5	45
.181	996.6	15.2	46
.213	992.9	15.0	47
.245	989.2	14.6	50
.280	985.3	14.5	52
.312	981.7	15.6	53
.342	978.3	16.3	43
.374	974.7	17.0	33
.404	971.3	17.4	27
.433	968.2	17.5	26
.465	964.7	17.4	27
.493	961.6	17.2	27
.525	958.0	17.0	27
.555	954.7	17.6	26
.588	951.2	18.2	22
.620	947.7	18.5	22
.655	943.9	18.4	23
.702	938.8	17.9	24
.750	933.7	17.5	25
.795	928.9	17.2	23
.836	924.6	17.1	22
.879	920.0	16.8	21
.916	916.2	16.7	21
1.068	900.3	16.6	15
1.231	883.5	15.6	13
1.365	870.1	14.7	16
1.524	854.1	13.4	17
1.681	838.7	12.4	16
1.802	826.9	11.8	19
2.111	797.4	9.6	17
4.066	630.1	-2.6	5

TABLE 5.2

RADIOSONDE DATA--PT. SUR LIGHTHOUSE

2 February, 1992

Launch time 2255 GMT

<u>Altitude (km)</u>	<u>Pressure (mb)</u>	<u>Temp (C)</u>	<u>Relative Humidity</u>
.000	1015.3	13.6	70
.110	1003.0	14.7	79
.139	999.7	12.3	41
.165	996.5	12.4	44
.188	993.8	13.0	47
.221	989.9	13.9	51
.286	984.3	14.7	57
.324	977.8	15.1	60
.372	972.2	15.5	65
.418	966.9	16.0	59
.455	962.2	16.2	57
.505	957.0	15.9	57
.549	952.0	15.5	57
.591	947.3	15.3	57
.632	942.6	14.9	57
.675	937.8	14.5	57
.713	933.6	14.1	57
.756	928.8	13.8	58
.801	923.7	13.4	59
.855	917.8	13.2	56
.909	911.9	13.4	52
.958	906.5	13.5	47
1.005	901.4	13.3	45
1.046	896.9	13.1	45
1.086	892.7	12.6	45
1.129	888.1	12.3	45
1.161	884.6	12.0	45
1.204	880.0	11.7	45
1.372	862.3	10.3	46
1.534	845.4	8.9	46
1.684	830.1	7.5	46
1.960	802.2	5.3	46
4.035	616.5	-7.2	54

TABLE 5.3
 RADIOSONDE DATA--PT. SUR LIGHTHOUSE
 4 February, 1992
 Launch time 2300 GMT

<u>Altitude (km)</u>	<u>Pressure (mb)</u>	<u>Temp (C)</u>	<u>Relative Humidity</u>
.000	1009.8	14.7	59
.110	1000.0	20.3	45
.121	998.7	16.1	39
.142	996.3	15.7	25
.188	991.0	14.8	24
.244	984.5	13.7	21
.298	978.2	12.7	18
.344	973.0	12.1	17
.373	969.7	12.0	17
.404	966.1	11.7	17
.435	962.6	11.5	17
.468	958.8	11.3	17
.501	955.1	11.0	17
.534	951.4	10.7	17
.566	947.7	10.5	17
.601	943.7	10.1	18
.636	939.8	9.8	18
.669	936.2	9.5	18
.700	932.7	9.2	18
.735	928.9	8.9	19
.765	925.5	8.6	19
.800	921.7	8.3	19
.833	918.1	8.0	20
.861	914.9	7.7	20
.892	911.6	7.4	20
.918	908.7	7.1	20
1.077	891.6	5.9	22
1.206	877.7	5.3	21
1.360	861.6	3.9	22
1.530	843.9	2.6	23
1.666	830.0	1.6	23
1.972	799.4	0.0	9
4.011	618.5	-13.8	19

Postgraduate School. AGACAT is a Microsoft FORTRAN routine which reads in CATS generated image data files and furnishes the user with more precise image analysis tools than those provided by the CATS program itself. It provides an enhanced false color display of any image captured using CATS, and thus makes the data from the AGA thermal imager compatible and accessible to any microcomputer.

Due to differing sun angles and wind speeds, each day's data showed a different sun glitter corridor width. The analysis process, therefore, consisted of isolating selected horizontal rows of pixels as measured below the horizon and analyzing these over each image taken during a given day. Specifically, the data from pixel rows at the 1°, 4°, 7° and 10° depression angles below the horizon were recorded from across the width of each scene. By extracting data in this manner, values from one scene could be compared with those from another scene taken on the same day, assuming that meteorological conditions and sun angles remained constant during the course of any single day's data collection effort. Since collection periods for data in either waveband were restricted to time periods on the order of approximately 0.75 hours, this assumption is valid. The amount of depression angle the AGA could achieve, approximately 13° below the horizon, was limited by interference from rocks and shore breakers at greater depression angles.

Instead of sensing a target from within an ocean background, this work involved looking at the sea alone. As a result, the sea surface source radiance I_0 represents the sum of sea self-emission, reflected sky radiance and direct solar reflections. By defining source radiance in this way, it was not necessary to account for the reflected radiance term $(1-\epsilon_0)I_s$ as detailed in Equation 5.3. The resulting equation (in isothermal units) used to compensate for source emissivity and atmospheric effects (transmissivity and path radiance) within this thesis, then, is

$$I_1 = \tau_{\text{LOWTRAN}}(\theta_{\text{view}}) \epsilon_{\text{SH}}(\theta_{\text{view}}) I_0 + (1 - \tau_{\text{LOWTRAN}}(\theta_{\text{view}})) I_{\text{atm}} \quad (5.4)$$

where I_{atm} is the blackbody thermal level (corresponding to T_{atm} measured during each day's data collection) as computed by Equation 5.1, $\epsilon_{\text{S\&H}}$ is from the Schwartz and Hon model (dependent upon view angle) and τ_{LOWTRAN} is the transmissivity as computed by LOWTRAN (dependent on view angle). I_1 , the apparent uncompensated pixel thermal level as output from the AGA 780, was obtained by setting $\epsilon=1$ and $\tau=1$ within the CATS software. This forced the system to readout directly as $T_1=T_0$ (in °C) after computation by Equation (5.3), the CATS internal algorithm. At this point the AGA 780's output represented the equivalent blackbody temperature corresponding to the energy falling on its detector from all sources within the FOV of the measured pixel. This value, when converted to isothermal units using Equation 5.1, was equal to I_1 for use in Equation

5.4. This procedure effectively overrode the internal algorithm within CATS (Equation (5.3)) which failed to account for any angular variations in ϵ and τ in its corrections for atmospheric effects and source emissivity.

Equation 5.4 was implemented as the MATLAB routine AGACOMP.M, written specifically for this analysis to accept inputs in the form of uncorrected source temperatures from the AGA. It provides output in the form of source radiance I_0 ($\text{Watts/cm}^2 \cdot \text{sr}^{-1}$) corrected for atmospheric transmissivity, path radiance and source emissivity variations with view angle. AGACOMP.M performs the following steps:

1. Accepts as its entering argument apparent temperatures as measured by the AGA 780 (extracted using Milne's AGACAT FORTRAN program) in either vector or single value format, with each individual temperature value representing the apparent blackbody temperature of a specified pixel
2. Reminds the user of which scanner constants (short wave or long wave) are currently being used to convert apparent temperatures to thermal values; additionally this indicates which waveband will be integrated over when converting from compensated temperature to source radiance
3. Queries the user for the atmospheric temperature, the path transmissivity (from LOWTRAN) and ocean surface emissivity (from the Schwartz and Hon algorithm) to be used in compensating for atmospheric effects and emissivity variations at a given horizontal position below the horizon
4. Computes I_{atm} from T_{atm} using Equation (5.1)
5. Computes I_1 from the temperature entered as the entering argument to the program using Equation (5.1)
6. Solves Equation (5.4) for I_0 , the equivalent blackbody thermal level of a specified pixel, or

$$I_0 = \frac{I_1 - (1 - \tau_{\text{LOWTRAN}}) I_{\text{atm}}}{(\epsilon_{\text{SH}} \cdot \tau_{\text{LOWTRAN}})} \quad (5.5)$$

7. Converts I_0 back to equivalent blackbody temperature (now compensated for atmospheric effects and source emissivity) using the inverse of Equation (5.1)

$$T_0 = \frac{B}{\ln((A/C(I_0 + \text{offset})) + 1)} \quad (5.6)$$

8. Computes Planck's integral (Equation (2.2)) coded as the MATLAB routine IRTEMP.M) over the appropriate waveband using the compensated pixel temperature computed above; this yields that pixel's source radiance in Watts/cm²·sr.

In order to implement Planck's integral (IRTEMP.M) within MATLAB, two of that program's internal functions, QUAD.M and QUADSTP.M, had to be modified to accept an additional temperature parameter. These functions were retitled as QUAD2PAR.M and QUADSTP2.M, respectively. Printouts of functions AGACOMP.M and IRTEMP.M are reproduced in Appendix B.

1. LOWTRAN Atmospheric Prediction Code

During data analysis, a more accurate means was needed to compute the net transmission of IR radiation over atmospheric paths. The model chosen for this was the LOWTRAN 6 computer code as modified by F. Wollenweber, of the German Military Geophysical Office [Ref. 35].

Since infrared systems are designed to operate through naturally occurring atmospheric windows, it is necessary to be able to predict the overall transmittance of the atmosphere as a function of wavelength and weather conditions. This prediction becomes a complex problem of computer modeling. LOWTRAN, a computer code developed by the Air Force Geophysics Laboratory, has become the standard for DOD atmospheric transmittance and radiance modelling. It use allows for compensation of atmospheric effects within IR systems.

LOWTRAN is a quick, efficient, and moderately accurate computer routine based on a single-parameter band model of molecular absorptions and emissions. It is a FORTRAN computer code designed to calculate atmospheric transmittance and radiance, averaged over 20 inverse centimeter intervals in steps of 5 inverse centimeters over a user specified path, in the 0.25 to 28.5 μm spectral range [Ref. 36:p. 2]. The code includes effects resulting from atmospheric refraction and curvature of the earth. Atmospheric parameters used by the LOWTRAN code are input as stacks of up to 33 layers, from 0 to 100 km altitude. Meteorological parameters such as barometric pressure, temperature, and humidity are user defined for each layer. As the optical path passes through each layer of a specific atmosphere during computation, the program sums all of the extinction elements (absorption and scattering) over each

layer and computes an overall transmissivity for the specified bandwidth.

Obviously, LOWTRAN is quite computationally intensive. The accuracy of its output is dependent upon the precision with which a given atmosphere is defined to the program. There have been extensive efforts to validate the LOWTRAN code for naval use. Among these is that of F. Wollenweber who evaluated the accuracy of LOWTRAN for near horizon transmittance calculations and has amended the algorithms within the source code to enhance its accuracy [Ref. 35]. Wollenweber performed comparisons between path radiances measured by a thermal imaging system (by converting apparent blackbody temperatures to atmospheric radiances using Planck's Law) and those predicted by LOWTRAN. He found generally good agreement between the two except in a narrow region around the horizon where LOWTRAN showed a radiance dip of approximately 30 percent relative to the measured values [Ref. 35:p. 2]. Wollenweber found this dip present in all aerosol models available to LOWTRAN. He proposed a solution to this disparity in a computer code modification which added artificial sublayers of atmosphere between the user defined layers. For a nearly horizontal path, Wollenweber determined that any increase in path radiance (due to long path lengths) was being offset by a coincident reduction in transmittance (also due to long path lengths through the same aerosol environment) [Ref. 35:p. 4]. By introducing artificial

sublayering within the predefined layers, Wollenweber found that the same radiance originated out of several thinner layers as from the one large one they replaced. Along the same path, however, the transmittance decreased fractionally less for each sublayer, resulting in a higher overall transmissivity over the same path. The net effect of Wollenweber's algorithms which artificially add sublayers to LOWTRAN's predictive routines is illustrated in Figure 5.4. This shows that the anomalous dip in path radiance at the horizon (as predicted by unmodified versions of LOWTRAN 6) is effectively removed when compared to actual path radiances as measured by a thermal imager [Ref. 35:p. 5].

For ease of use, the Wollenweber modified version of the software package PC-TRAN (a desktop version of LOWTRAN 6 by the ONTAR Corporation [Ref. 36]) was used in place of LOWTRAN for the calculations in this thesis. Atmospheric layer data was supplied to PC-TRAN from the radiosondes launched during data collection. Since most of this work's data consisted of images taken over low altitude nearly horizontal paths, only those layers below 4 km altitude were used as input into PC-TRAN. This was intended to improve the precision of that program's transmittance computations for low angle viewing.

Aerosol behavior within PC-TRAN was accounted for by specifying the Navy Maritime Model from the six available aerosol models to define the size, concentration and origin of

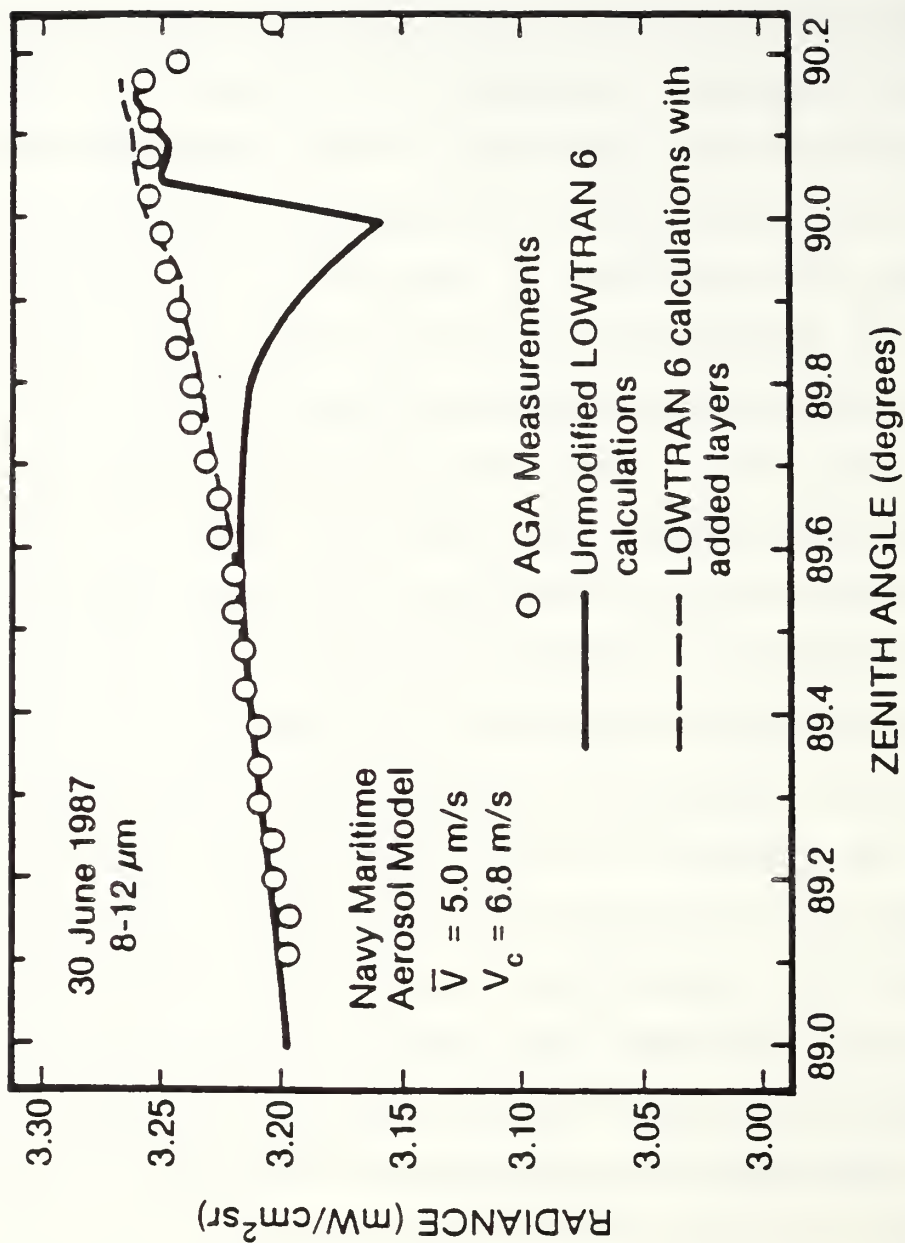


Figure 5.4

Comparison of measured sky radiances and those calculated by LOWTRAN 6 with and without additive layering versus zenith angle (Ref. 35)

particles found within the particular environment. Additionally, an ocean-influenced aerosol concentration was specified to PC-TRAN by selecting an air mass character value of 3 (from a scale where 1=open ocean and 10=strong continental influence). This value was chosen because of the seemingly continuous onshore winds experienced in the vicinity of the Point Sur lighthouse.

2. Correlating the Physical Horizon with the Computer Display

Because of viewing geometry considerations and path refractivity effects, a computation of the thermal imager's angle to the horizon was required so that all measurements taken on a given day could be made with respect to the same horizon as captured in the images. To be as accurate as possible, the AGA camera itself was levelled prior to any measurements. The pointing system added to the AGA for this experiment was too crude to measure the horizon angle accurately, so it was decided to use LOWTRAN to calculate it.

The horizon on the computer image display was identified by noting the vertical location of the thermal discontinuity established by the sea-air interface. The approach to correlate this position with the computed horizon angle was to execute LOWTRAN iteratively over several viewing zenith angles in order to find the last one which intersected

the earth at the horizon. This was accomplished for each day by furnishing vertical profile and height of eye data for input into LOWTRAN and executing it in the transmittance mode. Height of eye was calculated by adding the height of the lighthouse building above sea level, the height of the camera above ground, and the height of the tide for that day (see Table 5.4). Angles which did not intersect the earth resulted in an error message from LOWTRAN pertaining to improper geometry. Once the proper angle was found by trial and error, all other elevation measurements within the images for that same day could be correlated to this position, knowing that any single image was 7° or 140 pixels high in elevation (corresponding to 0.05° per pixel). The horizon angles computed using this method are contained in Table 5.4.

F. SYSTEMATIC SUMMARY OF SUN GLITTER DATA ANALYSIS

The ultimate aim of this thesis is to be able to incorporate sun glitter predictive algorithms into IR seeker based weapons in order to minimize their vulnerabilities to sun glint clutter. To that end, this work produces data pertaining to the statistical and physical nature of sun glitter such that follow-on research on modelling and discrimination routines can proceed.

For each day's data in each waveband (six separate sets), a standard method of data analysis was adopted. Application of this routine yielded three prime outputs, specifically:

- A plot of the spatial source radiance distribution vs. azimuth
- The angular width of each corridor
- A histogram of the source radiance distribution

The first step was to calculate the inputs to the MATLAB routine AGACOMP.M which compensated for atmospheric effects and surface emissivity variations. Using the radiosonde data from Tables 5.1, 5.2 and 5.3, the horizon angle θ_h was then computed for each day (applicable to both wavebands). With this angle, then, the transmissivities for other angles below the horizon (specifically the 1°, 4°, 7° and 10° angles) could be computed by LOWTRAN using the same method. Table 5.4 presents the transmissivities calculated for each day at specified angles below the horizon. The program EMISS was then used to compute the Schwartz and Hon value of surface emissivity as a function of wind speed and depression angle, θ_{view} . The results of these computations are presented in Table 5.5.

The next step was to extract the horizontally displaced raw data in the form of apparent blackbody temperatures from the AGA thermal images using Milne's mouse assisted FORTRAN routine, AGACAT. Each sun glitter pattern was comprised of several subimages, and each subimage was digitally captured on four successive frames to allow for time-averaging. Along the 1°, 4°, 7° and 10° depression angle pixel rows, every tenth

TABLE 5.4

TRANSMITTANCES FOR PT. SUR LIGHTHOUSE DATA

Obtained from LOWTRAN 6 (modified by Wollenweber)

	<u>1/30/92</u>	<u>2/2/92</u>	<u>2/4/92</u>
Horizon Angle	90.31°	90.31°	90.28°
Range to Horizon (km)	37.058	35.021	40.902
Height of Eye (m)	114.3	114.6	114.0
Atmospheric Temp (°C)	17.9	14.7	20.3

Long-wave (8-14 μm)

<u>Angle Below Horizon</u>	<u>1/30/92</u>	<u>2/2/92</u>	<u>2/4/92</u>
1°	.4468	.3872	.4786
4°	.7164	.6814	.7361
7°	.7952	.7698	.8084
10°	.8346	.8149	.8452

Short-wave (2-5.6 μm)

<u>Angle Below Horizon</u>	<u>1/30/92</u>	<u>2/2/92</u>	<u>2/4/92</u>
1°	.3513	.3345	.3568
4°	.4717	.4599	.4778
7°	.5206	.5102	.5267
10°	.5515	.5416	.5572

Table 5.5

EMISSIONS FOR PT. SUR LIGHTHOUSE DATA

Obtained from the computer code EMISS yielding
the Schwartz and Hon value of 10 μ m emissivity

	<u>1/30/92</u>	<u>2/2/92</u>	<u>2/4/92</u>
<u>Wind Speed</u>	1.03 m/s	2.90 m/s	2.20 m/s
24 Hr average wind <u>speed</u>	1.344 m/s	2.961 m/s	1.876m/s

	<u>Emissions</u>		
<u>Angle Below Horizon</u>			
1°	.208	.366	.305
4°	.447	.534	.499
7°	.600	.654	.633
10°	.722	.754	.741

pixel value (uncompensated equivalent blackbody temperatures in °C) was recorded across the angular width of each glitter pattern as computed from Tropf's computer code, SUN GLITTER (Appendix A).

Once the apparent blackbody temperature data for specified rows of pixels was extracted from the sun glitter images, each set represented the spatial distribution of those apparent (uncompensated) temperatures for horizontal pixel rows at the 1°, 4°, 7° and 10° depression angles within a given glitter corridor. These ordered values within each data set comprised vectors which could then be input into the MATLAB routine AGACOMP.M (Appendix B) to compensate for emissivity variations and atmospheric effects. AGACOMP.M performs a point-by-point computation yielding the compensated output data in vector form and expressed in terms of source radiance ($\text{Watts/cm}^2 \cdot \text{sr}$). These source radiance vectors were then averaged together over the four frames of data of each subimage and manipulated using MATLAB's internal functions to yield histograms and plots of the time-averaged, compensated sun glitter radiances as well as statistical information (the mean and standard deviation) of that data (see Table 6.1).

A summary of the procedure followed in the analysis of data for this thesis is as follows:

1. Determine the angle to the horizon for each data collection day; from this identify for each scene the 1°, 4°, 7° and 10° positions below the horizon using the relation that 1 pixel is $0.05^\circ \times 0.05^\circ$ in size

2. Compute the transmissivities at the 1° , 4° , 7° and 10° positions below the horizon using LOWTRAN 6 (modified by Wollenweber)
3. Compute the $10\ \mu\text{m}$ Schwartz and Hon value of emissivity $\epsilon_{\text{S\&H}}$ as a function of wind speed and view angle using the computer code EMISS ($4\ \mu\text{m}$ and $10\ \mu\text{m}$ values of emissivity are within 3% of one another, permitting use of $\epsilon_{\text{S\&H}}$ in both wavebands)
4. Compute the width of each day's glitter pattern as defined by the angular extent around the sun's azimuth that contains $\pm 2\sigma$ of wave slope data (Wu's form) by using Tropf's code SUN GLITTER (Appendix A)
5. Extract the uncompensated equivalent blackbody temperature values from every tenth pixel across the width of each glitter pattern as computed in step 4 at each of the 1° , 4° , 7° and 10° positions below the horizon
6. Execute the MATLAB routine AGACOMP.M for each set of data in each waveband data over each of 4 frames from each subimage. The output data sets represent the corrected spatial distribution of equivalent blackbody source radiance across each glitter pattern for specific horizontal rows of pixels below the horizon
7. Average each of the 4 sets of data from each subimage over the same horizontal rows to produce time-averaged radiance data

VI. RESULTS

Following the procedures of Chapter V, all of the raw data collected for this thesis was converted into compensated data and manipulated into useable form for output. The three principal output products (width information, radiance vs. azimuth plots, and radiance histograms) will be presented in this chapter, and will be used to demonstrate various trends and commonalities between sun glitter patterns in both wavebands. Additionally, practical comparisons to theory and previous data collection studies will be made using this data the results of which will provide evidence in support of the usefulness of this method for collecting and analyzing sun glitter in the IR.

A. GLITTER PATTERN WIDTH

As predicted by Cox and Munk, the width of a glitter pattern appears to increase with increasing wind speed for an observer whose view angle coincides with the solar azimuth. For this work, the day with the highest 24 hour averaged wind speed (2/2/92, 2.961 m/s) showed a wider glitter pattern than the day with the lowest 24 hour averaged wind speed (1/30/92, 1.344 m/s). Using the wave slope statistics derived by Wu as input into the Cox and Munk sun glitter geometry equations (within the FORTRAN program SUN GLITTER), the widths

TABLE 6.1

SUN GLITTER CORRIDOR HALF WIDTHS AT $\pm 2\sigma$ WAVE SLOPE

Computed using Wu's wave slope statistics
as input to Tropf's code SUN GLITTER (Appendix A)

Angle <u>Below Horizon</u>	2330 GMT <u>1/30/92</u>	2330 GMT <u>2/2/92</u>	2300 GMT <u>2/4/92</u>
1°	3.10°	5.38°	4.88°
4°	4.18°	6.57°	6.31°
7°	5.23°	7.77°	7.70°
10°	6.24°	8.97°	9.06°
<u>Wind Speed</u>	1.03 m/s	2.90 m/s	2.2 m/s
<u>24 Hr Avg. Wind Speed</u>	1.344 m/s	2.944 m/s	1.876m/s

at specified depression angles were computed and are presented in Table 6.1. Note that as the viewing depression angle increases for this low altitude, constant height of eye perspective, the glitter pattern widens. Were the observer's height of eye greater, the entire pattern would have appeared as a broadened elliptical or circular pattern of highlights (dependent on the angle of the sun). So, for low altitude viewing, simulating shipboard conditions, a low solar angle glitter pattern will appear as an ever broadening corridor of specular highlights.

The location of the edges in the imaged glitter patterns showed strong agreement to these calculations. There is also

good comparison between Tropf's width computations [Ref. 33] and the ones presented here, despite his use of Cox and Munk's wave slope statistics over those of Wu.

B. PLOTS OF GLITTER SOURCE RADIANCE VS. AZIMUTH

After compensating all individual horizontal rows of data for atmospheric and surface emissivity effects, the vectorized source radiance information from each of the four separate frames of each subimage were averaged into vectors corresponding to each glitter pattern's spatial distribution of time-averaged source radiances at specified depression angles. These subimage radiance vectors were combined with the other averaged subimage vectors taken from along the same horizontal row to create large, single vectors which contained the spatially oriented, compensated source radiance data over the entire glitter pattern width at those depression angles. These vectors as plotted against the azimuthal angle relative to the sun azimuth are presented in Figures 6.1-6.6 (where 0° represents the center of the glitter corridor, coincident with the local solar azimuth). Calculations of the mean and standard deviation for the same data before time-averaging are presented in Table 6.2.

The algorithm within the MATLAB routine AGACOMP.M was used to remove the effects of path radiance and atmospheric extinction from the raw data. The only variations in radiance across the width of a sun glitter pattern, then, were

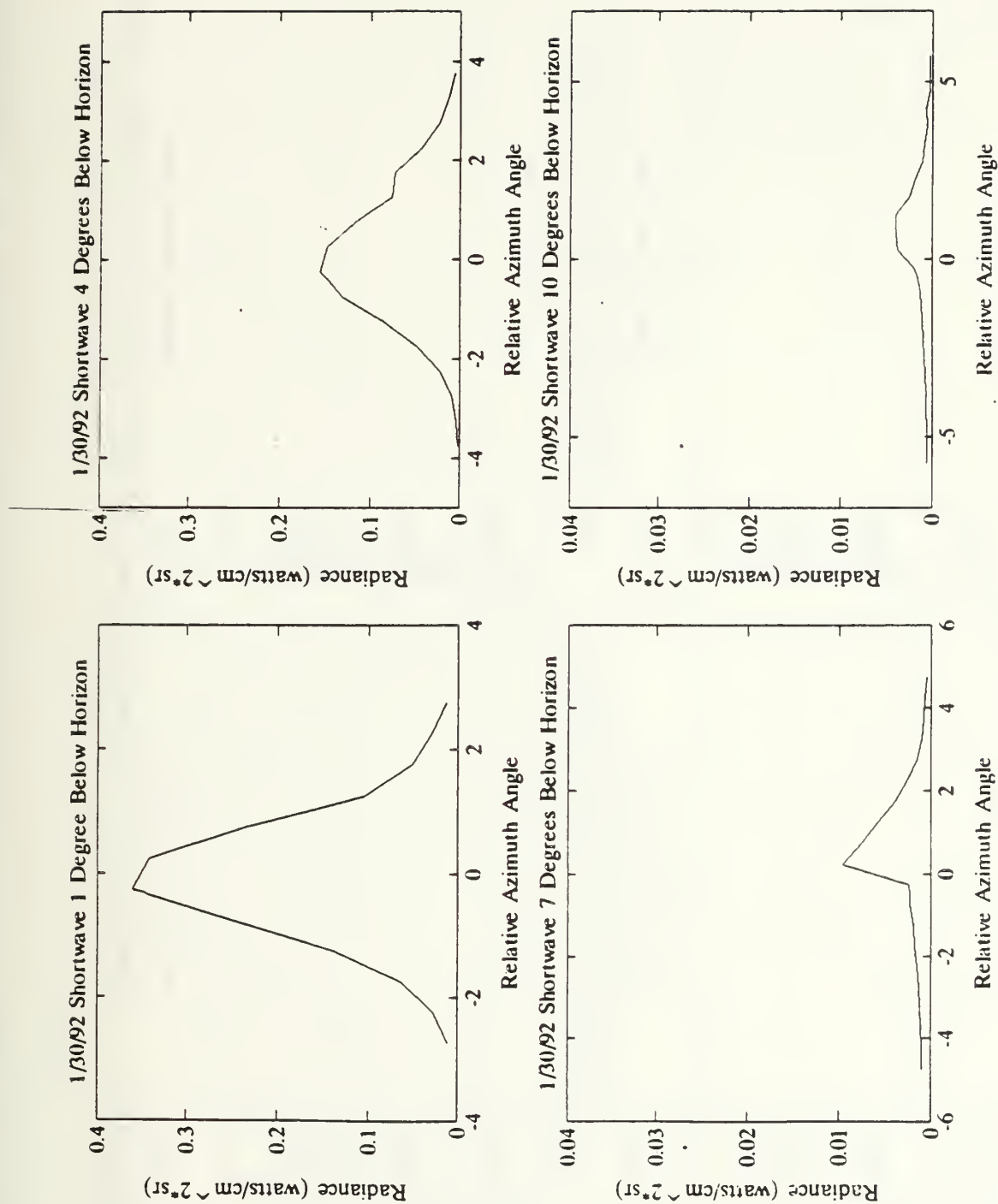


Figure 6.1 Spatial 2-5-6 μ m sun glitter radiance distributions for 1/30/92

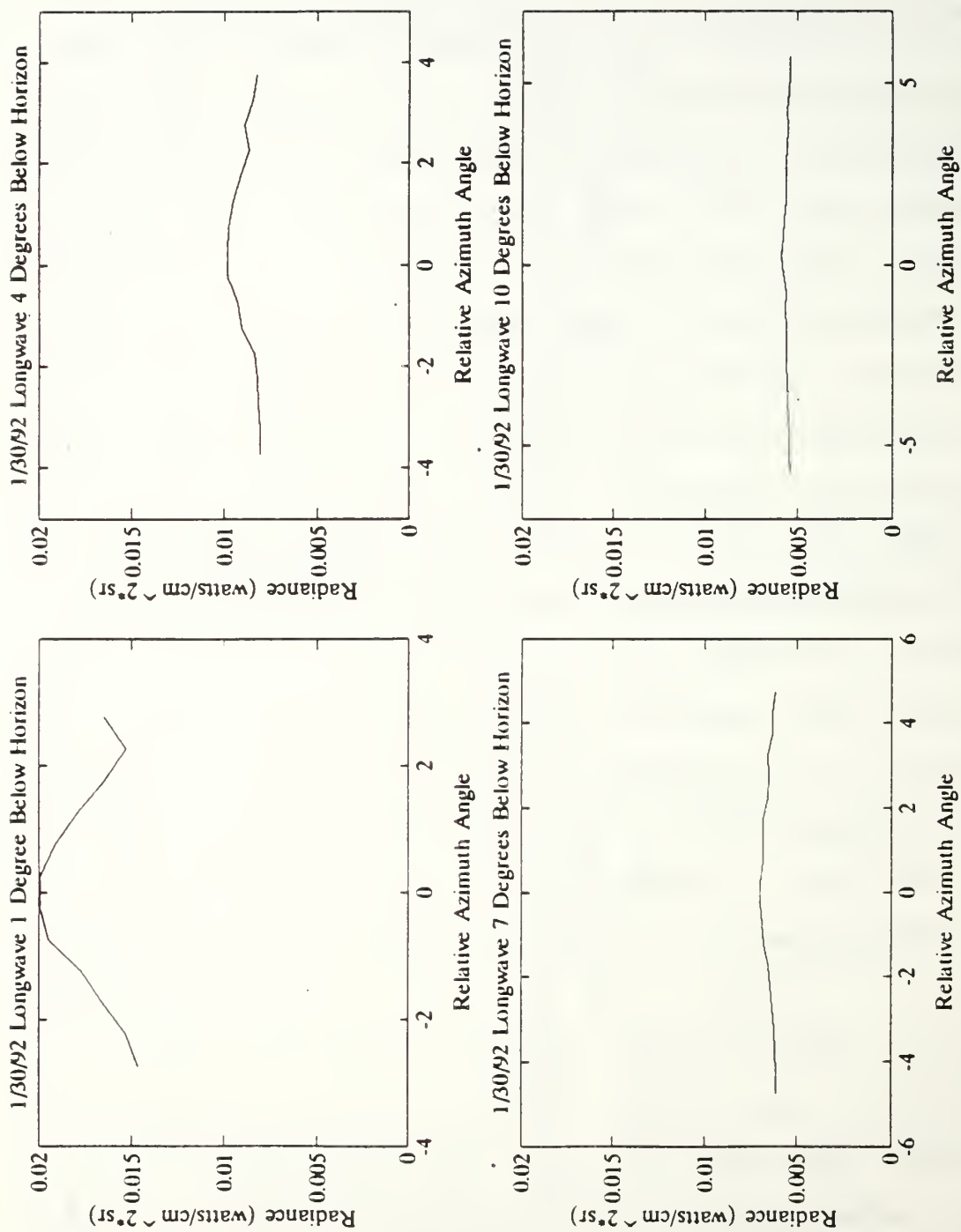


Figure 6.2 Spatial 8-14 μm sun glitter radiance distributions for 1/30/92

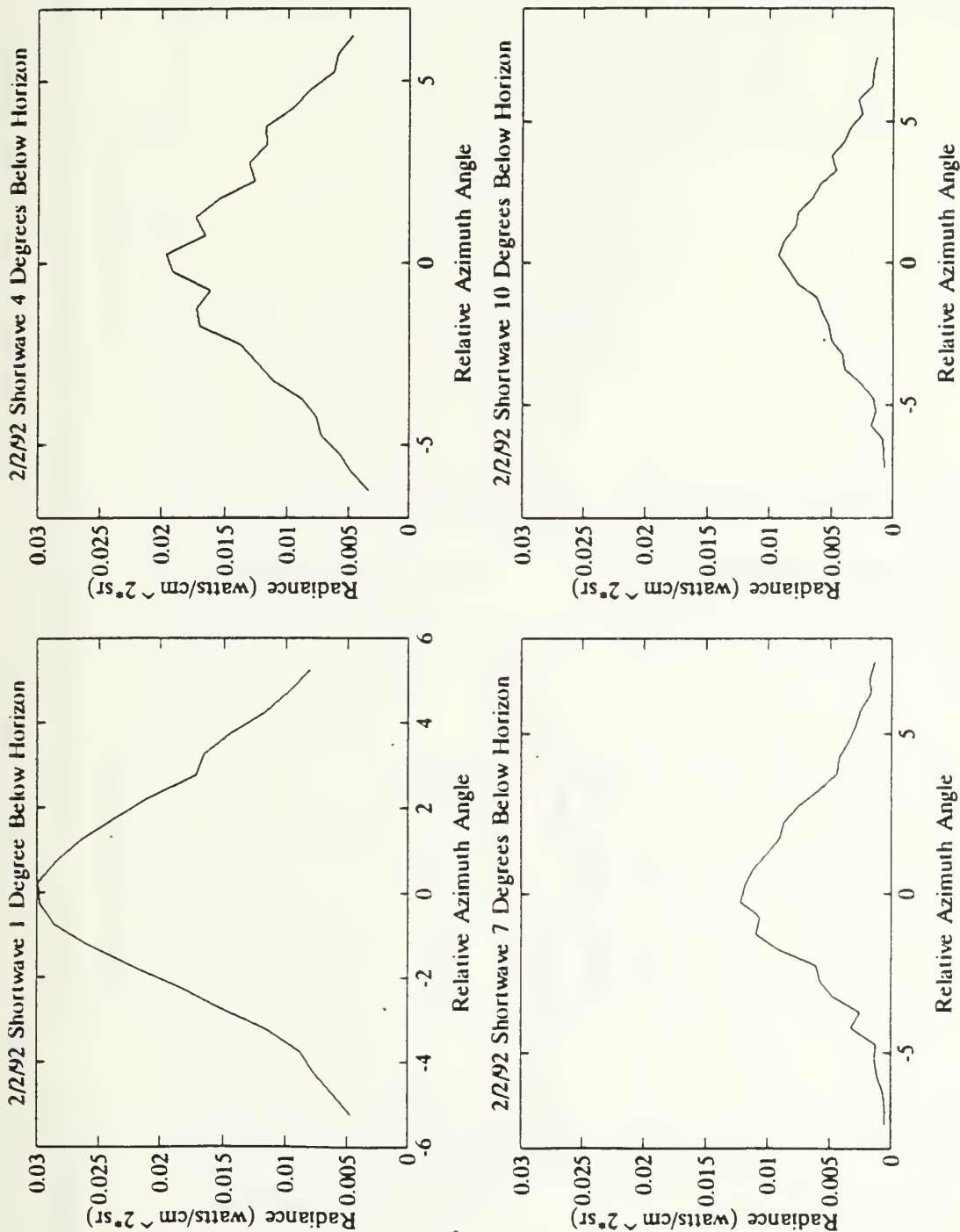


Figure 6.3 Spatial 2-5.6 μm sun glitter radiance distributions for 2/2/92

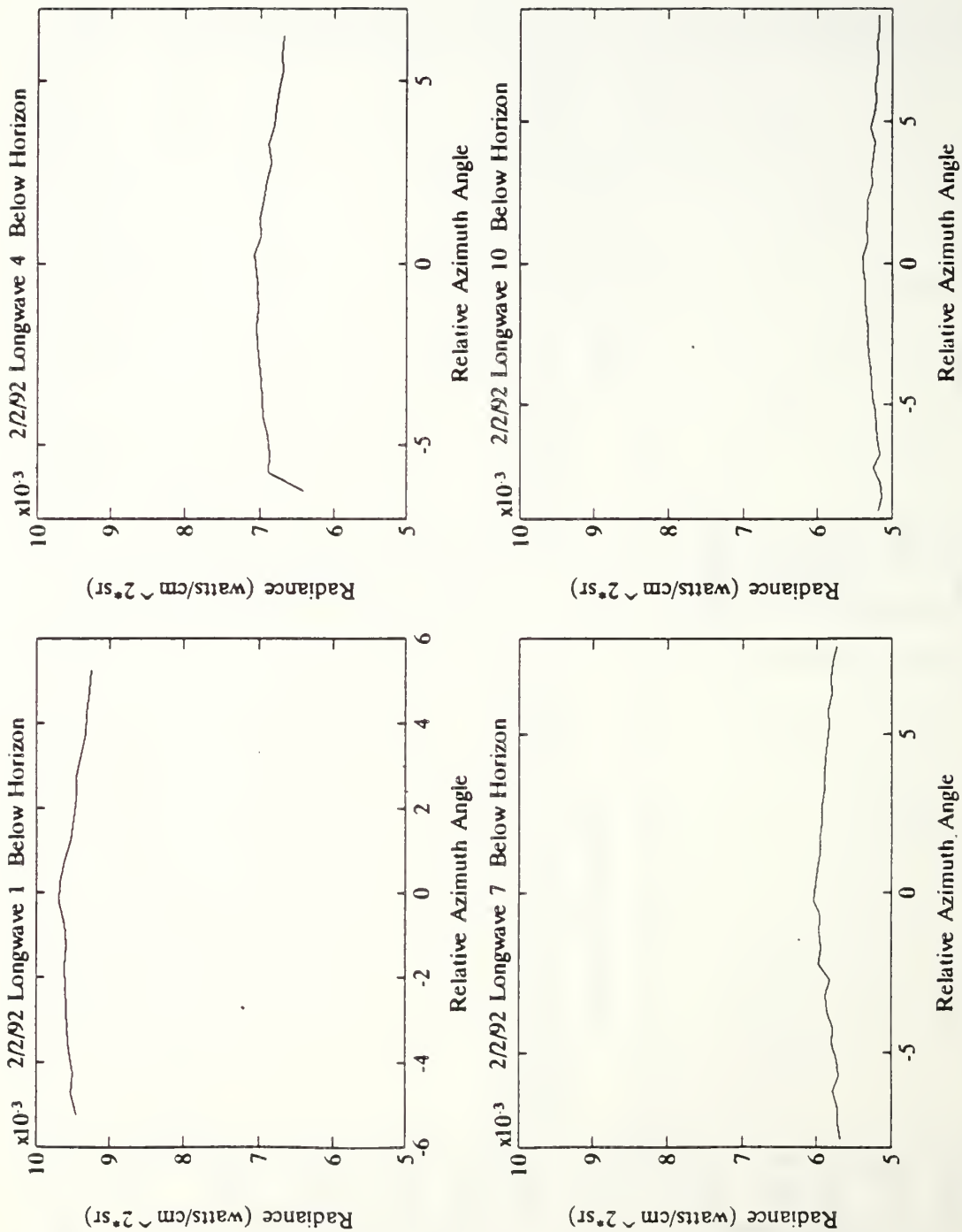


Figure 6.4 Spatial 8-14 μm sun glitter radiance distributions for 2/2/92

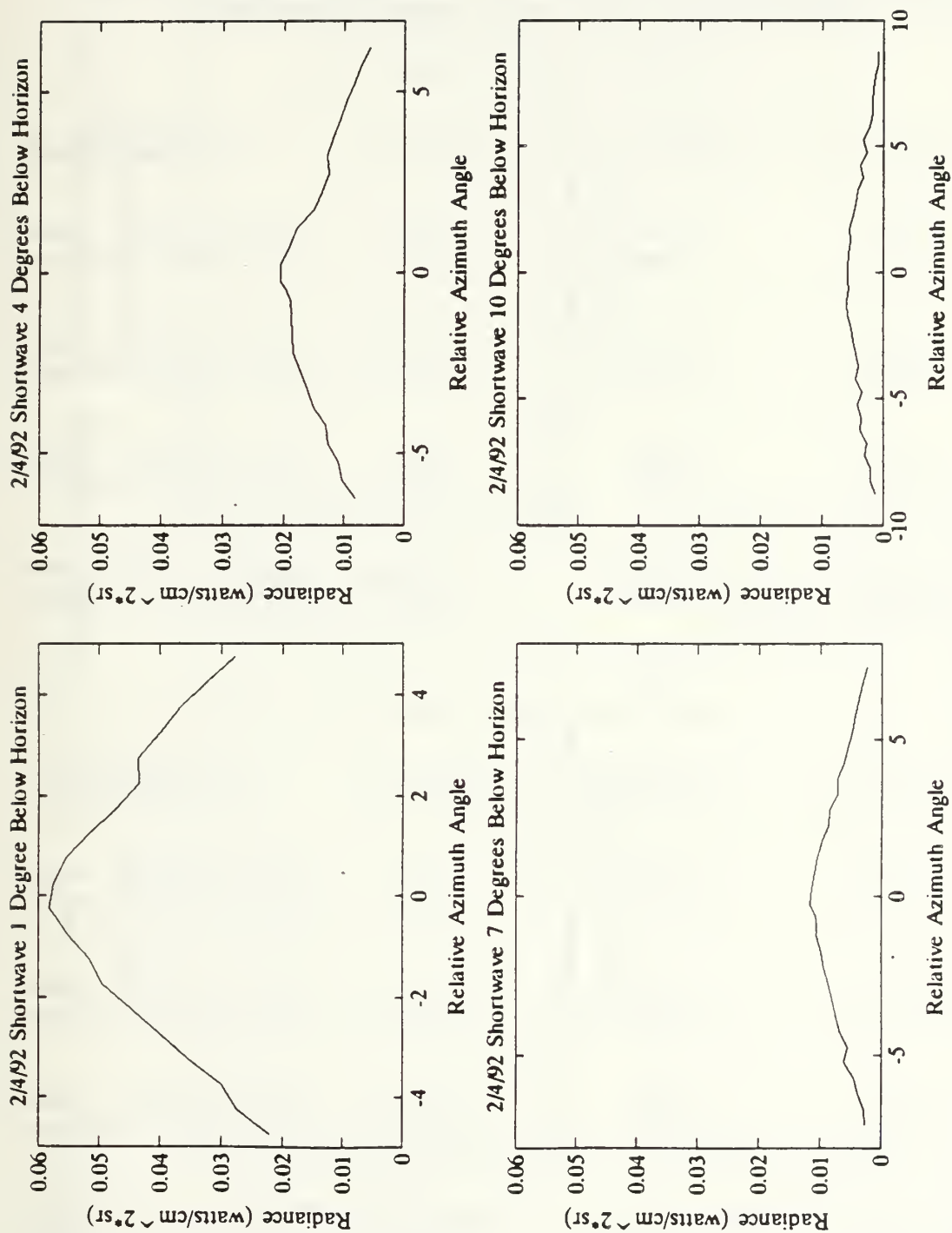


Figure 6.5 Spatial 2-5.6 μm sun glitter radiance distributions for 2/4/92

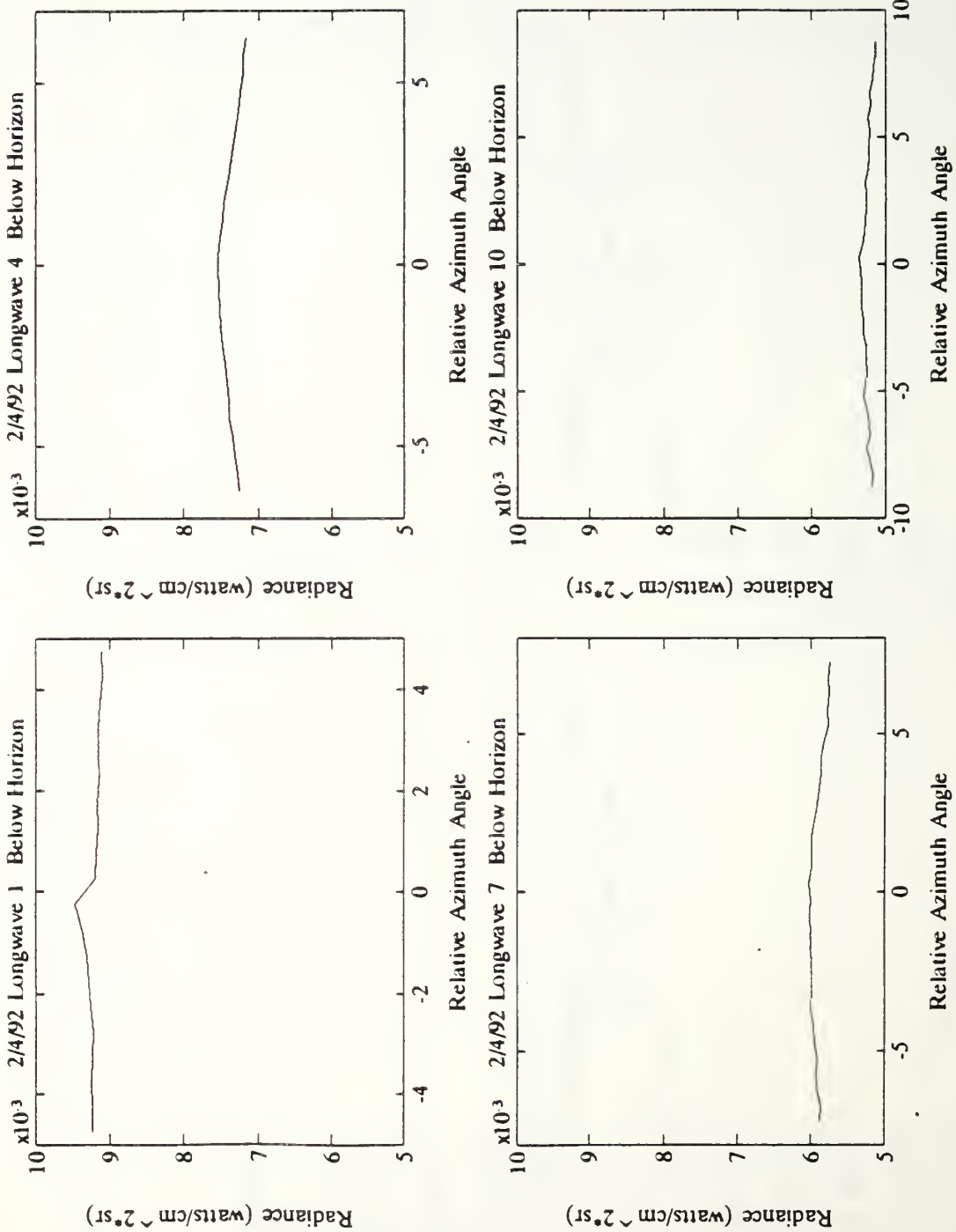


Figure 6.6 Spatial 8-14 μm sun glitter radiance distributions for 2/4/92

TABLE 6.2

**STATISTICS OF THE COMPENSATED SUN GLITTER SOURCE
RADIANCE VALUES (BEFORE TIME-AVERAGING) FOR SPECIFIED
HORIZONTAL PIXEL ROWS BELOW THE HORIZON**

A. Short-wave (2-5.6 μm)

<u>Angle</u> <u>Below Horizon</u>	<u>1/30/92</u>	<u>2/2/92</u>	<u>2/4/92</u>
1°			
mean (watt/cm ² ·sr)	.1365	.0175	.0425
standard deviation	.1349	.0083	.0112
4°			
mean (watt/cm ² ·sr)	.0598	.0115	.0140
standard deviation	.0555	.0050	.0048
7°			
mean (watt/cm ² ·sr)	.0024	.0053	.0070
standard deviation	.0025	.0040	.0031
10°			
mean (watt/cm ² ·sr)	.0013	.0043	.0036
standard deviation	.0013	.0028	.0018

B. Long-wave (8-14 μm)

<u>Angle</u> <u>Below Horizon</u>	<u>1/30/92</u>	<u>2/2/92</u>	<u>2/4/92</u>
1°			
mean (watt/cm ² ·sr)	.0174	.0095	.0092
standard deviation	.0019	1.535x10 ⁻⁴	9.357x10 ⁻⁴
4°			
mean (watt/cm ² ·sr)	.0088	.0069	.0092
standard deviation	7.131x10 ⁻⁴	2.096x10 ⁻⁴	1.172x10 ⁻⁴
7°			
mean (watt/cm ² ·sr)	.0065	.0053	.0059
standard deviation	3.092x10 ⁻⁴	1.149x10 ⁻⁴	9.635x10 ⁻⁴
10°			
mean (watt/cm ² ·sr)	.0056	.0053	.0052
standard deviation	1.588x10 ⁻⁴	8.808x10 ⁻⁴	6.484x10 ⁻⁴

apparently due to variations in source radiance resultant from local wave slopes and the changing strength of direct solar reflections as the viewing azimuth increased away from the sun's azimuth. Compensated source radiance values along the elevation of the sun glitter patterns showed additional variations corresponding to changes in the surface emissivity with view angle. At the same viewing depression angle, windy days produced rough sea surfaces which had higher emissivities than calm surfaces on days with less wind (winds in this context implies the 24 hour average wind speeds, see Table 6.1). By Equation (2.6), higher emissivities equate to lower reflectivities. With all factors other than wind speed held constant, radiances measured at similar depression angles varied with wind speed such that days with light winds had higher radiances than days with higher winds.

One data artifact worth noting is contained in the long-wave glitter radiance pattern at the 1° depression angle for the 1/30/92 data (Figure 6.2). Among all long-wave radiance plots, this one shows the most variance between glitter edge and center measurements. The likely cause of this is the low wind speed for that day (1.344 m/s 24 hour average) as compared to the other two days. Low wind speeds cause less roughness on the ocean surface with higher reflection coefficients resulting; this means that more sky and solar radiance would seem to emanate from the surface of the ocean. This effect (higher radiance at low wind speeds) would be most

pronounced at near grazing view angles where reflectivity is highest, and would tend to be less important as the viewing depression angle is increased. For the 2/2/92 and 2/4/92 1° depression angle data, higher wind speeds reduced this effect, causing the radiance response in those plots to appear relatively flatter by comparison.

With only one minor exception, all of the short-wave sun glitter patterns showed a gaussian shape across their azimuth. The exception is the 7° depression angle pattern for the 1/30/92 data (Figure 6.2), where a possible error in pointing the AGA imager or interference from the large northwest ocean swell resulted in an apparent linear drop in radiance near the center of the pattern. Ignoring this artifact, that pattern should tend to follow the shape of the other curves for that day and appear gaussian as well.

As the viewing depression angle was increased, the short-wave radiances (and long-wave as can best be ascertained) had their maximum values near the horizon and then decreased as the viewing angle was aimed further downward. This meant that the difference between center and edge radiances was greatest for glitter images taken near the horizon during periods of low solar angles. If the sun were higher in the sky and the observer's height of eye were greater, or if the wind speed were lower acting to reduce the effects of wave slope shadowing, these patterns would also have had a gaussian shape in elevation. The work presented here, then, is valid for

most shipboard or sea skimming missiles applications where height of eye is low and the resultant view angles are within 10° of grazing on wind roughened surfaces. The sun glitter pattern for these conditions should appear as an ever widening corridor of highlights (essentially a half gaussian shape) regardless of the solar elevation due to the relatively low height of eye of the observer.

An additional corollary to the radiance distribution of a sun glitter pattern in the vertical direction arises from examining the impact of wind induced contrasts between each day's 1° and 10° depression angle's maximum radiance values. Data analyzed for this thesis shows that in both wavebands there is a greater delta between the 1° and 10° depression angles' maximum radiance values for days with low wind speeds as compared to days with higher wind speeds. On 1/30/92, for example, the difference between these two values for a wind speed of 1.03 m/s was 98.9% of the overall maximum radiance for that day, whereas on 2/2/92 this delta decreased to 69.23% for a wind speed of 2.90 m/s. These results support both Gambling's [Ref. 32] and Hughes' [Ref. 13] findings relating to wind induced radiance contrasts within a glitter pattern as discussed in section IV.E.2.b of this thesis.

As was expected, the long-wave measurements showed far less solar interference than those in the short-wave. This is supported by the fact that the 8-14 μm waveband accounts for

only 0.09863% of the sun's irradiance at sea level while the 2-5.6 μm waveband contains 6.136% of this irradiance [Ref. 12:p. 3-36]. These percentages equate to equivalent sea level in-band blackbody radiances (from sun glitter only) of 0.1288 watts/cm²·sr for the long waveband and 8.018 watts/cm²·sr for the short waveband (computed using the constant 260 w/m² for total sea level solar irradiance of the sun at 80° from zenith [Ref. 12:Table 3-2], $1.9\pi \times 10^{-5}$ sr for the solid angle of the sun disk in the sky [Ref. 4:p. 48] and an average wave facet reflectivity of 0.3). These calculated values are simply intended to demonstrate the wide difference between glinting radiances in the two wavebands while providing representative values of glitter radiances computed using first principle methods.

Measured (and compensated) sea surface radiances varied from these values due to differences in solar position, atmospheric transmissivity and sea surface reflectance. In the 2-5.6 μm waveband, maximum measured radiances (at the center of the sun glitter pattern) were between 0.031 and 0.36 watts/cm²·sr, which are up to two orders of magnitude away from the theoretical value computed above. Long waveband (8-14 μm) maximum radiances were measured between 0.0095 and 0.02 watts/cm²·sr, and are in closer agreement with the theoretical value of 0.1288 watts/cm²·sr.

One source of the discrepancy between these theoretical and measured values is attributable to less than perfect

detector responsivities in both wavebands. For a given bandwidth, if the scanner's responsivity is less than unity (a realistic case not accounted for in the above theoretical computation of sun glitter radiances) then there would be less radiance recorded by that detector. This would in turn decrease the differences between the computed theoretical and measured shortwave sun glitter radiance values by perhaps as much as 50% over the entire bandwidth, depending upon the sensor.

A second source of error between the theoretical values calculated above and the measured values herein is due to differences in the angular dimensions between an AGA 780 pixel and the solar disk. Because the sun reflects through a solid angle of $1.9\pi \times 10^{-5}$ sr and the size of the pixel measuring it is $2.4\pi \times 10^{-5}$ sr, the sun's image will not fill the area of a pixel. Thus, there will not be an exact correlation between solar reflected radiances (computed from theory) and measured radiances due to cooler areas around the image of the sun acting to lower the effective temperature received by the AGA. The extent to which the effect impacts IR sensing is dependent upon the temperature of the background sea surface.

Evidence of limited solar interference in the long-wave is supported by looking at the relatively flat response of 8-14 μm radiances across the width of the sun glitter patterns over the three sets of data in Figures 6.2, 6.4 and 6.6, each of which provided a nearly gaussian characteristic shape in their

corresponding short-wave plots. There were, however, some small variations in the long-wave sun glitter radiances that were consistent with a bell-shaped pattern but with much smaller differential radiances between each pattern's edge and center than in the short-wave. The ability to discern this degree of radiance difference from normal self-emission and sky reflected backgrounds, however, is dependent upon the sensitivity of the detector in use. In the case of the AGA 780, its noise equivalent temperature difference (NETD) of 0.12° at 22° C provides the ability to discern radiance differences of 9.6154×10^{-6} watt/cm²·sr in the long-wave and 1.356×10^{-6} watt/cm²·sr in the short-wave (computed assuming $\epsilon = \tau = 1$). Comparison of these sensitivities to the in-band direct solar contributions to sea surface radiances previously calculated (8.018 and 0.1288 watt/cm²·sr in the short and long waveband, respectively) reveals that the AGA 780 should have no trouble detecting sun glitter over additional background clutter. For other systems this may present an obstacle to sensing sun glitter if that system's sensitivity is too low.

The basic problem, however, is not one of detecting sun glitter, but rather avoiding its interference in remote IR sensing applications where receiver sensitivities are intentionally made low in order to support target recognition (thereby making them susceptible to degradation by sun glitter). As has already been seen, there is less of the sun's energy in the long waveband, which makes it the better

choice for use in regions of high intensity sun glitter (especially in dual band systems like the AGA 780). The appropriate conclusion, therefore, would be to use long-wave sensing during periods of vulnerability to sun glitter (perhaps using some means of "handing off" between wavebands) since that band is better suited to avoid its detrimental effects.

C. HISTOGRAMS OF SUN GLITTER RADIANCE DATA

A third means of analyzing sun glitter data is realized through plotting histograms of the non time-averaged radiances after compensation for varying emissivity and atmospheric effects. Each set of histograms, plotted on the same scale for that day's data, should graphically reveal information regarding the statistical nature of sun glitter that would otherwise be lost through the time-averaging process. Each day's histograms for both wavebands are presented as Figures 6.7-6.12.

Looking first to the short-wave histograms (Figures 6.7, 6.9 and 6.11), one trend appears to dominate all graphs: that low radiance values occurred most often at greater viewing depression angles. This finding is consistent with what is shown by the graphs for the same time-averaged data.

Relationships between the data's mean values and standard deviations are more clearly revealed in the histograms. For a day with low wind (1/30/92, 1.344 m/s 24 hour average),

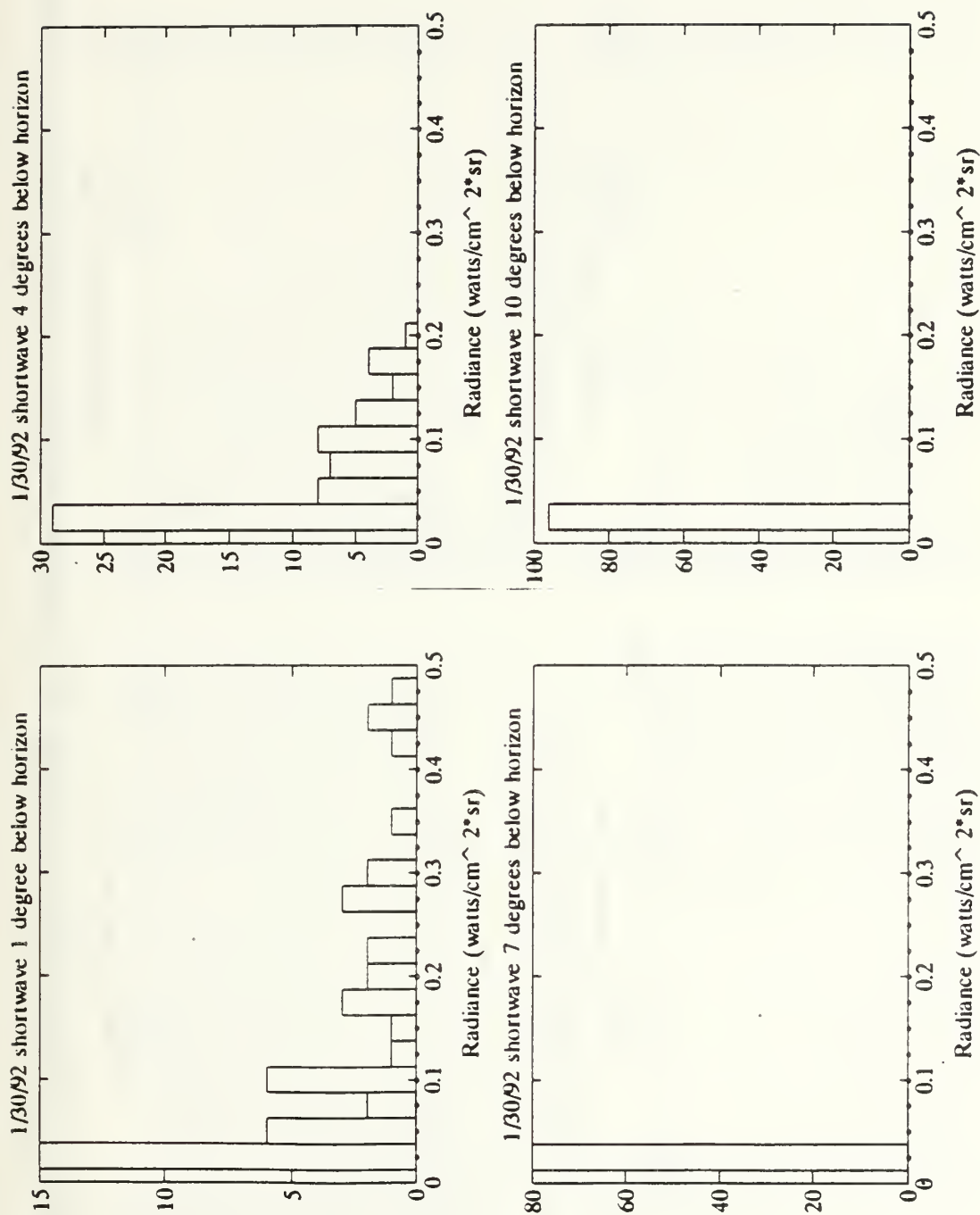


Figure 6.7 Histograms of 1/30/92 sun glitter radiance in the 2-5.6 μm waveband

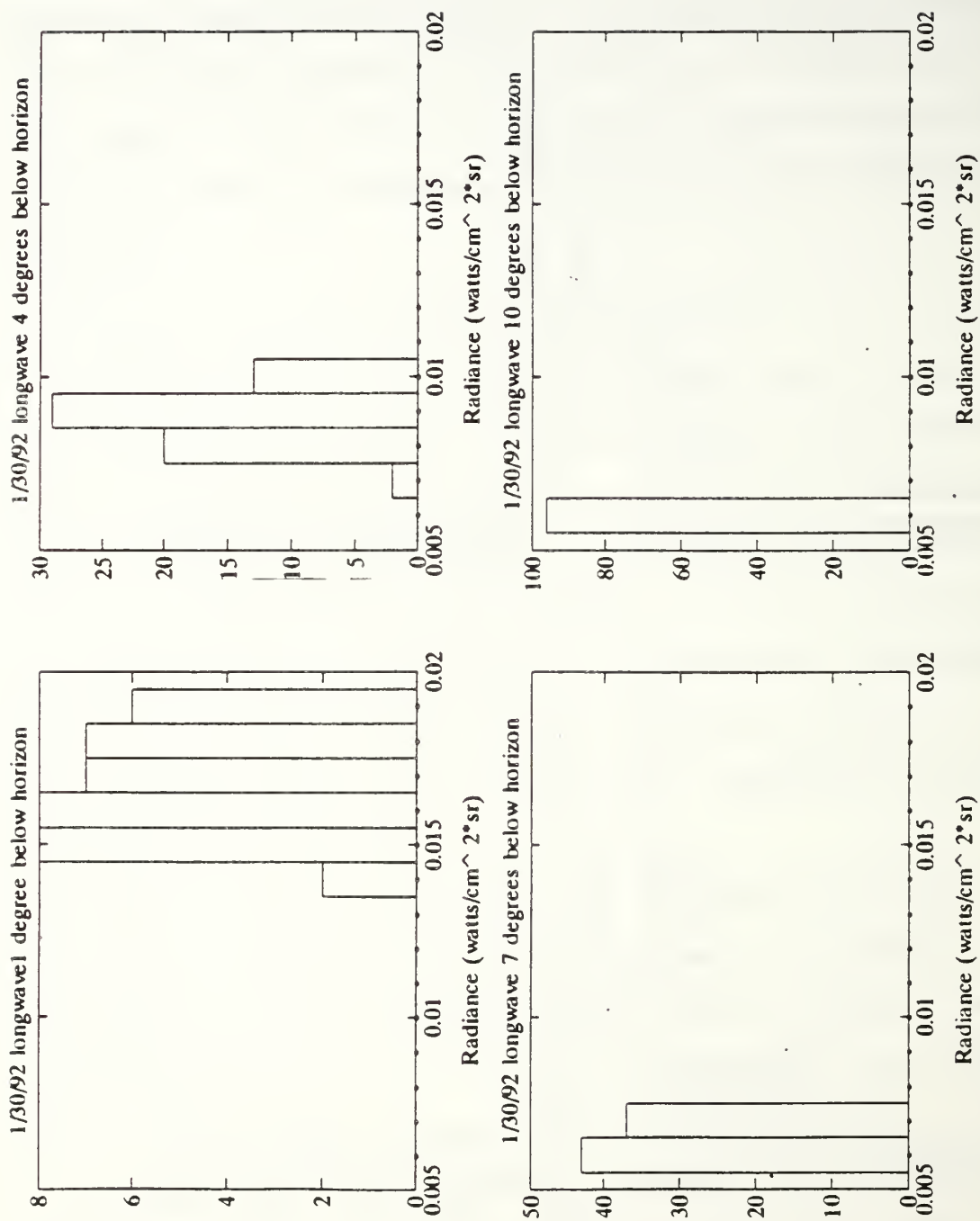


Figure 6.8 Histograms of 1/30/92 sun glitter radiance in the 8-14 μm waveband

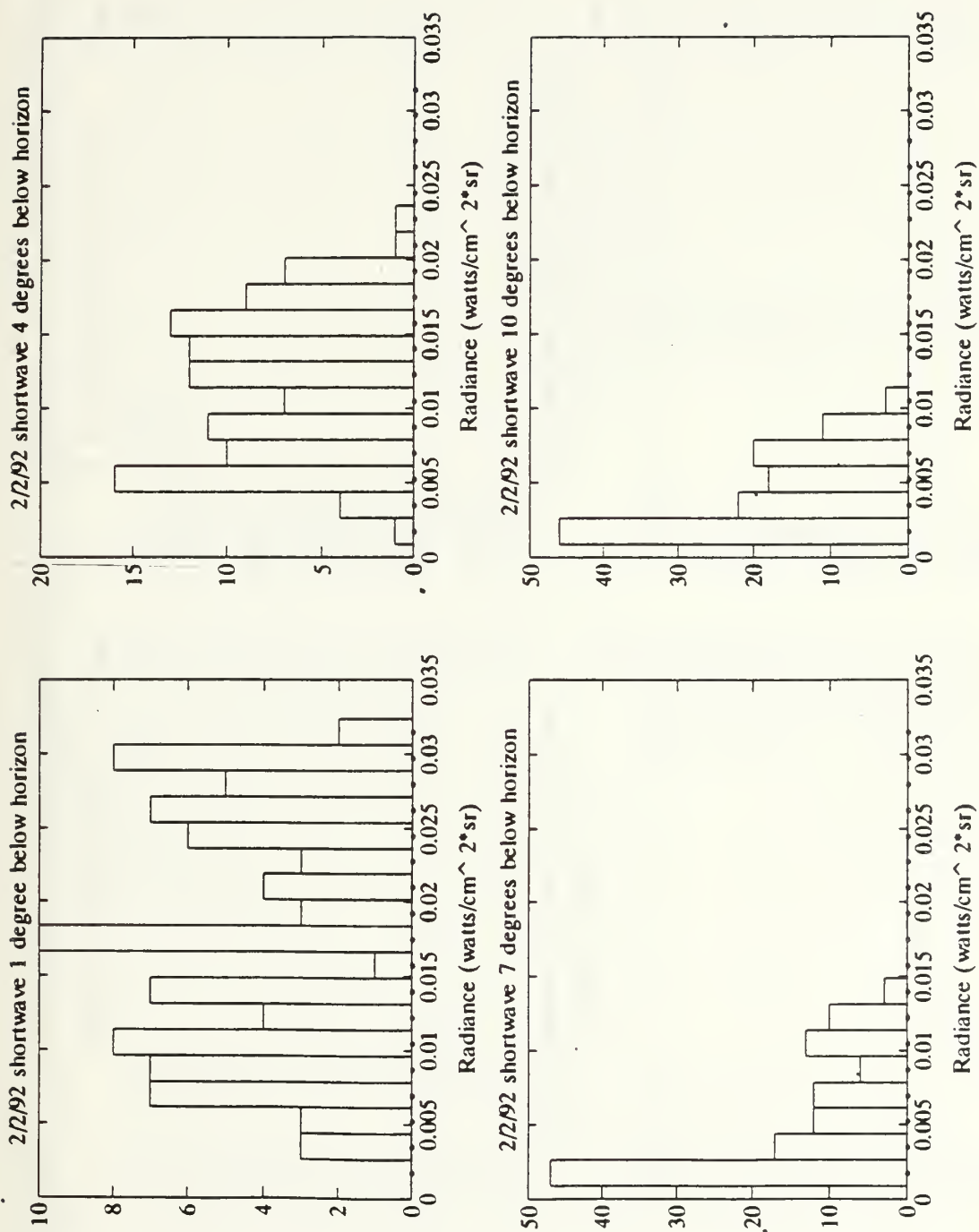


Figure 6.9 Histograms of 2/2/92 sun glitter radiance in the 2-5.6 μm waveband

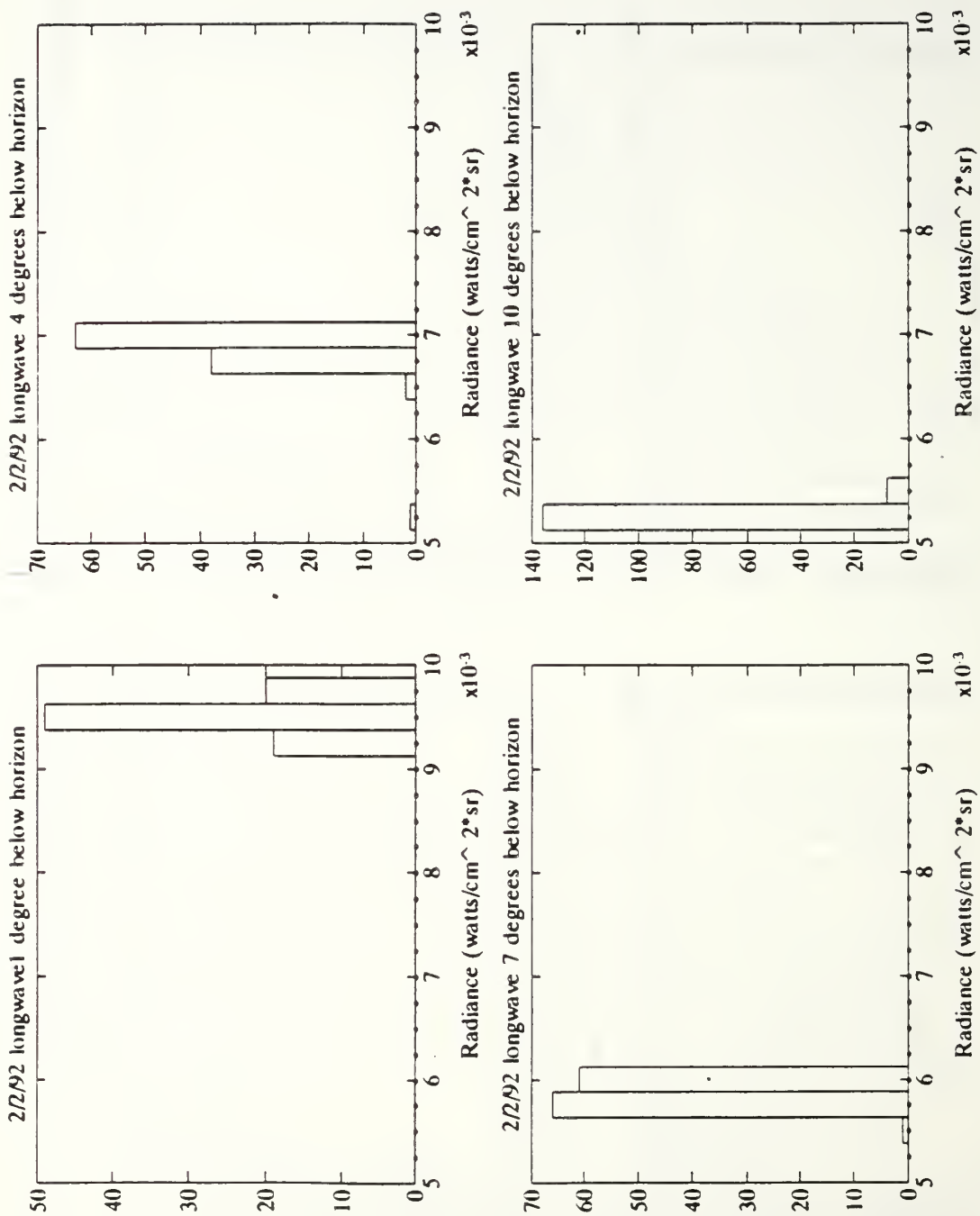


Figure 6.10 Histograms of 2/2/92 sun glitter radiance in the 8-14 μm waveband

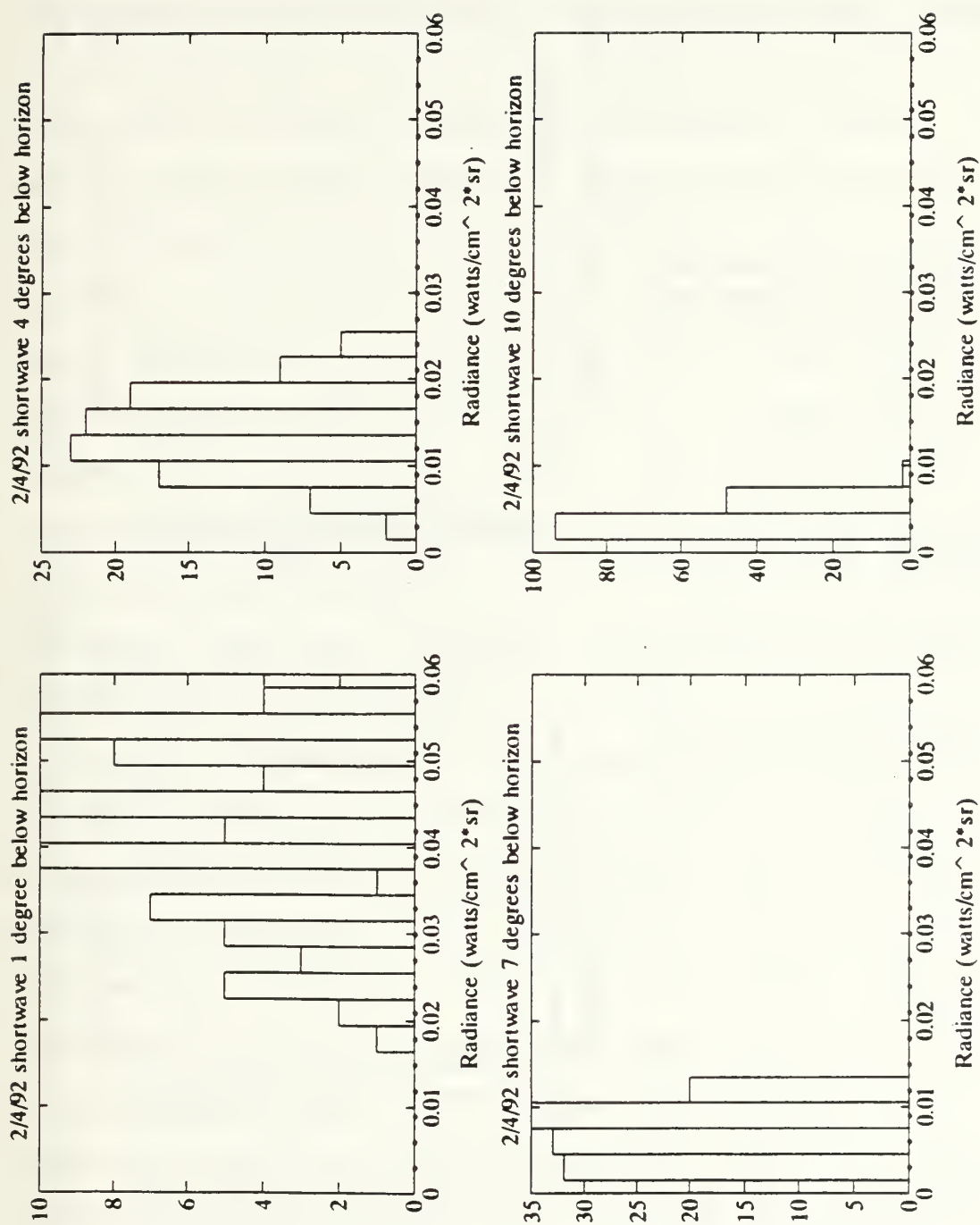


Figure 6.11 Histograms of 2/4/92 sun glitter radiance in the 2-5.6 μm waveband

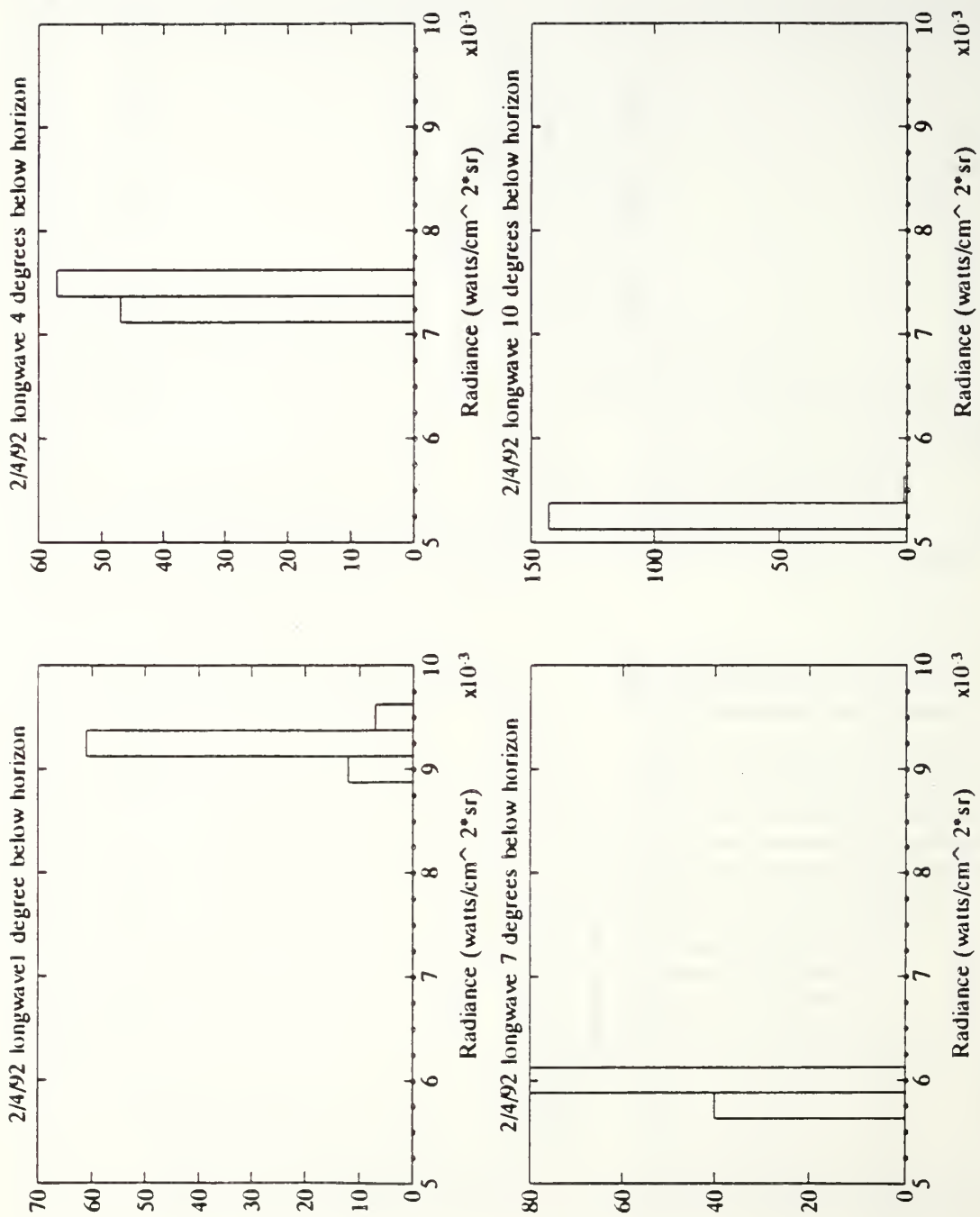


Figure 6.12 Histograms of 2/4/92 sun glitter radiance in the 8-14 μm waveband

radiance values were generally higher and showed more variance than days with stronger winds, although high wind days showed a more even distribution of the data about the mean. Looking at the histograms of the 1° positions, the 1/30/92 data appears to be skewed toward lower radiance values, while several outlying data points at higher radiances cause the mean to shift to the more intermediate value of $0.1365 \text{ watt/cm}^2 \cdot \text{sr}$. On 2/2/92, the day with the greatest winds, the same 1° depression angle data appears more evenly distributed about a mean value of $0.0175 \text{ watt/cm}^2 \cdot \text{sr}$. At other depression angles, the 2/2/92 data remains more variate than the corresponding lower wind speed data of 1/30/92, yet still shows the common decrease in overall radiance as the viewing depression angle was increased (a trend seen in both the spatial plots and histograms).

Among the histograms for long-wave data, also plotted on the same scales for all depression angles on each day, there is much less variation in the data than in the corresponding short-wave histograms. This graphically illustrates the same information regarding this data's standard deviations contained in Table 6.2, namely that long-wave sensors will be less affected by sun glitter than those operating in the short-wave due to the small portion of the solar spectrum represented there. Data in the long-wave IR, although at a much higher signal-to-glitter ratio than short-wave sun glitter data, still showed the familiar trend toward lower

radiance values as the viewing depression angle was increased.

D. COMPARISON OF RADIANCE VALUES TO PREVIOUS RESEARCH

The results of this thesis showed variations between what was computed from first principle theory for maximum sun glitter radiances and what was measured in the experiments. These differences were reasonable in light of the non-specific data used to compute the theoretical sun glitter radiance values of 8.018 and 0.1288 watt/cm²·sr in the 2-5.6 μ m and 8-14 μ m wavebands, respectively. In fact, deviations among measured sea surface radiance values are anticipated due to seasonal, diurnal, and wave-slope induced variations in parameters such as transmissivity, reflectivity and emissivity. Additional differences between glitter radiances measured by different IR receivers are also possible due to varying pixel sizes and system responsivities. Thus, by comparing some representative radiance values from the measurements taken and analyzed for this thesis to those from other related studies, some further insight can be obtained as to the validity of the results and methodology presented herein.

In a work which built upon and further amplified the efforts of Cox and Munk, Saunders [Ref. 16] presented data from sea surface radiance measurements (non-glinting) in the 8.2-12.5 μ m waveband. At a 5° viewing depression angle (no sun angles given), Saunders reported radiances of 2.1-3.3

mw/cm²·sr for data taken during the months of March, October and August with winds of 2-13 m/s. Comparable values from this paper in the 8-14 μ m waveband were 5-9 mw/cm²·sr as obtained from areas furthest from the center of the sun glitter pattern (representing non-glinting radiances) near the same 5° observation angle. The differences here are attributable to the fact that Saunders' measurements are of actual radiances (graybody) and the data from this paper represent apparent blackbody radiances. Therefore, even though Saunders' results appear low, there is some correspondence between the results from these two experiments.

Another paper by Eisner, et al. reported apparent spectral radiances of sun glitter as measured from a river near Cocoa Beach, Florida [Ref. 17]. Their research, conducted for near-grazing incidences and low solar elevations akin to the conditions established for this thesis, reported apparent spectral glinting radiances of 9 mw/cm²·sr· μ m at 2 μ m wavelength, 1.5 mw/cm²·sr· μ m at the 4 μ m wavelength, and 1.1 mw/cm²·sr· μ m for a wavelength of 10 μ m. These values roughly equate to 2-5.6 and 8-14 μ m in-band radiances of 12.9 and 6.6 mw/cm²·sr, respectively. Comparable values of time-averaged glinting radiances from this work were 30-360 mw/cm²·sr in the 2-5.6 μ m waveband and 9.5-20 mw/cm²·sr in the 8-14 μ m waveband. Although Eisner's results appear slightly low in relation to those from this thesis, some of the difference can be explained by accounting for Eisner's failure to compensate

for path radiance and atmospheric transmissivity in his results. Had these effects been included for near horizon measurements such as these (that is, over long path lengths), Eisner's corrected radiances would have been greater and therefore nearer to the results presented herein. Additionally, had Eisner's group expressed their results in equivalent blackbody radiances, the comparisons would have been even closer. Yet even after considering these possible explanations as to why these data sets do not exactly correspond, the results from this thesis still appear high.

In these and other cases, sun glitter measurements from similar research efforts have not compared closely to the data presented here (although after some heuristic manipulation, those of Saunders and Eisner, et al. came close). This implies that there may have been some error in the method used to correct the data from this thesis for atmospheric effects and source emissivity variations.

In the paper "Naval Ocean Infrared Background Analysis" by Ostrowski et al. [Ref. 37], measurements of sun glitter scenes were recorded in order to validate the SEABEAM model [Ref. 3] for use in sun glitter predictions. Their shortwave radiance values, measured at sun and view angles corresponding to those in this work, were again generally low compared to the results presented here. Specifically, they recorded average glitter radiances of $0.5\text{--}1 \text{ mwatt/cm}^2\cdot\text{sr}$ in the $3.1\text{--}5.1 \text{ }\mu\text{m}$ waveband (Dahlgren, VA tests). Converting

these apparent radiance values to equivalent 2-5.6 μm waveband radiances yields results of 0.9-1.8 $\text{mwatt}/\text{cm}^2\cdot\text{sr}$. After accounting for differences due to apparent instead of zero-range source radiances and blackbody vice graybody radiators, Ostrowski's shortwave measurements seem low by a factor of between 5 and 30 compared to this work's corrected shortwave results. Some of this can certainly be attributed to diurnal and seasonal variations as they affect ambient conditions. More likely, though, because of the wide disparity in radiance values they highlight a potential weakness in the formulation of Equation (5.4) to compensate measured radiances for atmospheric effects and source emissivity variations.

The results from this thesis, then, are valuable in that they present a method to measure and define the sea surface sun glitter corridor both physically and statistically in relative terms. Results presented herein serve to show how differing sun and view angles combine with ambient wind conditions to form unique sun glitter patterns for low angle (shipboard) applications.

The attempt to employ an algorithm to correct these measured radiances for atmospheric effects and then express the results as equivalent blackbody source radiances was not completely successful. Greater effort is needed to find a method which more accurately computes and accounts for atmospheric radiance and attenuation within a given scene such that source radiances (graybody radiances as opposed to

blackbody) are provided as output. Expressing the combined source radiance of a glinting sea surface (comprised of the sum of sea self-emission, reflected sky radiance and reflection of direct solar radiance) by its equivalent blackbody radiance (by dividing the equivalent compensated graybody radiance by the emissivity of the sea surface) is apparently improper. This is due to the fact that two of the three source components of the overall source radiance from a glinting sea (sky reflected and direct solar reflected radiances) are affected by that sea's reflectivity, not its emissivity. Thus, a more valid expression of Equation (5.4) would be

$$I_1 = \epsilon_{SH} \tau I_0 + (1 - \epsilon_{SH}) \tau I_{sky} + (1 - \epsilon_{SH}) \tau I_{sun} + (1 - \tau) I_{atm} \quad (6.1)$$

where

- τ = transmissivity from LOWTRAN (modified by Wollenweber)
- ϵ_{SH} = Schwartz and Hon value of sea surface emissivity
- I_{sun} = thermal level of the sun's radiance at sea level
- I_{sky} = thermal level of the sky's radiance at sea level
- I_{atm} = thermal level of the atmosphere corresponding to atmospheric temperature
- I_1 = thermal level corresponding to the flux falling on the AGA 780 detector with $\epsilon = \tau = 1$
- I_0 = thermal level of the sea's self emission.

The total emanated sea surface radiance I_{source} in isothermal units, then, is

$$I_{source} = I_0 \epsilon_{SH} + (1 - \epsilon_{SH}) I_{sky} + (1 - \epsilon_{SH}) I_{sun} \quad (6.2)$$

Thus, a more proper form to use in compensating measured radiances for atmospheric extinction and path radiance is

$$N_{\text{source}} = \frac{N_1 - N_{\text{atm}}}{\tau} \quad (6.3)$$

where

$$\begin{aligned} N_1 &= \text{radiance corresponding to } I_1 \text{ as computed by} \\ &\quad \text{Planck's Integral (Equation (2.2)) using } T_{\text{pixel}} \text{ (as} \\ &\quad \text{read directly from CATS) as input} \\ N_{\text{atm}} &= \text{atmospheric radiance as computed by LOWTRAN 6} \\ \tau &= \text{atmospheric transmissivity as computed by LOWTRAN} \\ &\quad 6 \end{aligned}$$

which expresses N_{source} as the compensated, graybody source radiance of the sea.

Most of the differences between results from Equation (6.4) and those from this thesis are due to the differences between blackbody and graybody radiances (a factor of $1/\epsilon_{\text{S\&H}}$ among radiance terms expressed in isothermal units). The remainder of any differences between these results and those of other researchers is most probably due to an error in the method used to compute path radiance (used in the conversion of apparent radiances to zero range source radiances). The method employed here was to use the relation

$$I_{\text{atm}} = \frac{A}{C \exp(B/T_{\text{atm}}) - 1} - \text{Offset}, \quad (\text{isothermal units}) \quad (6.4)$$

to convert measured atmospheric temperature directly to isothermal units (representing the atmosphere's thermal value for use in Equation (5.4)). In hindsight, it appears that this computation inaccurately computed the path radiance received by a sensor. Because the compensated radiance values from this paper seem high as compared to those from other

works, it is concluded that this method of computing path radiance provided low values for atmospheric path radiance to the algorithm which compensated for atmospheric effects (Equation (5.4)). In turn, an insufficient amount of path radiance was subtracted from the measured radiances. This resulted in corrected radiances which were greater than they should have been had path radiance been calculated properly.

Further work using Equation (6.3) to compensate the data collected for this thesis was performed and revealed improved accuracy in accounting for atmospheric effects (by comparison to Saunders' and the SEABEAM sea radiance model). These results are presented in a forthcoming SPIE paper by Dr. A.W. Cooper, et al. of the Naval Postgraduate School [Ref. 38].

VII. CONCLUSIONS

This thesis has presented the results of efforts to measure and subsequently define the physical and statistical nature of sun glitter on the sea surface. A methodology was formulated and used to extract and analyze raw data from a thermal imaging system taken over a period of three days under differing weather conditions. The results from this process were compensated for atmospheric effects and then expressed as equivalent blackbody source radiances, comprised of the sum of sea self-emission, reflected sky radiance (solar scattering) and direct solar reflections (sun glitter). Comparisons to first principle theoretical computations and the results of previous research efforts showed excellent qualitative results. Quantitatively, these results lacked sufficient accuracy due to having used inexact methods to adjust measured radiances for the effects of atmospheric path radiance and source emissivity variations. Specifically, the analytical results herein were inadequately expressed as equivalent blackbody radiances rather than real, graybody radiances. Additional discrepancies were also due to the improper method chosen to compute atmospheric path radiances.

The overarching requirement which motivates this work is the need to incorporate algorithms into IR sensors which effectively compensate for the effects of sun glitter

corruption and thus allow those systems freedom from the vulnerabilities they suffer as a result of intense solar reflection from the sea surface. There is still a need, therefore, to produce empirically based methods which perform this function. This can be accomplished through hardware modifications to IR systems such as the use of polarizing filters or dual band spectral discrimination techniques (which capitalize on the relatively weak response of the 8-14 μm waveband to sun glints). Additionally, newer software based systems can incorporate computer codes to vary their sensitivity to changes in sea radiance resulting from sun glitter. Such codes could be based on the physical parameters of sun glitter as described in this thesis to avoid the high false alarm rates resulting from direct solar reflections off the sea surface.

The data presented here indicates that although sun glitter may be inescapable to sea based infrared sensing systems, its effects can be better compensated for by knowing when and where sun glitter is least intense. Factors known to increase the magnitude of reflected sun glitter are low solar angles (early morning or late afternoon) and low wind speeds.

Shipboard operations, however, usually proceed without regard to these parameters. Therefore, IR systems should be able to predict and accommodate for sun glitter at all times in order to prevent them from being vulnerable to its effects. This requires some ability to measure locally certain

parameters and then use them to compute the extent of the sun glitter's effects on IR sensors in near real time. It would be necessary to measure the local weather conditions, solar azimuth and elevation, and seeker angle relative to the horizon in order to predict both the angular extent and magnitude of the interference presented to an IR sensor from sun glitter. With this information, the sensor could use adaptive thresholding techniques to reduce its false alarm rate while scanning across or sensing within a sun glitter corridor. Additionally, dual band systems could "handoff" to one another when, due to strong interferences in the short-wave sensor from sun glints, the long wave detector or some electronic combination of short and long wave signals would become dominant.

For an imaging system such as the AGA 780, any external compensation for atmospheric effects such as the one attempted in this thesis will meet with certain challenges: accurately defining what "source radiance" is and computing the true path radiance. These steps are necessary in order to be able to compare results with those obtained using other IR systems. When these concepts are applied to weapons systems, the challenges do not change. Those systems require accurate information as to the magnitude of any radiance within their FOV not emanating from a target. This allows them to capitalize on the contrasts between targets and their backgrounds. Having seen the difficulties inherent in

performing an external compensation for the effects of path radiance and atmospheric extinction, it is recommended that newer systems incorporate algorithms in their software to compute atmospheric transmissivity, path radiance (i.e., LOWTRAN) and sun glitter radiance (Saunders' sea radiance model with Tropf's SUN GLITTER code to compute corridor width). When a system receives an aggregate signal from a target embedded in a glinting background, it will then be equipped to account for the various radiance contributions to that scene and be better able to discern the target as a result.

APPENDIX A-SUN GLITTER CORRIDOR WIDTH PREDICTION CODE

```

C      SUN GLITTER PROGRAM
C      Calculates the angular width of a sun glitter corridor
C
C      The following program calculates the boundary of the sun
C      glitter corridor in terms of depression angle and bearing
C      relative to the sun, based on sea surface maximum slope,
C      observer latitude and longitude, and time inputs.
C
C      Inputs: maximum Wave Slope, Lat, Long
C              Day of Year, Time of Day (GMT)
C      ZMAX = Maximum Wave Slope
C      LAT1 = Observers Latitude, Degrees
C      LONG1 = Observers Longitude, Degrees
C      IDAY = Day of Year
C      Time = Time (GMT)
C
C      Outputs: Combination of Seeker Depression angles and
C               Azimuth Angle (Relative to Sun) where
C               Sun glitter is significant
C      LAT2 = Subsolar Latitude, Degrees
C      LONG2 = Subsolar Longitude, Degrees
C      MU = Sun Zenith Angle, Degrees
C      BEAR = Bearing to the Sun, Degrees
C      PHI = Seeker Depression Angle (Degrees)
C      NU = Seeker Azimuth and (Relative to sun)
C
C      REAL*4 LAT1, LONG1, LAT2, LONG2, TIME
C      REAL*4 MU, BEAR, ZMAX, DTR, PHIMIN, PHIMAX
C      REAL*4 PHI(91), NU(91), BETA(91)
C      REAL*4 NUEND
C      INTEGER*4 IDAY, IMIN, IMAX
C      DTR=ATAN(1.0)/45.
C      OPEN(UNIT=5, FILE='CON')
C      OPEN(UNIT=8, FILE='SUN.DAT')
20  WRITE(5,30)
30  FORMAT(' Input Maximum Slope (>10 to Stop):')
    READ(5,*) ZMAX
    IF(ZMAX.GT.10.0) GOTO 900
C  Calculate Maximum Tilt Angle (in radians)
    BETAMX=ATAN(ZMAX)
40  WRITE(5,50)
50  FORMAT(' INPUT OBSERVER LATITUDE (+ NORTH, -SOUTH):')
    READ(5,*) LAT1
    WRITE(5,60)
60  FORMAT(' INPUT OBSERVER LONGITUDE (+ WEST, - EAST):')
    READ(5,*) LONG1

```

```

WRITE (5,70)
70  FORMAT(' INPUT DAY OF YEAR (1-366):')
    READ(5,*) IDAY
    WRITE(5,80)
80  FORMAT(' INPUT TIME OF DAY, HH.DD (GMT):')
    READ(5,*) TIME
C   Determine Subsolar Point
    CALL SUBSOL(LAT2, LONG2, TIME, IDAY)
C   Determine Zenith Angle of Sun (MU) and
C   Bearing Angle to Sun (BEAR, measured Clockwise from North)
    TT=LONG1-LONG2
    IF(ABS(TT).GT.90.0) GOTO 800
    XX=SIN(DTR*LAT1)*SIN(DTR*LAT2)+
*   COS(DTR*LAT1)*COS(DTR*LAT2)*COS(DTR*TT)
    MU=ACOS(XX)/DTR
    IF(MU.LT.0.0) GOTO 800
    BEAR=0.0
    IF(MU.EQ.0.0) GOTO 87
    XX=COS(LAT2*DTR)*SIN(TT*DTR)/SIN(MU*DTR)
    BEAR=ASIN(XX)/DTR
    IF((LAT2-LAT1).LT.0.0) BEAR=180-BEAR
C   PHIMAX AND PHIMIN are maximum and minimum values of PHI
87  PHIMIN=90.0-MU-(2*BETAMX)/DTR
    IF(PHIMIN.LT.0.0) PHIMIN=0.0
    PHIMAX=90.0-MU+(2*BETAMX)/DTR
    IF(PHIMAX.GT.90.0) THEN
        PHIMAX=180.0-PHIMAX
    NUEND=180.0
    ELSE
        NUEND=0.0
    ENDIF
    IMIN=IFIX(PHIMIN+1.99999)
    IF(IMIN.LT.1) IMIN=1
    IMAX=IFIX(PHIMAX)+1
    IF(IMAX.GT.91) IMAX=91
    WRITE(5,210) LAT1, LONG1, IDAY, TIME, ZMAX,
*               LAT2, LONG2, MU, BEAR,
*               PHIMIN
    WRITE(8,210) LAT1, LONG1, IDAY, TIME, ZMAX,
*               LAT2, LONG2, MU, BEAR,
*               PHIMIN
210  FORMAT(' Observer Latitude = ',F8.3,' Degrees (+N, -S)',/,
*         ' Observer Longitude = ',F8.3,' Degrees (+W, -E)',/,
*         ' Day of Year = ',I3,'; Time (GMT) = ',F8.2,' Hours',/,
*         ' Maximum Sea Surface Slope = ',F5.2,/,
*         ' Subsolar Latitude = ',F8.3,' Degrees (+N, -S)',/,
*         ' Subsolar Longitude = ',F8.3,' Degrees (+W, -E)',/,
*         ' Sun Zenith Angle = ',F8.3,' Degrees',/,
*         ' Bearing to Sun = ',F8.3,' Degrees (CW from N)',/,
*         ' Depression Angle off Sun',/,F16.2,
*         ' 0.00')

```

```

DO 100 I=IMIN,IMAX
  PHI(I)=FLOAT(I-1)
  BETA(I)=BETAMX
C   COSOM is the cosine of the Angle OMEGA
  COSOM=(COS(DTR*MU)+SIN(DTR*PHI(I)))/(2.0*COS(BETA(I)))
  IF (COSOM.LE.1.0) GOTO 90
  COSOM=1.0
  COSBE=(COS(DTR*MU)+SIN(DTR*PHI(I)))/2.0
  BETA(I)=ACOS(COSBE)
90  CONTINUE
  OMEGA=ACOS(COSOM)
  COSNU=(SIN(PHI(I)*DTR)*COS(DTR*MU)-COS(2.0*OMEGA))/
  *      (COS(DTR*PHI(I))*SIN(DTR*MU))
  IF (ABS(COSNU).LE.1.0) THEN
    NU(I)=ACOS(COSNU)/DTR
  ELSE
    NU(I)=0.0
  ENDIF
C   Convert Radians to degrees
95  CONTINUE
C   ALPHA(I)=ALPHA(I)/DTR
99  WRITE(5,110) PHI(I),NU(I)
100 WRITE(8,110) PHI(I),NU(I)
110 FORMAT(2F16.2)
  WRITE(5,110) PHIMAX,NUEND
  WRITE(8,110) PHIMAX,NUEND
  GOTO 20
700 STOP
800 WRITE(5,810) LAT1, LONG1, IDAY, TIME, LAT2, LONG2, MU
  WRITE(8,810) LAT1, LONG1, IDAY, TIME, LAT2, LONG2, MU
810 FORMAT(' No Sun',/,
  *      ' Observer Latitude = ',F8.3,' Degrees (+N, -S)',/,
  *      ' Observer Longitude = ',F8.3,' Degrees (+W, -E)',/,
  *      ' Day of Year = ',I3,'; Time (GMT) = ',F8.2,' Hours',/,
  *      ' Subsolar Latitude = ',F8.3,' Degrees (+N, -S)',/,
  *      ' Subsolar Longitude = ',F8.3,' Degrees (+W, -E)',/,
  *      ' Sun Zenith Angle = ',F8.3,' Degrees',/)
  GOTO 20
900 STOP
END
SUBROUTINE SUBSOL(THETAS,PHIS,TIME,IDAY)
C
C   SUBROUTINE SUBSOL calculates the subsolar point angles
C   THETA and PHI based upon IDAY and TIME. Since each year
C   is 365.25 days, the exact value of the declination angle
C   changes from year to year. For precise values consult
C   'THE ASTRONOMICAL ALMANAC' published yearly by the U.S.
C   GOVT. Printing Office. The solar position is characterized
C   by 25 points below; this should predict the subsolar angles
C   within one degree. For increased accuracy, add more data.
C   SUBSOL is borrowed from LOWTRAN 7.

```


C
C The Equation of Time, EQT, is in minutes
C The Declination Angle, DEC, is in degrees

```

        DIMENSION NDAY(25),EQT(25),DEC(25)
        DATA IPR/5/
        DATA NDAY/1,9,21,32,44,60,91,121,141,152,160,172,182,
*       190,202,213,244,274,305,309,325,335,343,355,366/
        DATA DEC /-23.07,-22.22,-20.08,-17.32,-13.62,-7.88,4.23,
*       14.83,20.03,21.95,22.87,23.45,23.17,22.47,20.63,18.23,8.58,
*       -2.88,-14.18,-15.45,-19.75,-21.68,-22.75,-23.43,-23.07/
        DATA EQT /-3.23,-6.83,-11.17,-13.57,-14.33,-12.63,-4.2,
*       2.83,3.57,2.45,1.10,-1.42,-3.52,-4.93,-6.25,-6.28,-0.25,
*       10.02,16.35,16.38,14.3,11.27,8.02,2.32,-3.23/
        IF(IDAY.LT.1.OR.IDAY.GT.366) GOTO 900
        IF(TIME.LT.0.0.OR.TIME.GT.24.0) GO TO 910
        DO 10 I=1,25
        IF(NDAY(I).EQ.IDAY) GO TO 30
10      IF(NDAY(I).GT.IDAY) GO TO 20
20      I=I-1
        EQTIME=EQT(I)+
*       (EQT(I+1)-EQT(I))*(IDAY-NDAY(I))/(NDAY(I+1)-NDAY(I))
        DECANG=DEC(I)+
*       (DEC(I+1)-DEC(I))*(IDAY-NDAY(I))/(NDAY(I+1)-NDAY(I))
        GO TO 40
30      EQTIME=EQT(I)
        DECANG=DEC(I)
40      THETAS=DECANG
        EQTIME=EQTIME/60.0
        PHIS=15.0*(TIME+EQTIME)-180.0
        IF(PHIS.LT.-180.0) PHIS=PHIS+360.0
        RETURN
900     WRITE(IPR,901) IDAY
901     FORMAT( 'FROM SUBSOL - IDAY OUT OF RANGE, IDAY=',I6)
        STOP
910     WRITE(IPR,902) TIME
902     FORMAT(' FROM SUBSOL - TIME OUT OF RANGE, TIME=',E12.5)
        STOP
        END

```

APPENDIX B-MATLAB FUNCTIONS AGACOMP.M AND IRTEMP.M

```

function [q]=agacomp(s)
%
%   AGACOMP computes the source radiance of a pixel imaged by the
%   AGA 780 with emissivity and transmissivity set to 1 within
%   the imaging system. The program converts apparent temperature
%   to isothermal units and performs an external correction
%   of atmospheric interactions by using more valid forms of
%   epsilon and tau, obtained from the Schwartz and Hon
%   algorithm and LOWTRAN, respectively. The output is the source's
%   in band equivalent blackbody radiance ( $\text{Watts}\cdot\text{cm}^{-2}\cdot\text{sr}^{-1}$ ).
%
%   Written by Eric B. Moss, 3-15-92
%
%   Input parameters for horizontal row of pixels
disp('Currently set for short-wave: hit any key to acknowledge')
pause
t=input('Enter Transmissivity: ');
e=input('Enter Emissivity: ');
o=input('Enter Offset Correction: ');
%
%   A,B and C are calibration constants, C=1
%
A=183453;
B=2814;
format short e
%
%   Enter meteorological air temperature and convert to Kelvin
%
tamb=input('Enter Ambient Temperature, deg C: ');
tamb=tamb+273.15;
%
%   Convert air temperature to blackbody radiance (isothermal units)
%
iamb=A./(exp(B./tamb)-1)-o;
%
%   Implement algorithm to correct for atmospheric attenuation and
%   source emissivity
%
for n=1:length(s)
    s(n)=s(n)+273.15;
    i(n)=A./(exp(B./s(n))-1)-o;
    ic(n)=(i(n)-(1-t).*iamb)./(t.*e);
    tc(n)=(B./(log((A./(ic(n)+o))+1)))-273.15;
    g(n)=quad2par('irtemp',2,5.6,tc(n));
end
q=g;

```

```

function w=irtemp(x,t)
%
%   This function applies Planck's Law to a wavelength x and
%   a temperature t (K), yielding that body's spectral radiance
%    $N_\lambda$  in Watts·cm-2·μm-1·sr-1.
%
%   Written by Eric Moss, 2-15-92
%
w = (3.7415e4 ./ (x.^5)).*(1 ./ (exp(1.43879e4 ./ (x.*(t+273.15)))-1))/pi

```

LIST OF REFERENCES

1. Cox, C. S. and Munk, Walter, "Measurement of the Roughness of the Sea Surface from Photographs of the Sun's Glitter," *Journal of the Optical Society of America*, Vol. 44, No. 11, pp. 838-850, November, 1954.
2. Reynolds, William R., "Toward Quantifying Infrared Clutter," *SPIE Proceedings: Characterization, Propagation and Simulation of Infrared Scenes*, Vol. 1311, 1990, pp. 232-240.
3. Lindquist, George H., Ball, Bruce W. and Scheeres, Daniel, *Infrared Sea Background Modeling and Model Validation*, Nichols Research Corporation, Ann Arbor, Michigan, September, 1988.
4. Zachor, Alexander S., Holzer, James A. and Smith, Frederick G., *IR Signature Study*, Honeywell Electro-Optics Center, Lexington, Massachusetts, November, 1978.
5. Beard, J. J., *Reduction of Solar Glints from the Sea with a Linear Polarizer*, Environmental Research Institute of Michigan, Ann Arbor, Michigan, October, 1976.
6. Lloyd, J. M., *Thermal Imaging Systems*, Plenum Press, New York, 1975.
7. Hudson, Richard D., *Infrared Systems Engineering*, John Wiley and Sons, New York, 1969.
8. van Haersma Buma, C. E., *Infrared Sea Background Radiation*, National Defence Research Organization, The Hague, The Netherlands, Report No. PHL 1975-33, August, 1975.
9. Cooper, A. W., Notes for course PH3208, Electro-optic Principles and Devices, Naval Postgraduate School, 1990 (unpublished).
10. Wilf, I., and Manor, Y., "Simulation of Sea Surface Images in the Infrared," *Applied Optics*, Vol. 23, No. 18, 15 September, 1984.
11. Bell, Ely E.; Eisner, Leonard; Young, James and Oetjen, Robert A., "Spectral Radiance of Sky and Terrain at Wavelengths between 1 and 20 Microns. Part II: Sky

Measurements," *Journal of the Optical Society of America*, Vol. 50, No. 12, December, 1960.

12. Wolfe, William L. and Zissis, George J., *The Infrared Handbook*, Office of Naval Research, Department of the Navy, Washington, D.C., 1985.
13. Naval Ocean Systems Command Report TR 1294, *Sea and Sky Infrared Radiances Near the Horizon*, by Herbert G. Hughes, June, 1989.
14. Levesque, Martin P. and St-Germain, Daniel, "Generation of Synthetic IR Sea Images," *SPIE Proceedings: Characterization, Propagation and Simulation of Infrared Scenes*, Vol. 1311, 1990.
15. Jerlov, N. G., *Marine Optics*, Elsevier Scientific Publishing Company, New York, 1976.
16. Saunders, Peter M., "Radiance of Sea and Sky in the Infrared Window 800-1200 cm^{-1} ," *Journal of the Optical Society of America*, Vol. 58, No. 5, May 1968.
17. Eisner, Leonard; Bell, Ely L.; Young, James and Oetjen, Robert A., "Spectral Radiance of Sky and Terrain at Wavelengths between 1 and 20 microns. Part III: Terrain Measurements," *Journal of the Optical Society of America*, Vol. 52, No. 2, February, 1962.
18. Stengelmann, E.J. and Garvey, J.O., *Ocean Sunglitter Background in the Infrared*, Hughes Aircraft Company, Culver City, California.
19. Basener, R.F. and McCoyd, G.C., *Polarization of Light Emitted by the Sea*, Grumman Research Department, Geo-Astrophysics Section, Memorandum RM-360, April 1967.
20. Tropf, W.J., *Sea/Sky Horizon Infrared Contrast*, The Johns Hopkins University Applied Physics Laboratory, Memorandum F1A79U-033, 20 June 1979.
21. Naval Research Laboratory Memorandum Report No. 5816, "Emissivity as a Function of Surface Roughness: A Computer Model," by I. B. Schwartz and D. Hon, 1986.
22. Lawler, Gregory M., LT USN, *Validation of the Schwartz and Hon Algorithm at Low Grazing Angles*, Master's Thesis, Naval Postgraduate School, Monterey, California, September, 1990.

23. Naval Research Laboratory Report 6736, "Infrared Characteristics of Ocean Water (1.5-15 Microns)," by Daniel Friedman, July 11, 1968.
24. Tropf, W.J., *Sun Glitter off the Horizon Sea*, The Johns Hopkins University Applied Physics Laboratory Memorandum F1A79U-047, 20 August 1979.
25. Cox, C.S. and Munk, Walter, "Statistics of the Sea Surface Derived from Sun Glitter," *Journal of Marine Research*, Vol. 13, No. 2, 1954, pp. 198-227.
26. Sidran, Miriam, "Broadband Reflectance and Emissivity of Specular and Rough Water Surfaces," *Applied Optics*, Vol. 20, No.18, 15 September, 1981, pp.3176-3183.
27. Wu, Jin, "Sea Surface Slope and Equilibrium Wind-Wave Spectra," *The Physics of Fluids*, Vol. 15, No. 5, May, 1972, pp. 741-747.
28. Jerlov, N. G. and Nielsen, Steemann E., *Optical Aspects of Oceanography*, London, Academic Press, 1974.
29. Fraedrich, D. S., "Spatial and Temporal Infrared Radiance Distributions of Solar Sea Glints," *SPIE Proceedings: Ocean Optics IX*, Vol. 925, 1988, pp. 392-397.
30. Schwering, Piet, "Infrared Clutter Measurements of Marine Backgrounds," *SPIE Proceedings: Characterization, Propagation and Simulation of Sources and Backgrounds*, Vol. 1486, 1991, pp. 25-36.
31. Massachusetts Institute of Technology Lincoln Laboratory IRIS Paper 1991, *Infrared Background Measurements and Water/Glint Analysis*, by R.M. O'Donnell, G.M. Daniels and T. Zomers (Group 46), 30 January, 1991.
32. Gambling, D.J., "Sun Glitter on the Surface of the Ocean in the Infrared Spectral Region," *Infrared Physics*, Vol. 15, 1975, pp. 149-155.
33. Tropf, W.J., *Definition of the Sea Surface Sun Glitter Corridor*, The Johns Hopkins University Applied Physics Laboratory Memorandum F1F (0)90-U-138, 11 May, 1990.
34. AGA Thermovision 780 Operating Manual, AGA Infrared Systems AB, Publication No 556 556 492/Ed II, 1980.
35. Naval Ocean Systems Command Technical Document 1193, *Effects of Atmospheric Model Layering on LOWTRAN 6 Calculations of 8- to 12- μ m Near Horizon Radiances*, by

F.G. Wollenweber, Naval Ocean Systems Command, San Diego, California, January, 1988.

36. ONTAR Corporation, *PC-TRAN Version 2 Software Manual*, ONTAR Corporation, Brookline, Massachusetts, 1987.
37. Ostrowski, P.P., Perez-Esandi, J. and Snedegar, R.W., "Naval Ocean Infrared Background Analysis," *SPIE Proceedings: Characterization, Propagation and Simulation of Infrared Scenes*, Vol. 1311, pp. 265-276, 1990.
38. Cooper, A.W., Crittenden, E.C., Milne, E.A., Walker, P.L., Gregoris, Dennis and Moss, E., "Mid and Far Infrared Measurements of Sun Glint From the Sea Surface", *SPIE Proceedings: Characterization, Propagation and Simulation of Sources and Backgrounds*, Vol. 1749, July 1992.

INITIAL DISTRIBUTION LIST

- | | | |
|----|---|---|
| 1. | Defense Technical Information Center
Cameron Station
Alexandria, VA 22304-6145 | 2 |
| 2. | Library, Code 0142
Naval Postgraduate School
Monterey, CA 93943-5000 | 2 |
| 3. | Professor A. W. Cooper, Code PH Cr
Department of Physics
Naval Postgraduate School
Monterey, CA 93943-5000 | 2 |
| 4. | Professor R. Pieper
Department of Electrical and Computer Engineering
Naval Postgraduate School
Monterey, CA 93943-5000 | 1 |
| 5. | The Johns Hopkins University
Applied Physics Laboratory
Attn: Dr. R. Steinberg, F1F Group
Johns Hopkins Road
Laurel, MD 20707 | 1 |
| 6. | Commander
Naval Surface Weapons Center (NWSC)
Attn: John Shipp and Ken Hepfer, Code F44
Dahlgren, VA 22448-5000 | 1 |
| 7. | Commander
Naval Research Laboratory (NRL)
Attn: Dr. Rich Priest, EO/IR Systems
4555 Overlook Ave.
Washington, DC 20375-5000 | 1 |
| 8. | Professor J.B. Knorr, Code EW
Electronic Warfare Academic Group
Naval Postgraduate School
Monterey, CA 93943-5000 | 1 |
| 9. | Commander Naval Research Laboratory, Monterey
Attn: Mr. John Cook
Naval Warfare Support Department
Monterey, CA 93943-5000 | 1 |

10. Commander, Naval Sea Systems Command 1
Ship Self Defense Group
Attn: Mr. J. Misanen
Washington, D.C. 20363-5100
11. LT Eric B. Moss 1
Surface Warfare Officer's School
Department Head Class #125
446 Cushing Road
Newport, RI 02841-1209

DUDLEY KNOX LIBRARY
NAVAL POSTGRADUATE SCHOOL
MONTEREY CA 93943-5101



GAYLORD S





3 2768 00018987 2